Force-Modulated Growth of Carbon Nanotube Forests

by

Nicholas T. Dee

B.S. Materials Science & Engineering, and Engineering Mechanics
Johns Hopkins University, 2013

Submitted to the Department of Mechanical Engineering
in Partial Fulfillment of the Requirements for the Degree of

MASTER OF SCIENCE IN MECHANICAL ENGINEERING

at the

MASSACHUSETTS INSTITUTE OF TECHNOLOGY

September 2015

Signature of Author: Signature redacted
Department of Mechanical Engineering
August 24, 2015

Certified by: Signature redacted
A. John Hart
Associate Professor of Mechanical Engineering
Thesis Supervisor

Accepted by: Signature redacted
David E. Hardt
Chairman, Committee on Graduate Students

this page intentionally left blank

Force-Modulated Growth of Carbon Nanotube Forests

by

Nicholas T. Dee

Submitted to the Department of Mechanical Engineering
on August 24, 2015 in Partial Fulfillment of the
Requirements for the Degree of Master of Science in
Mechanical Engineering

ABSTRACT

Carbon nanotubes (CNTs) can have exceptional mechanical, thermal, and electrical behavior, but successful use of CNTs in macroscale materials requires scalable processes to organize CNTs while preserving their intrinsic properties. Although the chemical influences on CNT growth have been subject to significant research, the effect of mechanical forces, which have been shown to influence the kinetics of many chemical reactions, remains unclear. When CNTs grow into vertically aligned "forest" structures by chemical vapor deposition (CVD), entanglement and attractive forces among the CNTs cause the CNTs to become mechanically coupled. Further, because there is a distribution of sizes, orientations, and growth rates amongst individual CNTs within a forest, it has been suggested that coupled CNTs develop forces that are transmitted to the growth interface at the catalyst.

The goal of this thesis is to investigate the effects of applied mechanical forces and intrinsic forces that result from mechanical coupling on CNT growth. Using a custom-built chemical vapor deposition system including a micromanipulator that can apply compressive loads to a CNT forest and measure its height in real-time, the effects of extrinsic mechanical forces on the growth kinetics and forest morphology were studied. It was found that forces as small as 0.1 nN per CNT decrease the collective growth rate of the CNT forest along with its terminal height. Furthermore, time-varying forces can be used to induce a morphological change in the forest structure and modulate the apparent growth rate without causing termination. Next, a finite element model was developed to simulate the forces exerted between a pair of CNTs growing at different rates and coupled by van der Waals forces. The simulation predicts that mechanical coupling between CNTs enables forces exceeding 10 nN to be transmitted to the catalyst, which are potentially several orders of magnitude larger than the externally applied forces that were found experimentally to influence forest growth. Together, these findings suggest that the quality and growth rate of CNT forests may be limited by CNT-CNT mechanical coupling and force transmission to the catalyst, and motivate future work using controlled forces to manipulate the quality and morphology of CNTs for various applications.

Thesis Supervisor: A. John Hart

Title: Associate Professor of Mechanical Engineering

this page intentionally left blank

Acknowledgements

I would especially like to thank Professor A. John Hart for his guidance, brilliant insight, and patience during the past two years. John's excitement about exploring the frontiers of science and engineering is contagious and inspirational, and I look forward to continue working with him over the coming years.

I would also like to thank Dr. Mostafa Bedewy for being a great mentor and who laid the foundation for this thesis.

I am grateful to Abhinav Rao for his invaluable insight and assistance with simulations.

I truly appreciate Hangbo Zhao's tireless work in preparing samples for me.

I would also like to thank Justin Beroz, Kendall Teichert, Tom Serbowicz, and others who designed and built the "Mechanochamber".

I would like to thank Sebastian Pattinson for his guidance throughout my graduate career, especially during the thesis writing process.

I am grateful for the countless help I've received from other members of the Mechanosynthesis group, both current and former.

Finally, I would like to thank the Department of Mechanical Engineering at MIT and the National Science Foundation for providing the support that has enabled me to conduct this research.

this page intentionally left blank

Chapter 1 Introduction

1.1 Motivation and Background

Carbon nanotubes (CNTs) are a cylindrical allotrope of carbon, with rolled sheets of a hexagonal lattice of sp^2 bonded carbon atoms (graphene) forming the walls of the nanotube. A CNT comprised of a single sheet is called a single-walled nanotube (SWNT), and a CNT made of multiple concentric sheets is a multiwalled nanotube (MWNT). The chirality of a CNT depends on the orientation of the hexagonal lattice of the CNT walls with respect to the CNT axis, as defined by the (n,m) combination of basis vectors a_1 and a_2 (**Figure 1.1**) [1]. An "armchair" CNT has m = n, a "zigzag" CNT has n = 0 or m = 0, and the other combinations form "chiral" CNTs (**Figure 1.2**) [2]. The chirality determines the CNT's bandgap and consequently its electronic properties; all armchair SWNTs and those with $n - m = 3k$ (for nonzero integer k) are metallic [1], [2], SWNTs of other chirality are semiconducting [2], and for practical purposes MWNTs are metallic [3] because their bandgap is inversely proportional to diameter regardless of chirality. The aspect ratio of CNTs is quite large; their diameters can vary from 0.2-2 nm for SWNTs and 5-100 nm (though they are typically limited to 20 nm) for MWNTs, and lengths from 100 nm to a few centimeters [3].

Since the 1991 report in *Nature* by S. Iijima [4], there has been much excitement over the potential for CNTs to be used as an enabling material for newly engineered devices because of their exceptional thermal, electrical, and mechanical properties [2], [3]. CNTs are reported to have a room-temperature thermal conductivity of 3500 $Wm^{-1}K^{-1}$ [5] (compared to 398 $Wm^{-1}K^{-1}$ for copper [6]), current carrying capacity of 10^9 A/cm^2 [7] ($\sim 10^6$ for common electrical conductors like Cu and Au [8]), and Young's modulus of 1 TPa and tensile strength of 100 GPa [9] (207 GPa and 2.55 GPa for 1080 steel [10]). Axially aligned arrays of CNTs (or CNT "forests") are very promising assemblies for taking advantage of these unique properties at a larger scale, for example in gas and water filtration membranes [11], [12], flexible high-conductivity electrical interconnects [13], reinforcement to join interfaces of laminated composites [14], reversible dry adhesives [15], and interface materials for thermal management of electronic devices [16]. However, translating the outstanding nanoscale properties of individual CNTs to macroscopic objects remains challenging, to a large extent because it has proven difficult to assemble CNTs in a way that maximizes their macroscopic properties [3].

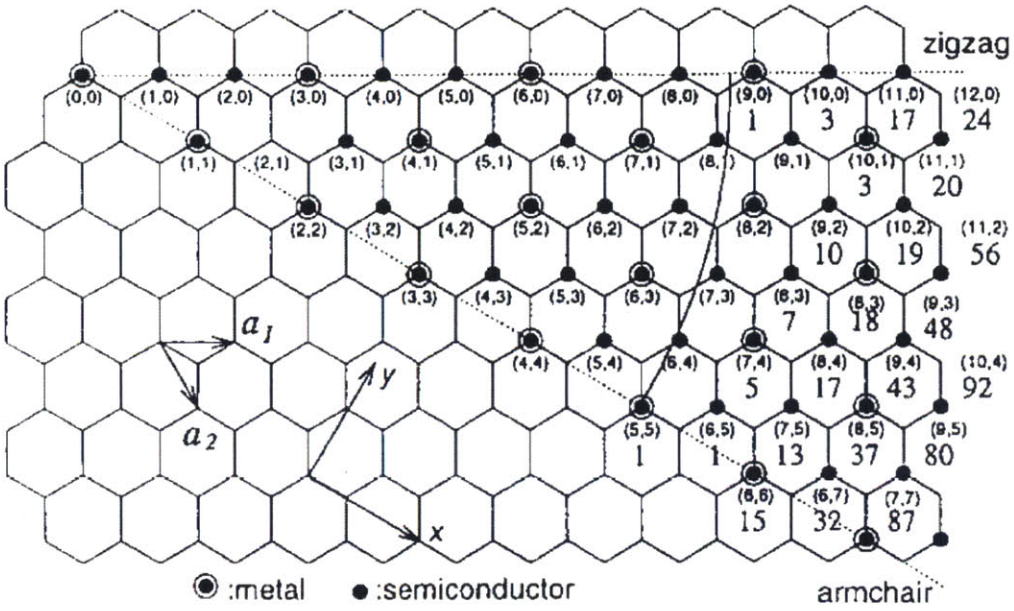

Figure 1.1 Graphene lattice structure showing the (n,m) combinations of basis vectors a_1 and a_2 that specify CNT chirality [1].

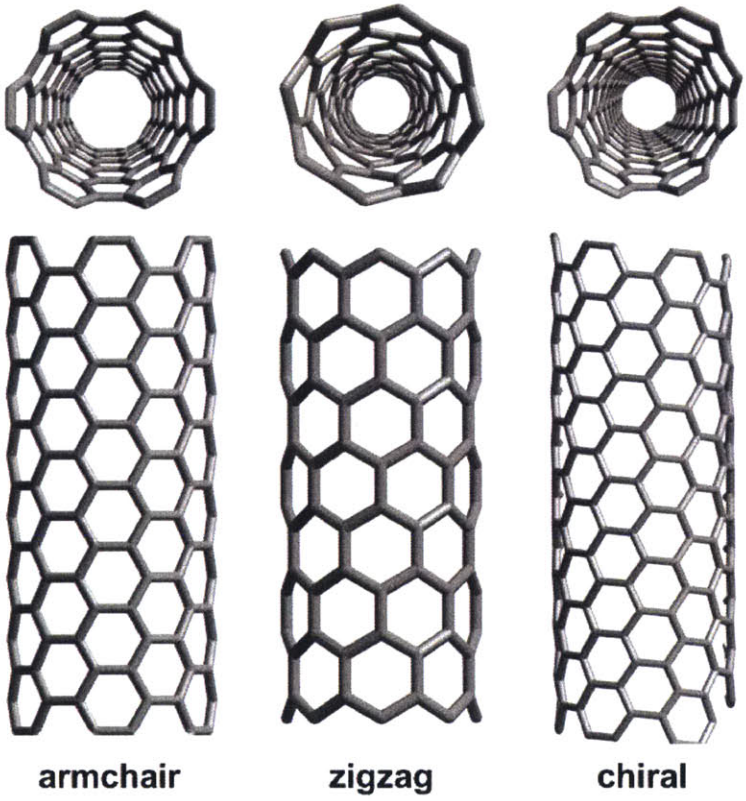

Figure 1.2 Structure of CNTs of different chirality [17].

CNT forests are typically formed on flat substrates, and require self-organization of the CNTs perpendicular to the substrate by crowding during the initial stage of the growth process. This can be accomplished using chemical vapor deposition (CVD) [18], in which gases are passed through a reaction furnace to react and synthesize materials on top of a catalytic substrate. The most important parameters for achieving high density and thus an aligned forest are the carbon source material, the catalyst material, the support material, and the growth temperature. The carbon source must be reactive enough to achieve to dissociation into active carbon species without resulting in soot formation; some common hydrocarbon precursors include methane, ethylene, acetylene, benzene, carbon monoxide, cyclohexane, and xylene [19], [20] . The requirements for a CNT catalyst are that it can break down the carbon source into active carbon species, allow for diffusion of those active carbon species, and serve as a template for the proper cylindrical morphology of CNTs [19], [20]. There are many options for catalysts, but typical ones include the transition metals Fe, Co, and Ni [20]. The catalyst-substrate interaction is also important, as a strong interaction could reduce catalytic behavior, though some interaction is thought to be necessary to prevent catalyst sintering [20]. In many cases, a thin "barrier" layer of an oxide such as alumina or silicon is deposited for this purpose [20]. Finally, the growth temperature must be high enough to allow for the decomposition of the carbon source without being so high that the formation of polymeric carbon chains predominates that of graphitic carbon [19]. MWNTs tend to grow at temperatures between 600 °C and 900 °C, while SWNTs are often grown at higher temperatures, between 900 °C and 1200 °C [20].

To initiate the CNT growth, the typically inactive metal oxide catalyst is reduced with hydrogen gas, allowing for the hydrocarbons to interact with the pure metal catalyst. The atomic mechanism of CNT growth is not fully understood, but can be classified depending on the strength of the catalyst-substrate interaction [20]. These types of growth are shown schematically in **Figure 1.3**. With a strong interaction ("base-growth"), the catalyst dewets into nanoparticles that adhere to the substrate. Carbon species break down on the catalyst and diffuse into it, precipitating out and joining together to form a hemispherical cap. Subsequent growth in the axial direction pushes the cap off the catalyst, forming the CNT walls and elongating the tube. The alternative mechanism to CNT growth is "tip-growth", in which the catalyst particle is weakly adhered to the substrate. Growth of the CNT walls results in the CNT growing between the catalyst and the substrate, lifting the catalyst off the substrate [20].

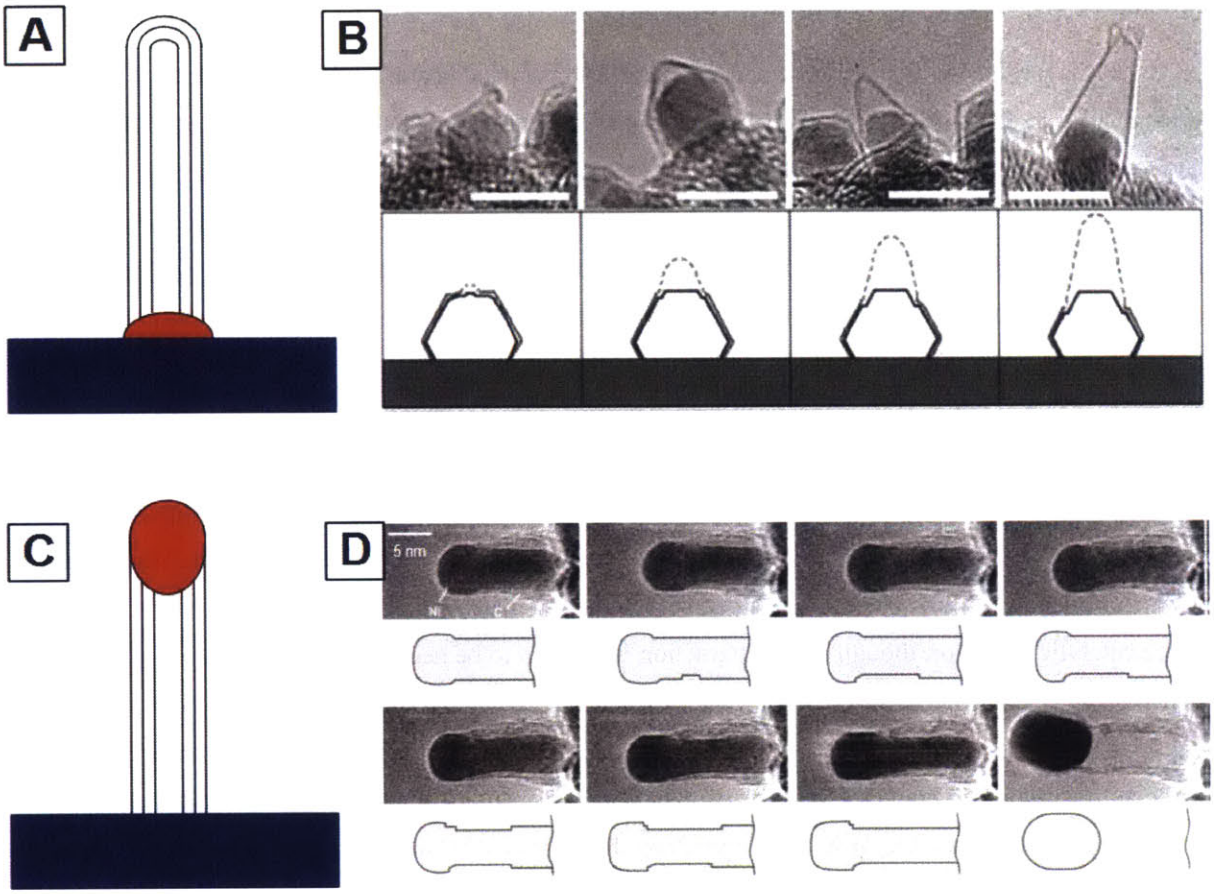

Figure 1.3 (A) Schematic of base-growth. (B) Still frames from an *in situ* transmission electron microscope (TEM) video and accompanying schematics of base-growth [21]. (C) Schematic of tip-growth. (D) Still frames from an *in situ* TEM video and accompanying schematics of tip-growth [22].

Both the nanoscale and macroscale properties of CNTs depend on their structure and assembly. Defects can develop during the CNT growth process. For instance, a carbon atom vacancy in the CNT wall can result in a pentagon forming in the wall and breaking the hexagonal symmetry, leading to anisotropic properties, curved morphology, and degradation of properties of individual CNTs [23]. Additionally, the aforementioned applications require precise control over the density, alignment, and uniformity of CNTs that constitute a forest [24]–[26]. However, a typical forest contains CNTs of a wide range of sizes that exhibit a tortuous morphology (**Figure 1.4**) [27]. Both the nanoscale and macroscale defects that undermine CNT properties arise during the growth process. While the chemical and physical influences on CNT growth have been extensively studied, the effect of mechanical forces, though potentially critical, remains unclear [28]. To achieve reliable production of CNTs for applications, it is thus pertinent to understand how forces affect the growth of CNT forests, and to utilize this understanding to improve the fabrication process and realize the applications of vertically aligned CNT arrays.

Therefore, the goal of this thesis was to investigate the effects of applied mechanical forces on the growth kinetics and quality of CNT forests, and to predict the strength of mechanical coupling between a pair of growing CNTs and the resulting intrinsic forces that develop at the catalyst. As discussed in detail in the following chapters, these tasks were accomplished with experiments using a custom-built CVD reactor with an internal micromanipulator for applying forces *in situ*, and with a finite element model that captures the dynamics of mechanical coupling.

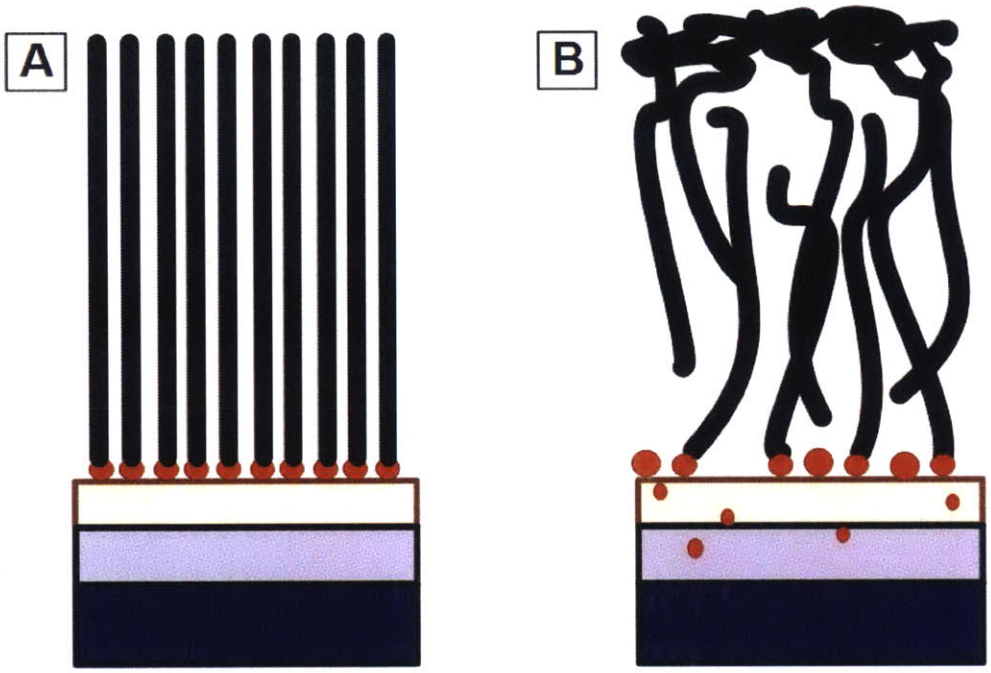

Figure 1.4 (A) Ideal CNT forest of uniformly spaced, vertically aligned CNTs of equal diameters. (B) Representative of an actual forest, with polydisperse catalyst particles and CNT sizes, contributing to a tortuous morphology [courtesy of M. Bedewy].

1.2 Outline

The remainder of the thesis is organized as follows:

Chapter 2 Discusses mechanochemistry – the study of the confluence of mechanical and chemical forces – and how it relates to CNT forest growth.

Chapter 3 Presents a custom-built chemical vapor deposition and microcompression system, which was built by colleagues in the Mechanosynthesis group and refined by the author, and measurement of its performance to apply *in situ* compressive forces to growing CNT forests.

Chapter 4 Presents the results of experiments where compressive forces were applied to influence the growth kinetics and morphology of CNT forests.

Chapter 5 Presents the use of a finite element model to simulate the mechanical coupling of CNTs and the consequent distribution of forces across the CNTs using simulations.

Chapter 6 Summarizes the key findings of the thesis and identifies the subsequent efforts from this work.

Chapter 2 The Influence of Mechanical Forces on Chemical Reactions

2.1 Introduction to Mechanochemistry

It has been known since ancient times that mechanical forces can help initiate and stimulate chemical reactions [29], [30]. The first known documented case of this phenomenon was described by Theophrastus of Eresus near the end of the fourth century B.C., concerning extracting "quicksilver" (mercury) by grinding cinnabar and vinegar together with a mortar and pestle [31]. However, the coupling between mechanical and chemical energetics was not thoroughly investigated until the nineteenth century, during which time the chemist Wilhelm Oswtald introduced the term "mechanochemistry" [32], [33]. Since then, mechanochemistry has come to refer primarily to the use or influence of mechanical energy on transformations, and has become a well-established field within chemistry and materials science [29], [32], [33].

Mechanochemistry can be regarded as an analogue to electrochemistry and other methods of physical activation of chemical reactions. The non-equilibrium thermodynamics of concurrently occurring processes can be superimposed according to the phenomenological relationship:

$$J_i = \sum_{k=1}^{n} L_{ik} X_k \tag{2.1}$$

This equation states that a generalized flux J_i is influenced by all manner of forces $X_k \ldots X_n$ acting in a system, proportional to the phenomenological coefficients L_{ik}. For example, a temperature gradient (i) and/or a concentration gradient (k) can cause a heat flux J_i related by the thermal conductivity L_{ii} and the Dufour coefficient L_{ik} [34]. Compared to other methods of physically initiating chemical reactions, the mechanical energy required to do so can be lower than the covalent bond energy; the mechanical energy is concentrated on the atomistic scale, deforming the bond and lowering its potential [29], [35], [36]. This reduction in activation energy ΔE_A can be described as being a function of the applied force F and the difference in the geometry of the transition state Δd via a simplified relationship [37]:

$$\Delta E_A = F \cdot \Delta d \tag{2.2}$$

A schematic representation of the implications of this equation is illustrated in **Figure 2.1**, showing a downward shift in the activation energy for a reaction as force is applied.

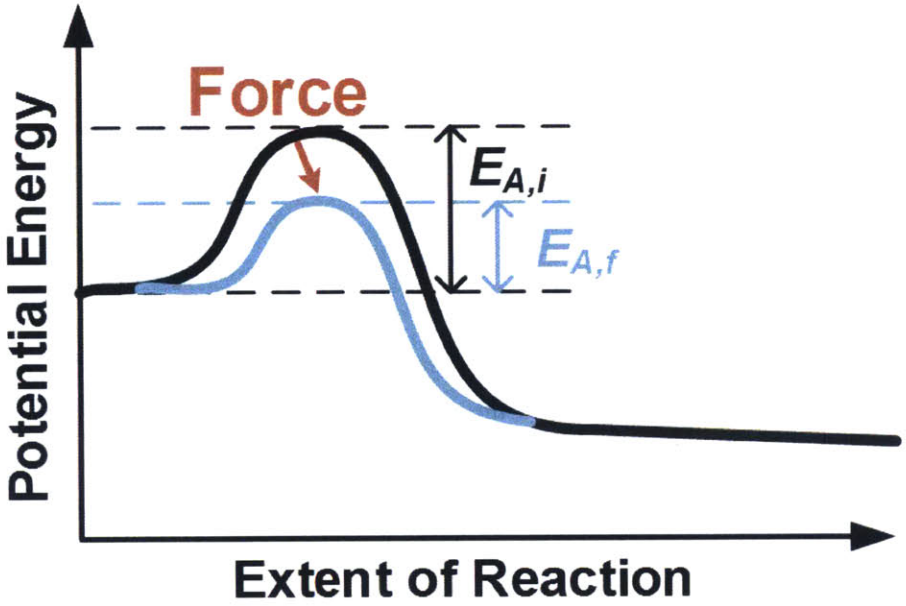

Figure 2.1 Illustration of a shift in the activation energy for a reaction when force is applied

The kinetics of a chemical reaction under mechanical stress will consequently be affected by the change in activation energy. For a constant stress, this can be described by a modified Arrhenius equation for rate constant k:

$$k = k_o exp\{-(E_A - \alpha\sigma)/RT\} \tag{2.3}$$

where the activation energy for the chemical reaction E_A is shifted linearly by an amount proportional to the stress σ [36]. Therefore, the presence of mechanical stress can be expected to have a large effect on atomistic processes including atomic diffusion, bond transformation, catalysis, and crystal growth.

The principle of mechanochemistry has been studied and utilized extensively in the field of polymer chemistry. Polymerization can be mechanically activated using turbulent flow through an extruder and vibratory milling, among other techniques [38]. The atomic force microscope (AFM) has enabled single-molecule force spectroscopy to elucidate mechanically activated structural changes in polymers, in a setup as described in **Figure 2.2**. For instance, Rief *et al.* found that vertical stretching an individual dextran molecule initiated a change in the conformality of the polymer chain [39]. Another study utilizing the same technique applied to a compound of pyridine ligands connected by poly(ethylene glycol) linkers revealed that a great enough force can cause bond rupture [40]. Similarly, applied tension to a single molecule of polybutadiene functionalized by *gem*-dibromocyclopropane (gDBC) caused the irreversible isomerization of the gDBC. These understandings have allowed for the development and implementation of mechanically

activated functional groups (mechanophores) in polymers, which can upon application of force undergo controlled transformations such as ring opening, isomerization, or bond scission [37], [41]. These developments have shown that mechanical force can be used as a means of selectively inducing desired chemical changes in molecules.

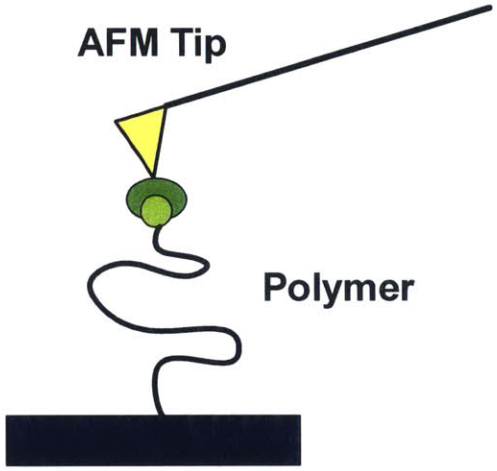

Figure 2.2 Setup for single-molecule force spectroscopy of a polymer using an AFM tip

Mechanochemistry is also relevant to catalysis. Mechanical force, in the form of ultrasonication for instance, provides a controlled means of activating latent catalysts of polymers containing catalytic mechanophores [42], [43]. Additionally, researchers are beginning to thoroughly investigate the use of stress to control and potentially enhance catalytic activity. These studies have mostly concerned electrocatalytic hydrogen evolution reactions (HER) and oxygen reduction reactions (ORR) because they are relatively well-understood and technologically important. Experimental efforts have included straining thin films during electrochemical deposition [44], [45] and constructing lattice-strained core-shell nanostructures [46]. The corresponding effects on electronic structure and catalytic activity have been simulated using density functional theory [45], [47]. Utilization of mechanical stress has been found to be a promising method for control of activation and enhancement of catalysts.

Furthermore, mechanical forces have been found to have an enabling effect on material synthesis and crystal growth. Aziz *et al* measured and enhanced the solid phase epitaxial growth rate of B_2O_3 [48] and Ge [49] by application of hydrostatic pressure. Similarly, application of nonhydrostatic pressure with three-point bending of a Si wafer found that epitaxial growth of crystalline Si was affected, with greater growth rate on the tensile side than the compressive side [50]. Heteroepitaxial growth of Ag on Pt was also found to be influenced by strain, as the compressive strain from lattice mismatch decreases diffusion barriers, changing the kinetics of adatom surface diffusion and grain nucleation [51]. Mechanical force can

also be used as an engineering parameter to enable the synthesis of novel nanoscale materials, such as using the ball milling technique to create metallic compound nanoparticles of a desired composition [52]–[55]. Additionally, mechanical agitation has been found to improve the diffusion and chemical reaction rates for the synthesis of TiO_2 nanotubes, resulting in elongation of the nanotubes that would have an advantageous effect for applications in rechargeable lithium ion batteries [56]. Therefore, mechanical forces can be used to direct the atomic pathways during diffusion and growth processes.

2.2 Effects of Mechanical Forces on CNT Forest Growth

Mechanical coupling of non-uniform CNTs causes the collective forest to deviate from the ideal vertically aligned monodisperse arrays (**Figure 2.3**). As revealed by *in situ* x-ray scattering of growing forests, a forest growth undergoes a series of characteristic stages [27]:

1. Initial growth of the CNTs occurs in many different directions. The CNTs come into contact with each other, becoming mechanically coupled and self-organizing into a tangled "crust". After enough CNTs have joined the crust to make it self-supporting, it lifts off the substrate surface and further growth is more vertically aligned.
2. There is a density increase as more CNTs nucleate from the catalyst particles and grow into the forest.
3. A period of steady growth ensues, with no significant change in density.
4. The density slowly begins to decay as individual CNT growth deactivates, likely due to catalyst poisoning or migration.
5. Self-termination of the forest occurs as the decay in density reaches a point at which the forest is no longer self-supporting.

The result of these stages of growth having differences in density and alignment is that there is microscopic non-uniformity throughout the height of the forest in addition to nanoscale non-uniformity between CNTs.

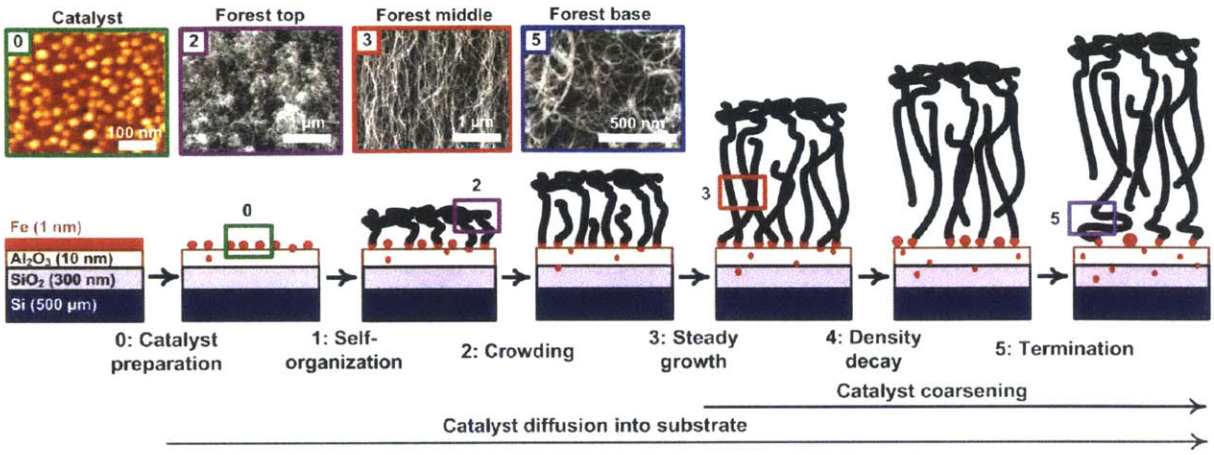

Figure 2.3 Stages of CNT forest growth, along with an AFM image of the catalyst and scanning electron microscope images of different heights of the forest [27].

One can consider the multi-scale mechanochemical phenomena governing the presence of intrinsic and extrinsic stresses during CNT forest growth, as shown schematically in **Figure 2.4**. At the macroscale, external forces can induce deformation and buckling of the CNT forest structure, as well as affect the collective growth rate of the forest. Hart and Slocum showed that placing weights on the catalyst substrate before growing a multi-walled CNT forest resulted in the forest growing to shorter heights as it lifted the weights during growth [57]. Additionally, with increasing weight, the CNTs became more tortuous until coordinated buckling of the CNTs within the forest was observed. The force needed to create CNTs with apparently buckled shapes during growth was found to be 0.40 nN per CNT, much smaller than the 10 nN required to buckle an already-grown CNT of the same effective length. Furthermore, transmission electron microscope (TEM) images revealed that CNTs grown under load contained significant structural defects and "built-in" waviness [57]. These results suggest that externally applied loads can affect the chemical processes involved in CNT forest growth.

Mechanical coupling between CNTs due to van der Waals forces results in intrinsic stress development and increased tortuosity. It has been demonstrated that CNTs within a forest will have a distribution of diameters [58]–[60], and the growth rates of CNTs are diameter dependent [59], [60]. Furthermore, Puretzky *et al.* developed a mathematical model of the diffusion and precipitation processes involved in CNT growth, which predicts that the diameter and growth rate are positively correlated [61]. Consequently, as two CNTs of different diameters come into contact, being held together by van der Waals forces, the larger CNT will be pushed in compression and the smaller CNT pulled in tension [28]. This is illustrated in a TEM image of two growing CNTs taken by Mostafa Bedewy, showing the buckling walls of the larger CNT (**Figure 2.5**). The implications are that throughout a CNT forest, CNTs of different

growth rates are forming contacts with each other, imparting stresses on one another, and exerting forces on the catalyst.

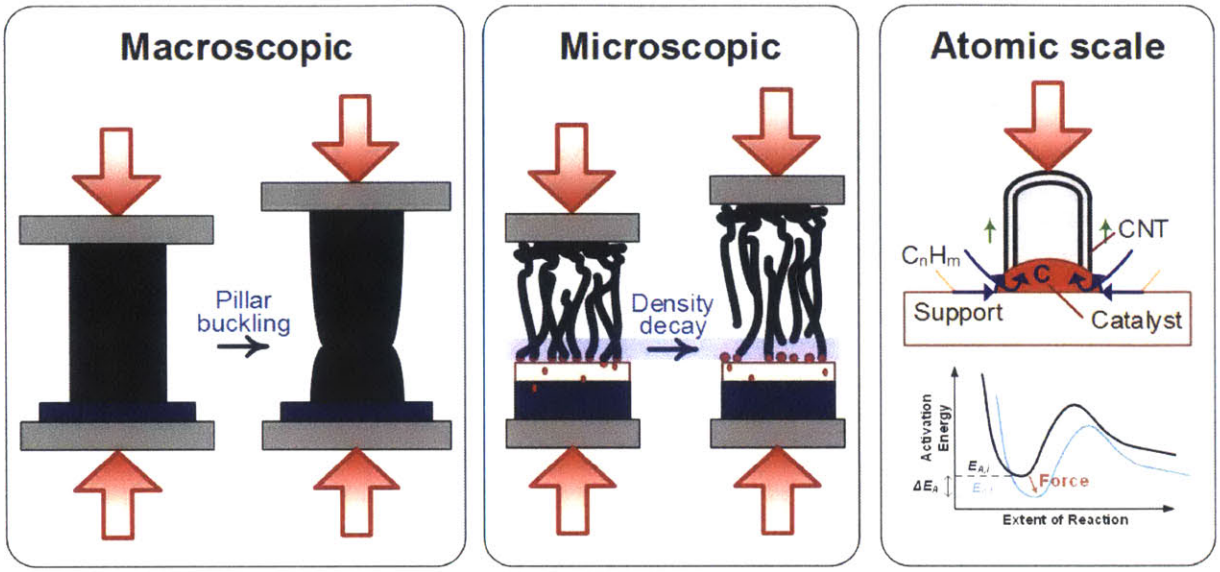

Figure 2.4 The multi-scale mechanochemical effects of CNT growth with external forces [courtesy of M. Bedewy]

Figure 2.5 TEM image of two coupled CNTs, with the CNT on the right in compression as evidenced by buckles in its walls [courtesy of M. Bedewy]

The intrinsic forces generated as a result of mechanical coupling are transmitted to the CNT-catalyst interface, where carbon precipitates from the catalyst and the walls of the CNT are formed. Bedewy and Hart calculated that a CNT could potentially impart a load of tens of nN on a catalyst particle during growth as a result of mechanical coupling [28]. As has been discussed in the preceding section on mechanochemistry, these forces at the growth front could potentially alter the energetic landscape of the CNT growth. For instance, results from the studies on stress-induced catalysis for ORR and HER indicate that stresses transmitted to the catalyst particles will alter the catalyst particle's activity. Additionally, stress could mediate the diffusion of the carbon species through the catalyst and to the CNT growth front. Finally, the mechanical force could cause a shift in the activation energy of the reactions involved in CNT synthesis.

Mechanical forces have been found to affect CNT forest growth from the macro- to nanoscale, with implications on the atomic processes governing CNT growth. However, there have been no studies to the author's knowledge of applying controlled forces during growth, and relating these applied forces to the dynamic forces generated by the growth behavior of the CNT population. The subsequent chapters of this thesis detail studies to further investigate the multi-scale effects of applied force on forest morphology and growth rate, and the microscopic mechanism of mechanical coupling that leads to stress development at the catalyst.

this page intentionally left blank

Chapter 3 Mechanochamber: A System for Mechanochemical Vapor Deposition of Carbon Nanotube Forests

3.1 Introduction

Mechanical forces have been found to have detrimental effects on CNT forest growth [28], [57], warranting the need for experimental investigation into the mesoscale mechanochemical phenomena that occur during CNT growth. One possibility might be to use a conventional microcompression or nanoindentation device to apply external forces during CNT synthesis. There have been many studies using nanoindentation techniques to reveal the mechanical properties of already-grown CNT forests [62]–[65], including using an indenter capable of operating in a vacuum environment in a scanning electron microscope (SEM) for *in situ* studies [66]. However, none of these techniques used equipment that can be operational in the harsh chemical vapor deposition (CVD) conditions that is required to study the mechanochemical effects on synthesis of CNTs. The main issue with high temperature testing is thermal drift, but some specialized devices have been made to partially accommodate this, including one device that can perform microcompression and nanoindentation studies at up to 665 °C in vacuum [67], and another that can perform nanoindentation studies at up to 500 °C in inert atmospheres at variable pressures [68] . Despite these advances, none of these devices or techniques would be able to withstand the harsh gas environment and high temperatures required to apply *in situ* forces during CNT synthesis.

This chapter describes the "Mechanochamber", which is a custom-built microcompression system with high temperature and variable atmosphere and pressure capabilities. With a coupled actuation and measurement system, a linear probe can move with micron-scale motion resolution and with force resolution of ~ 0.1 g. In addition, the system has a heater stage that can reach 1000 °C, inlets for gas flows, and a vacuum system so that it can operate under a variety of environmental conditions. The system can therefore be used as a cold-wall chemical vapor deposition (CVD) reactor and can apply and measure compressive forces to the substrate *in situ.* These unique capabilities allow for the investigation of the effects of external mechanical forces on the synthesis of CNT forests. The Mechanochamber was designed and built by J. Beroz, K. Teichert, M. Bedewy, and T. Serbowicz, as well as other contributors.

3.2 Design of the System and its Components

Figure 3.1 shows a picture of the Mechanochamber and a schematic of its main components. The top section of the system contains the components that control the compression probe. The probe, a long 4 mm diameter rod made of quartz, is mounted on a 10 g capacity load cell. The probe system is moved up and down (in the axial direction) by a voice coil actuator, and an optical encoder measures the position of the probe with micron-scale accuracy. The heating stage is a 1" diameter button heater made of alumina with a Pt alloy heating element, which can reach a temperature of 1000 °C at a rate of 50 °C/min. The heater is mounted on a manual X-Y-Z-θ positioning system so that a sample on the heater can be aligned with the probe. The chamber has an inlet for gas flows that are controlled by mass flow controllers (MFCs). The outlet of the system is connected to a hygrometer for measuring moisture level, a pressure sensor, and a vacuum pump. The chamber is constructed of stainless steel vacuum components with KF-style o-ring seals, and can be evacuated (using a rotary pump) to ~100 mTorr. A light source and a digital camera are positioned outside the system, looking into the front window of the chamber, to allow for experiments to be recorded *in situ*.

The probe and holder attached to the load cell must be light enough to not stretch the load cell beyond its load capacity of 10 g. As discussed in Chapter 2, very small forces are known to have a large effect on CNT growth [57], so the 10 g limit load cell was chosen because of its ability to detect small forces. In addition, the probe must be of a material that can withstand temperatures as high as 1000 °C without deformation or degradation, and prevent transmission of heat to the load cell by conduction. Thus, the probe was made out of a thin quartz rod. A light-weight collet chuck for the rod was designed and machined out of a small piece of aluminum and a collar of polyetheretherketone (PEEK) that can be easily disassembled to exchange probes (**Figure 3.1.E**). The probe and collet combined to weigh 5.52 g, which is smaller than the load cell limit. Since the hanging probe puts the load cell in tension, the amount of compression force that can be applied is equal to the 10 g limit of the load cell plus the weight of the probe. Thus, the compressive load capacity with this probe is 15.5 g. Additional static weight can be added to the probe collet to increase the weight to 10 g total to achieve a maximum compressive force of 20 g if desired.

Control of the system is performed with a LabVIEW™ program that is integrated with a National Instruments FPGA controller and data acquisition devices. An image of the LabVIEW program interface is shown in **Figure 3.2**; the right side of the interface controls the probe, and the left side controls the gas flows, heating, and moisture monitoring. The probe controls are enabled for the entire time the program is active, and they allow for position or load control of the probe, each controlled with a PID controller. For position control, the probe can move to a certain position, instantly or at a specified velocity, and can be stopped automatically if a set load is reached. For load control, the probe is moved until the specified load

is reached. Additionally, the position or load can be cycled in waveform patterns such as a sine wave or a square wave. The controls on the left side of the interface are only enabled when the "Press to Grow" button is pressed, so that the user can input a growth recipe by specifying the gas flows, temperature, and duration of each step. The program will then monitor the gas flows, temperature, and moisture level throughout the growth. The steps to use the program and perform an experiment in the Mechanochamber are described in **Figure 3.3**.

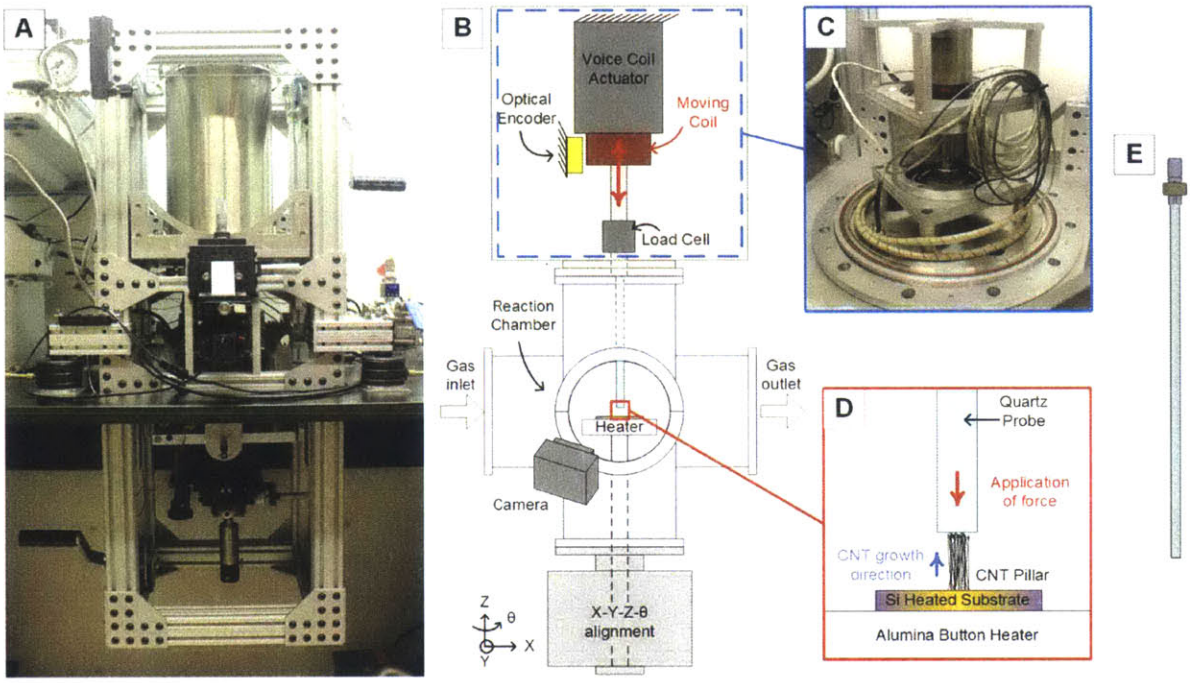

Figure 3.1 (A) Photograph of the custom-built reaction chamber for in situ compression of CNTs. (B) Schematic of the main components of the system. (C) Photograph of the microcompression system, housed inside a large vacuum cylinder. (D) Schematic of the quartz probe applying compression to a growing CNT forest.

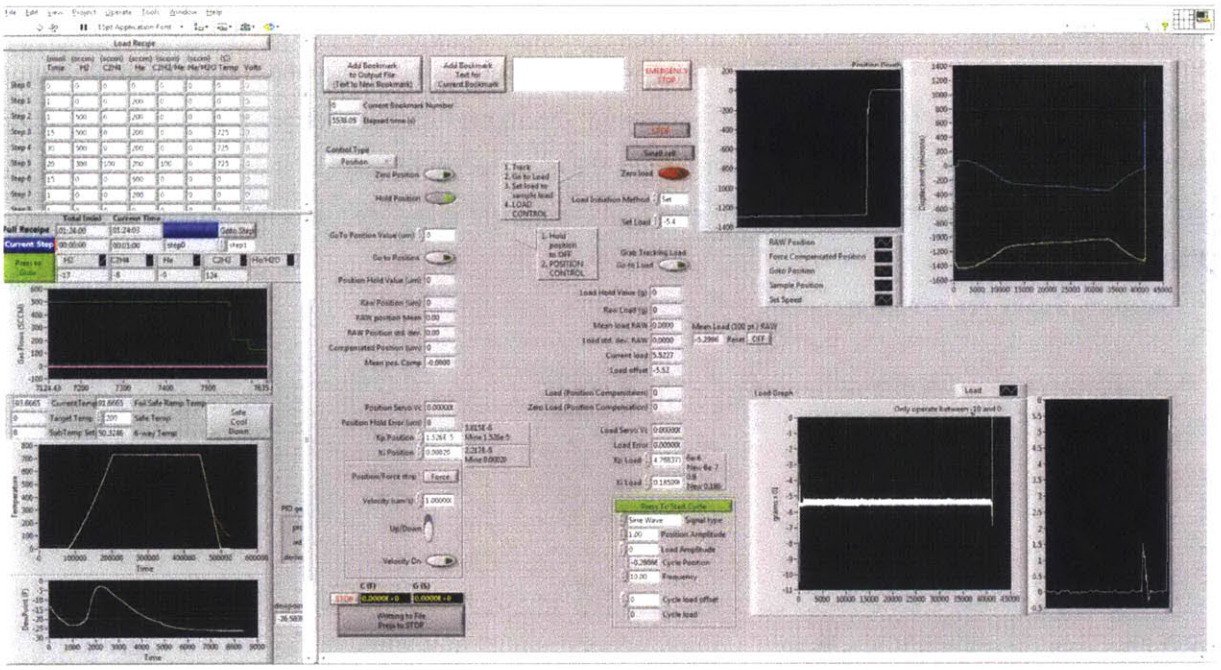

Figure 3.2 Custom LabVIEWTM program interface to control the Mechanochamber. The right side of the interface controls the microcompression system, while the left side controls the CVD components.

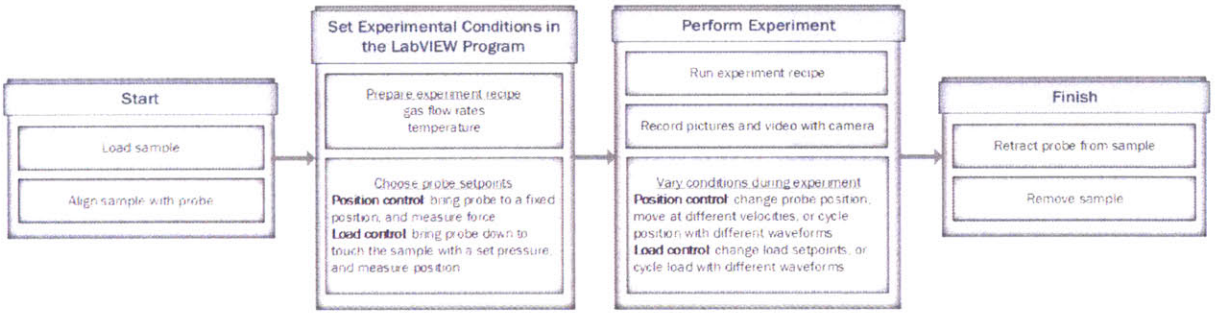

Figure 3.3 Schematic of the procedures involved in conducting an experiment in the Mechanochamber.

3.3 System Calibration and Operation

A series of calibrations were performed to ensure precise control of the microcompression and heating systems.

3.3.1 Position control

The feedback control system for the movement of the probe allows for movement to specified positions at various velocities, down to as little as 1.0 μm/s. Tests of moving the probe up and down in 50 μm increments at varying velocities are shown in **Figure 3.4**. Even when moving at high speeds of 50 μm/s, the probe does not drastically overshoot its target position. The movement of the probe is smooth at all speeds except at 1.0 μm/s, where there is a noticeably unsteady increase in the position. However, this is not unexpected when comparing to the steady-state oscillations in position, at time intervals indicated by numbered bubbles in **Figure 3.4**.Corresponding analysis of those steady-state time intervals is detailed in **Table 3.1**, which reveals that the standard deviation (of the measured signal) from the mean in position is approximately 0.5 μm. In addition, the root mean square deviation (RMSD) from the set position shares near identical values with the standard deviation, indicating that the inaccuracy in the position is caused by the imprecision in holding the position fixed. The resolution of the optical encoder is 20 nm, so the oscillations in position when no movement is desired could be due to noise in the electrical signal or a variety of mechanical factors that could cause vibrations. It can therefore be concluded that there is some amount of imprecision in the position from the limit imposed by the resolution in measuring position, but most of the time there will be control to within +/- 1 μm (two standard deviations) of the intended position.

Sample Set	1	2	3	4	5	6	7
Set position [μm]	50	0	50	0	50	0	50
μ	50.02	-0.01	49.99	0.04	49.98	0.02	50.04
σ	0.52	0.54	0.42	0.40	0.38	0.47	0.49
RMSD	0.52	0.54	0.41	0.40	0.38	0.47	0.49

Table 3.1 Variation in position of the probe when no movement is desired for seven samplings, as shown in **Figure 3.4**, with mean μ, standard deviation σ, and root mean square deviation (RMSD) from the set position.

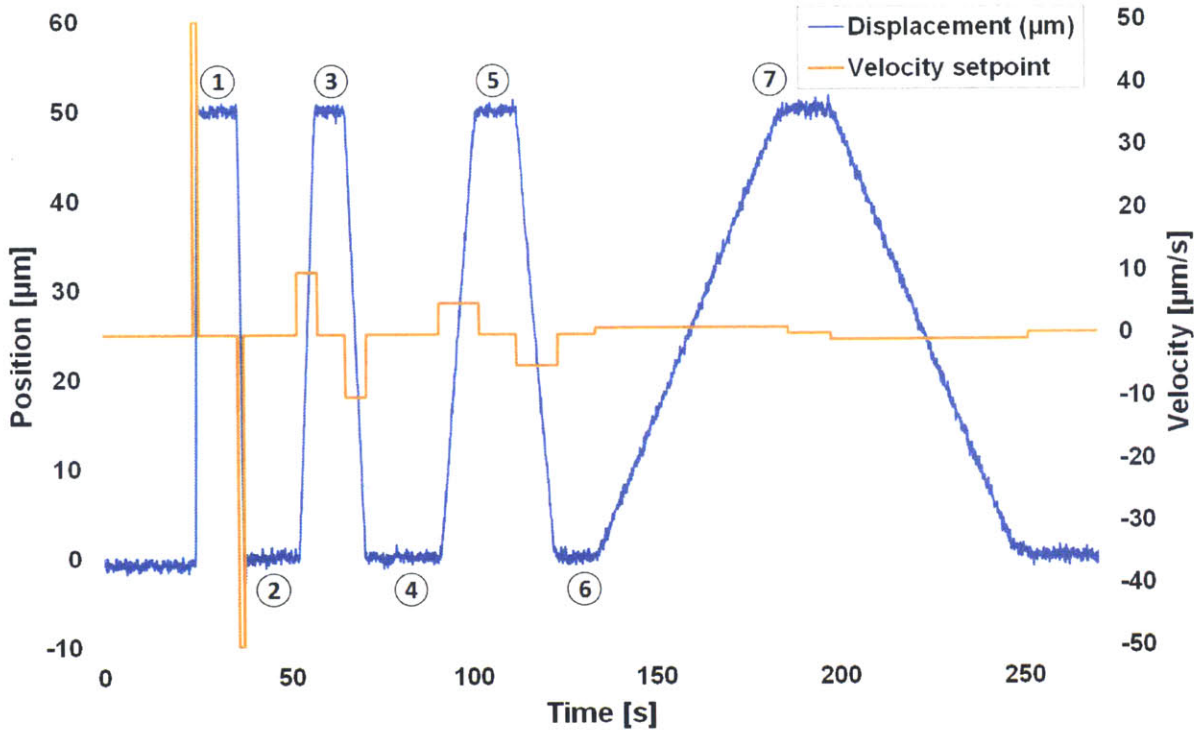

Figure 3.4 Measured position of the probe when moving up and down at different velocities. The numbers indicate the sample sets analyzed in **Table 3.1**.

3.3.2 Force control

To determine this the ability of the system to maintain a desired load, the probe was pushed against a plain Si chip mounted on the heater stage within the system, with forces increasing from 0.1 g to 15 g and back down again (stopping at 0.5 g below the 15.5 g limit of the load cell with the 5.5 g probe to prevent accidental overloading). **Figure 3.5** shows the load setpoint and the measured load throughout the experiment. The experiment was conducted by first bringing the probe down in a jump of 1000 µm and then 350 µm to approach the Si chip (the chip was at a position of a little less than 1400 µm lower than the starting position of the probe), and then lowering the probe at a rate of 0.1 µm/s until it touched the Si chip and pressed down with a force of 0.1 g. This force was maintained for a few seconds, and then the force was increased to 0.2 g, which translated into the probe being moved downwards slightly until that load was reached. This was repeated for 0.3 g, 0.5 g, 1 g, 5 g, 10 g, and 15 g, and then with those same values of force but in decreasing order. The probe first touching the Si chip caused a brief jump in load to almost 0.5 g before immediately settling down to the desired 0.1 g. Afterwards, however, there was no overshoot when

increasing the load, so there will be no unwanted overload to a sample if the load changed during an experiment.

The oscillations in load with varying setpoints are analyzed in **Table 3.2**. The average signal over the course of about 10 seconds for each setpoint shows a relatively large percent error for low forces. The manner in which the zero of the load is recorded might partially account for this. The resolution of the setpoint is to the nearest 0.1 g, and the probe weighs 5.52 g; the low-force readings are consistently a few hundredths of a gram too high, to which the extra 0.02 g would contribute. In addition, the variation in position due to inexact control might cause variations in the load that is applied. At low load setpoints, the additional downwards movement of the probe necessary to apply the appropriate compression force is small, so oscillations in the position can result in relatively large deviations from the intended load. The similarity in values between the root mean square deviations and the standard deviations, and the decline in percent error with increasing load support these assertions. The percent error seems to be larger when pressure is being lifted compared to the same load when the probe was increasing pressure. Despite the apparently large error for some loads, the standard deviations of under +/- 0.1 g for setpoints up to 1 g are quite low, especially when considering that there is a standard deviation of +/- 0.03 g when no load is applied (with the probe freely hanging). The deviations do increase with increasing pressure, as can be seen in **Figure 3.6**, but the error in the readings is very low so the applied load is fairly consistent. The system can thus apply loads of 0.1 g increments.

Set load [g]	0	0.1	0.2	0.3	0.5	1	5	10	15	10	5	1	0.5	0.3	0.2	0.1
μ	0.04	0.13	0.23	0.32	0.51	1.02	4.91	9.87	14.87	10.17	5.18	1.17	0.55	0.35	0.23	0.14
% error	-	26%	14%	6%	3%	2%	-2%	-1%	-1%	2%	4%	17%	10%	16%	15%	39%
σ	0.03	0.04	0.05	0.06	0.06	0.09	0.66	0.83	0.83	0.79	0.79	0.67	0.10	0.06	0.05	0.04
RMSD	0.05	0.05	0.06	0.06	0.07	0.09	0.66	0.84	0.84	0.80	0.81	0.69	0.11	0.08	0.06	0.06

Table 3.2 Variation in load exerted by the probe compared to different setpoints, for increasing load (blue) and decreasing load (red), corresponding to data from Fig. 3.5, with mean μ, standard deviation σ, and root mean square deviation (RMSD) from the set load.

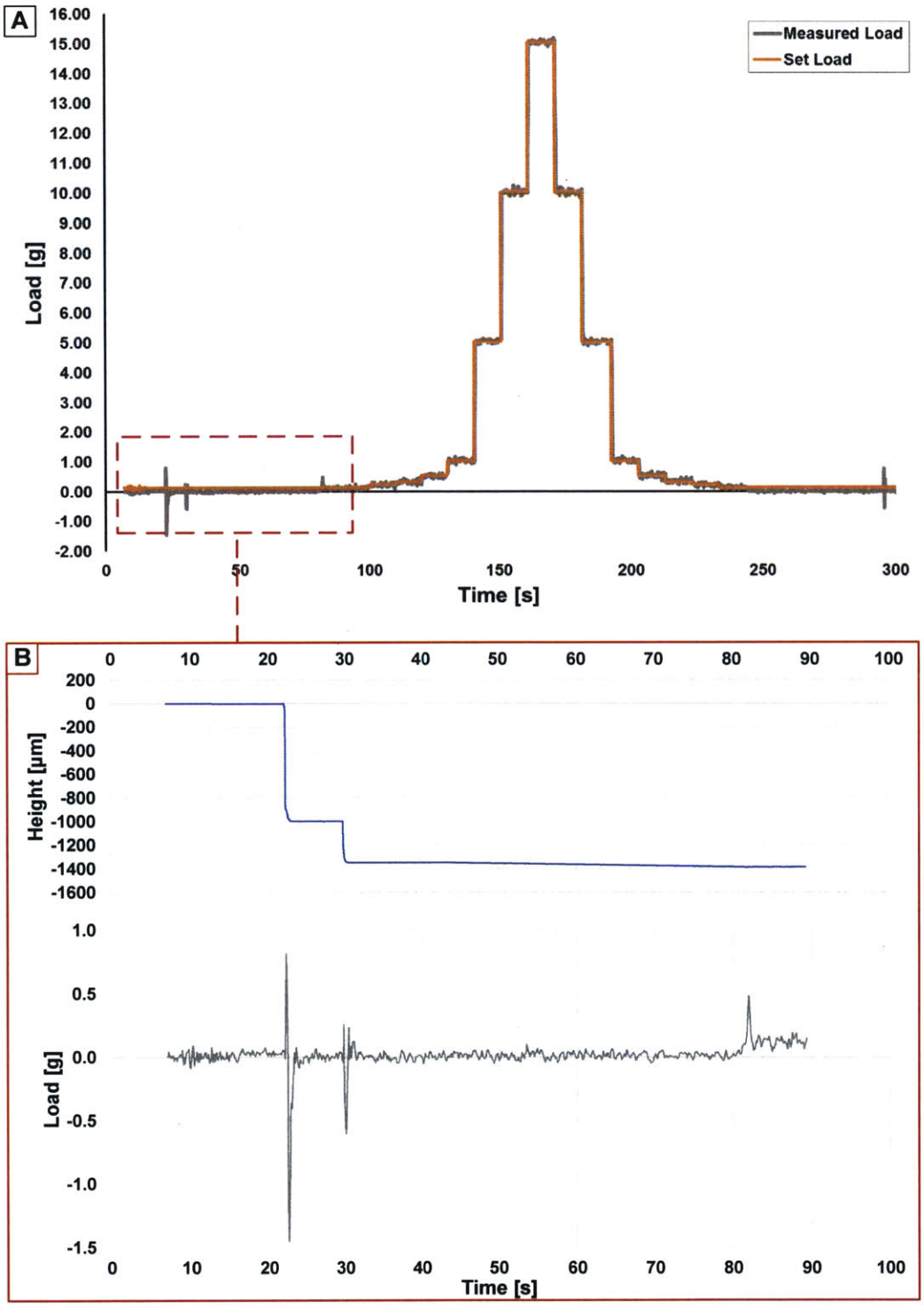

Figure 3.5 (A) Measured load exerted by the probe for given setpoints. The probe is first brought close to the sample with jumps downwards and then slowly being lowered until touching the sample (as seen in B). The probe subsequently presses down with greater force up to 15 g, and then pressure is released in the same increments and the probe is retracted.

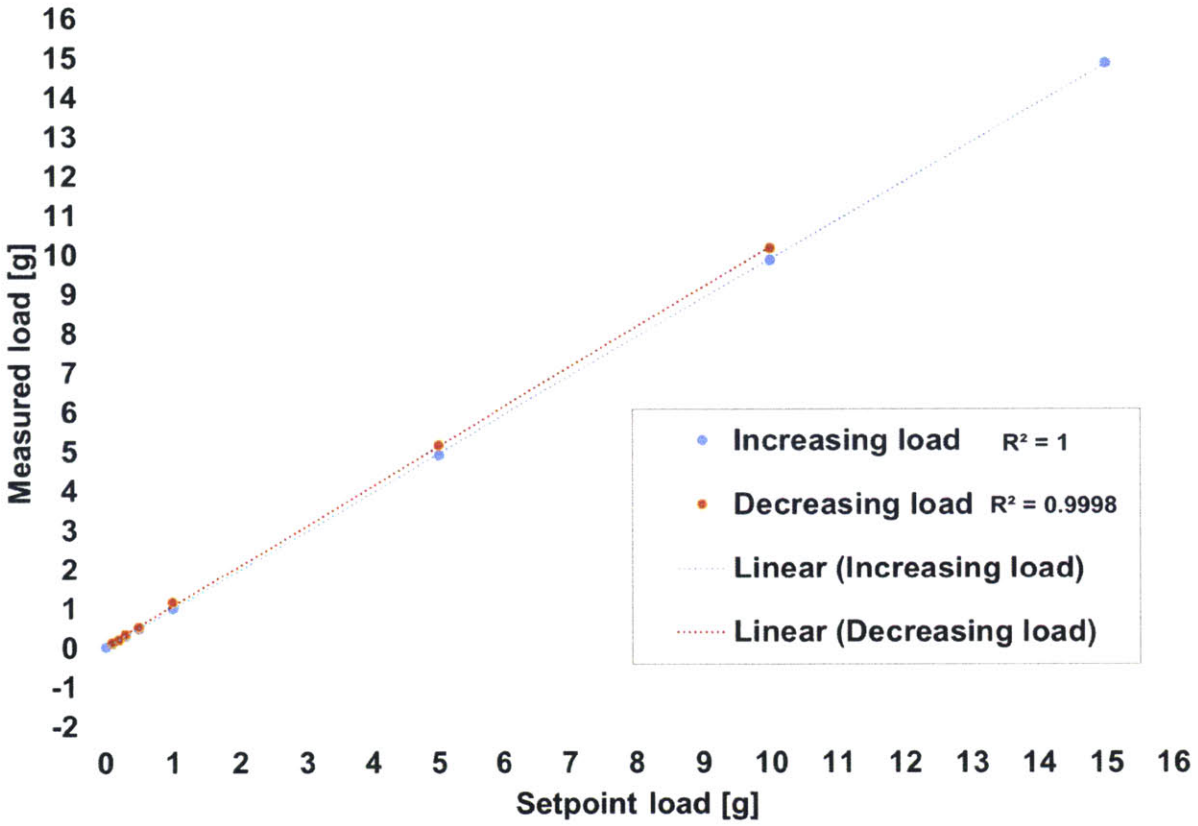

Figure 3.6 The mean values of the measured load for each setpoint of increasing load (blue) and decreasing load (red) corresponding to the data shown in **Figure 3.5**.

3.3.3 Temperature measurement

The temperature of the heater measured by a thermocouple that touches that backside of the heater, as shown in **Figure 3.7**. A feed-through thermocouple was also used to determine the difference between this thermocouple reading and the temperature at the top surface of the heater where the CNT growth substrate is placed. The feed-through thermocouple was bonded to a Si chip with a high temperature ceramic adhesive, placed in the system, and clamped to the heater surface to ensure good contact. The heater was then heated in an inert atmosphere to its 1000 °C limit and cooled back down. The difference between the front-side and back-side thermocouple measurements increased with increasing temperature, reaching as high as 50 °C. (**Figure 3.7.C**). The difference is much lower at typical CNT growth temperatures between 700 and 800 °C, but this must still be taken into account when performing experiments. Additionally, a thermocouple positioned on the outside of the 6-way cross shows that the chamber walls reach approximately 150 °C when the substrate is at 1000 °C.

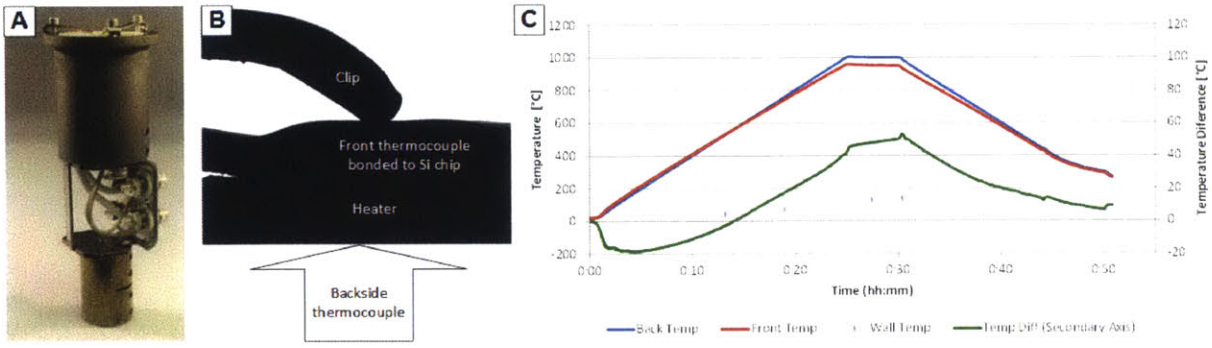

Figure 3.7 (A) Photograph of the heater along with its mounting structure and sample clips. (B) Photograph taken with the system microscope camera to show the setup for temperature calibration. (C) Temperature of the backside of the heater, frontside of the heater, and chamber wall (left axis) and the difference in measured temperature of the heater (secondary axis).

3.3.4 Performance under typical CNT growth conditions

The final calibration of the system was to measure the change in position of the probe due to thermal drift and the ability of the probe to maintain a constant load during typical CNT growth conditions, which involves variations in temperature and gas flows, depicted in **Figure 3.8.A**. The first step (blue section of the figure) involves heating the substrate to the CNT growth temperature in a mixed atmosphere of H_2 and He atmosphere. Then, those conditions are held for 30 minutes as the catalyst particles form and to allow for the position of the probe to stop changing as a result of thermal expansion of the system. After the 30 minute anneal step, hydrocarbon gases are introduced into the system to commence the CNT growth process (red section of the figure). These conditions are held until growth has terminated, which is determined by the cessation of vertical motion of the probe (in the case of constant force control). The system is then cooled slowly down to room temperature with only He flowing (green section of the figure).

For the control experiment, a bare Si chip was placed in the system to observe the effects of CNT growth conditions on the height and load measurements of the probe. The probe was pressed down against the Si chip throughout the experiment with a set load of 0.1 g. **Figure 3.8.B** shows the measured position and load of the probe during the experiment. Thirty minutes was enough to accommodate for the thermal drift of the system, as the height of the probe stayed consistent towards the end of the anneal step. However, during the growth step the probe drifted upwards 43 μm. This was probably caused by the change in atmosphere, with the introduction of hydrocarbon gases and the reduction of helium and hydrogen gas flows are reduced while maintaining the same overall gas flow rate. The thermal conductivity of hydrocarbons is much lower than that of lighter gases (e.g. at 500K and 1atm, 0.05 W/m·K for ethylene [69] compared to 0.22 W/m·K for He and 0.27 W/m·K for H_2 [6]). This change in atmosphere will decrease the convective heat loss around the heater, increasing the temperature at the top of the heater and of the Si chip compared

to the setpoint growth temperature, and resulting in further thermal expansion of the system. A previous cold-wall CVD system constructed by Hart also displayed this sensitivity in atmosphere when changing amongst He, H_2, Ar, and Air atmospheres [70]. The thermal drift continued for about 15 minutes, indicating that the measured growth kinetics during the very early stages of a CNT forest might be inaccurately high because of thermal expansion. The measured load throughout the experiment stayed consistent and did not vary due to changing temperatures and gas flows, indicating the reliability of force application in CNT growth conditions.

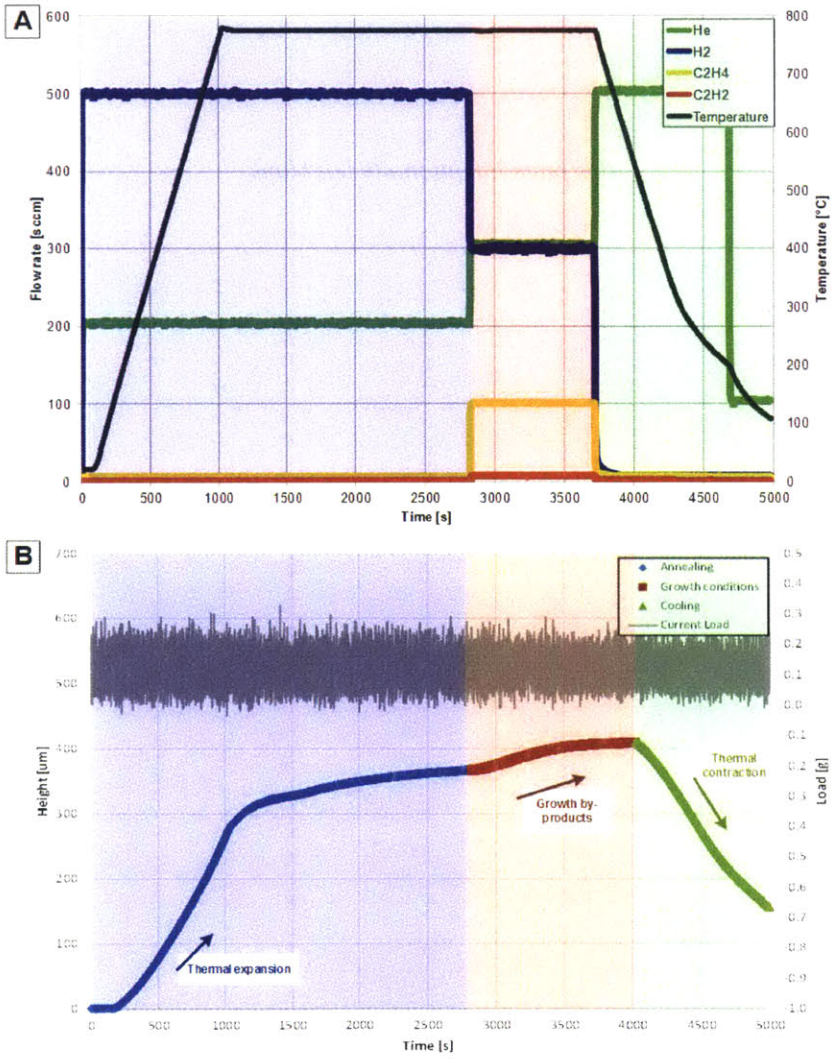

Figure 3.8 (A) Gas flows and temperature profile for a characteristic CNT growth experiment in the Mechanochamber. The blue regime is the heating and annealing step, red is the growth step, and green is the cooling step. (B) The position of the probe and its load when replicating CNT growth conditions but without catalyst in order to determine a baseline.

this page intentionally left blank

Chapter 4 Force-Modulated Growth of Carbon Nanotube Forests

In this chapter, the potential mechanochemical effects of force on CNT growth are explored by applying compressive forces to CNT forests during growth in the Mechanochamber. This chapter will first describe the experimental procedure used to apply compression to CNT forests during growth, and then discuss how to interpret the measured height vs. time results to determine the growth kinetics. Experiments conducted using static compressive forces reveal that the average forest growth rate decreases from 0.23 μm/s to 0.03 μm/s for increasing applied forces of 0.3 g and 10 g, respectively. In addition, the forest can be described by three regimes according to the amount of force applied: for low forces the forest grows at a high rate and maintains its structure; for moderate forces the forest grows at a high rate until buckling during growth, subsequently growing more slowly; and for high forces the forest grows slowly in a collapsed configuration. Finally, studies of growth under time varying-forces reveal that a single, sudden increase in the load during growth will cause a decrease in growth rate without inducing immediate termination of the growth, and a decrease in the load can cause the growth rate to temporarily increase.

4.1 Methods

This section details the experimental setup and procedure to grow CNT forests in the Mechanochamber system presented in Chapter 3.

4.1.1 CNT Catalyst Preparation

To prepare samples for CNT growth, a 4" (100) Si wafer with 300 nm of a thermally grown oxide layer is used as the substrate, with Al_2O_3 and Fe catalyst layers of thickness 10 nm and 1 nm, respectively. If a certain CNT forest structure is desired, the catalyst is patterned before deposition of the Al_2O_3 with photolithography techniques by applying positive resist SPR 700 to the Si wafer. After resist development, the Si wafer is coated with the Al_2O_3 followed by the Fe catalyst layers using electron beam evaporation. The wafer is then diced with a dicing saw into samples of size 10 mm × 10 mm. The patterned samples require an additional lift-off procedure to rid of the photoresist before conducting an experiment, by placing the sample in a beaker of acetone and into an ultrasonic bath, repeated with fresh acetone and then rinsed with isopropanol and blow-dried with a stream of N_2 gas. The Fe layer develops into appropriate catalyst nanoparticles during the annealing stage of an experiment. **Figure 4.1** shows pictures of a Si chip with patterned catalyst before and after CNT growth.

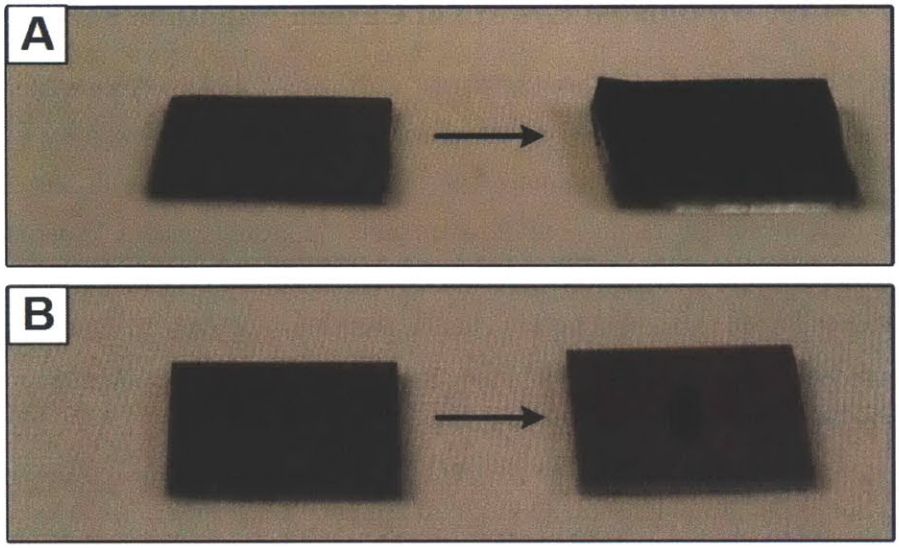

Figure 4.1 Photographs of Si chip samples before and after CNT forest growth, for samples prepared (A) with unpatterned catalyst and (B) catalyst patterned with a single 1 mm diameter circle in the center.

4.1.2 Procedure for CNT Forest Growth in the Mechanochamber

CNT growth in the Mechanochamber requires a series of preparation and alignment procedures:

1. The chamber is "baked out", which involves heating the closed system to a high temperature (typically 900 °C) for 20 minutes to burn away carbon deposits remaining in the system from previous experiments.
2. The microcompression assembly is raised and the heater stage assembly is lowered with the hand cranks to allow access to the assemblies outside the chamber.
3. The probe and heater are cleaned and wiped with acetone to ensure all contaminants are removed.
4. The sample is placed onto the heater and clamped into position with clips.
5. The heater and microcompression assemblies are re-positioned inside the chamber.
6. The stage is aligned with the probe using the X-Y-Z-θ positioning system of the stage. The stage should be moved so that the probe is centered above the sample, and the stage tilted so the bottom surface of the probe is coincident with the sample surface.
7. The chamber is sealed.
8. The system is pumped down for 1 hour with the vacuum pump to under 100 mTorr to rid of contaminants that had entered the chamber during sample loading
9. The gas lines to He, to the system, and through the hygrometer are opened
10. The system is purged with He to return the chamber to an inert environment and to flush the hygrometer to a baseline before the growth begins.

11. The gas lines to the mass flow controllers (MFCs) are opened.

The experiment can then proceed with the steps as described in **Figure 3.3**: the probe is brought down to touch the sample surface and aligned with the catalyst if necessary; a standard growth recipe of gas flows and temperatures is selected or created (**Table 4.1**); and the grow command is given by the LabVIEW program. To accurately measure the height of the forest *in situ*, the probe must be in contact with the forest at all times during growth. To enable this, the probe must press down and maintain a small force throughout. From the force control calibration experiments in Chapter 3, it was determined that a 0.1 g load was sufficient for this purpose. The probe is also used to press against the substrate surface and cover the catalyst during the annealing step before each growth in order to prevent excessive heat dissipation in the cold wall system and to allow for the catalyst particles to properly form. The resulting height measurements (**Figure 4.2**) reveal the CNT forest growth kinetics for a typical growth. Images taken *in situ* with the system digital camera are shown in **Figure 4.3**. When the CNT forest has finished growing, the growth step is ended and the system is cooled down to below 30 °C, at which point the probe is slowly moved upwards away from the forest at a rate of 1 μ/s.

Step	Time [min]	He [sccm]	H2 [sccm]	C2H4 [sccm]	1% C2H2 (He carrier) [sccm]	Temperature setpoint (°C)
Purge Gas Lines	1	200	500	0	0	0
Heat	15	200	500	0	0	725
Anneal	30	200	500	0	0	725
Grow	70	200	300	100	100	725
Ramp temperature down	15	500	0	0	0	0
Cool to room temperature	20	200	0	0	0	0

Table 4.1 Typical CNT forest growth recipe, listing gas flow rates and temperature setpoint (ramp at 50 °C/min).

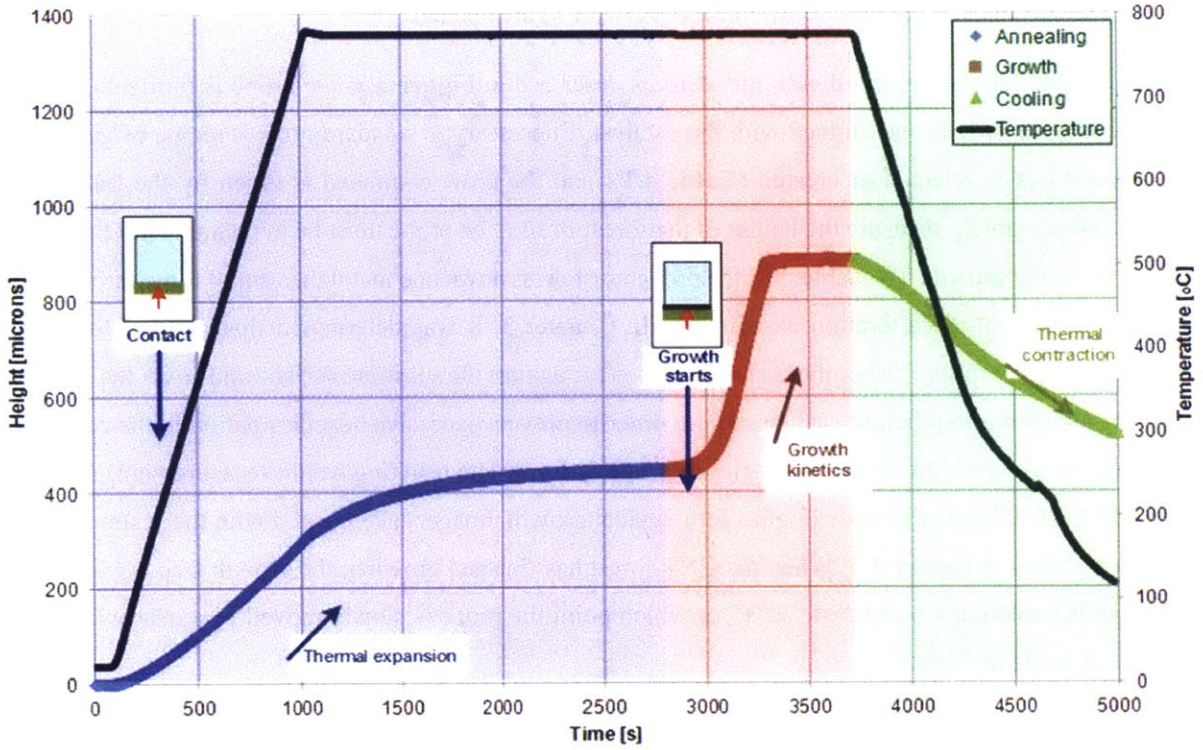

Figure 4.2 The height of the probe and temperature profile during a CNT growth experiment.

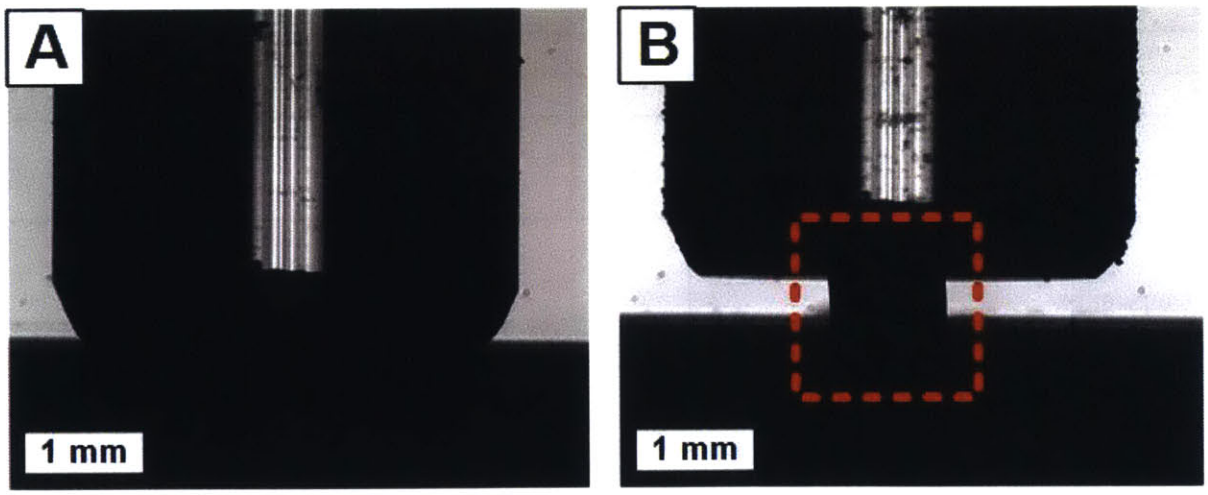

Figure 4.3 Photographs taken with the in situ digital camera microscope of 1 mm diameter pillar sample loaded in the Mechanochamber (A) before CNT growth begins and (B) after growth, with the CNT pillar highlighted in red.

4.1.3 Application of Compressive Force during CNT Growth

The Mechanochamber system as described in the previous chapter was used to perform experiments where a controlled compressive force was applied to the top surface of a CNT forest while monitoring the height kinetics. To ensure a constant pressure across the CNT forest was maintained so that the force could be distributed as equally as possible, substrates containing catalyst patterned in a single a 1 mm diameter circle (as shown in **Figure 4.1**) were used. These circles could then be centered underneath the 4 mm diameter probe inside of the Mechanochamber so that a constant pressure can be maintained across the forest (**Figure 4.3**).

Assuming equal distribution of force amongst the CNTs in the forest, the force acting on each CNT can be computed from

$$F_{\mathrm{CNT}} = \frac{mg}{N_{\mathrm{CNT}} A_{forest}} \tag{4.1}$$

where m is the applied load (in mass units), g is the gravitational constant, N_{CNT} is the CNT areal number density (CNTs/cm^2) of the forest, and A_{forest} is the area of the top of the forest that the force is acting upon. **Table 4.2** lists corresponding pressures for some values of force within the 0.1-10 g range that was used in experiments. **Figure 4.4** shows plots of the force per CNT for a range of applied forces and forest densities, and can be used to estimate the force per CNT for a given applied force. For instance, assuming a forest density of 10^{10} CNTs/cm^2, the force per CNT under 12.5 kN/m^2 compression is approximately 0.1 nN.

Force [g]	Applied Pressure [kN/m^2]
0.1	1.2
0.3	4.0
0.4	5.1
0.5	6.4
0.6	7.5
0.7	8.6
0.9	11.4
1.0	13.0
1.5	19.1
2.5	31.5
4.0	50.0
5.1	63.8
7.0	87.0
10.0	125.0

Table 4.2 Corresponding pressures for the range of static forces applied in the compression of 1 mm diameter CNT pillars during growth.

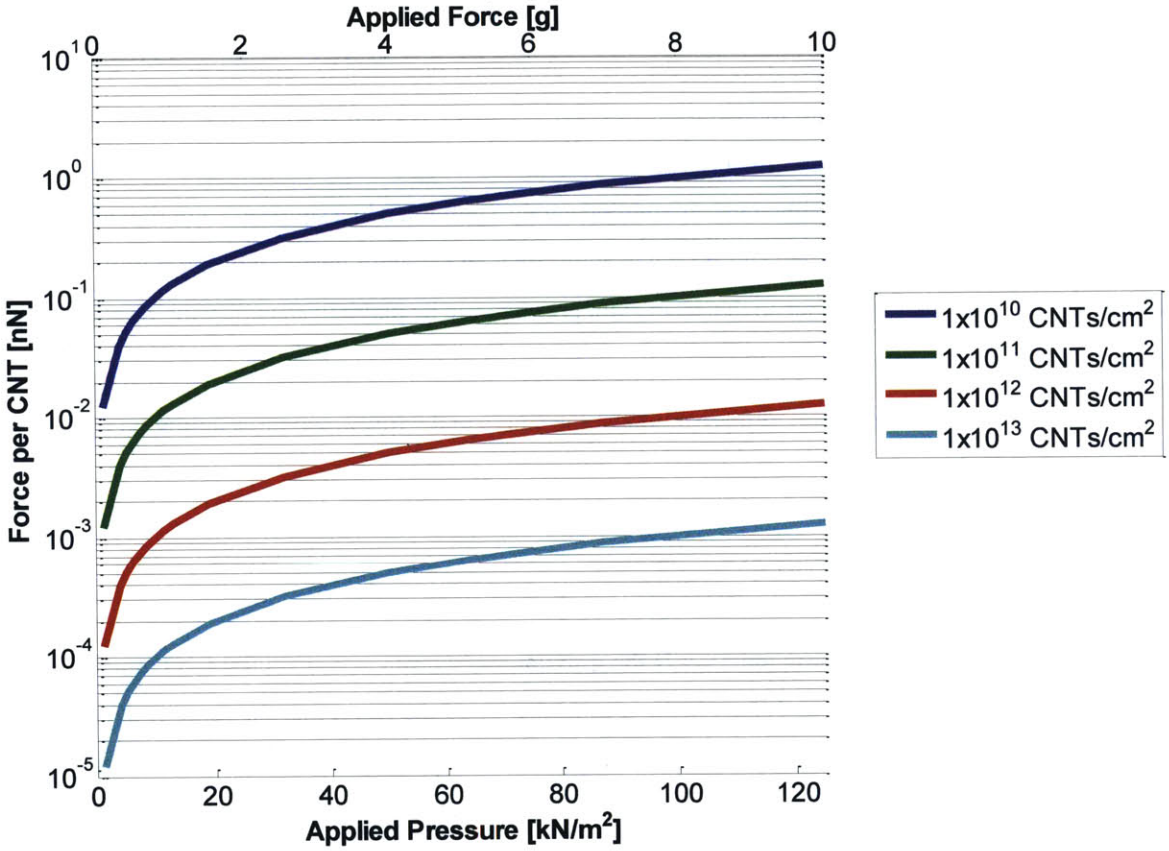

Figure 4.4 Average force per CNT for application of pressure on the top of a 1 mm diameter CNT forest pillar, for different CNT number densities.

4.2 Determination of Kinetics from Recorded Data

The height of the probe as measured throughout an experiment is used to determine the kinetics of the CNT forest growth, approximated as the change in height of the CNT forest. The height vs. time data for only the growth step of the experiment (the red section of **Figure 4.2**; after the carbon source is introduced) is isolated as shown in **Figure 4.5.A** for a representative CNT growth under static compression. The instantaneous growth rate of the forest, represented by motion of its top surface, can be obtained by numerical differentiation of the height with time using the simple difference quotient

$$V_{1\to 2} = \frac{h_2 - h_1}{t_2 - t_1} \tag{4.2}$$

where $V_{1\to 2}$ is the instantaneous growth rate, h is the height, and t is the time.

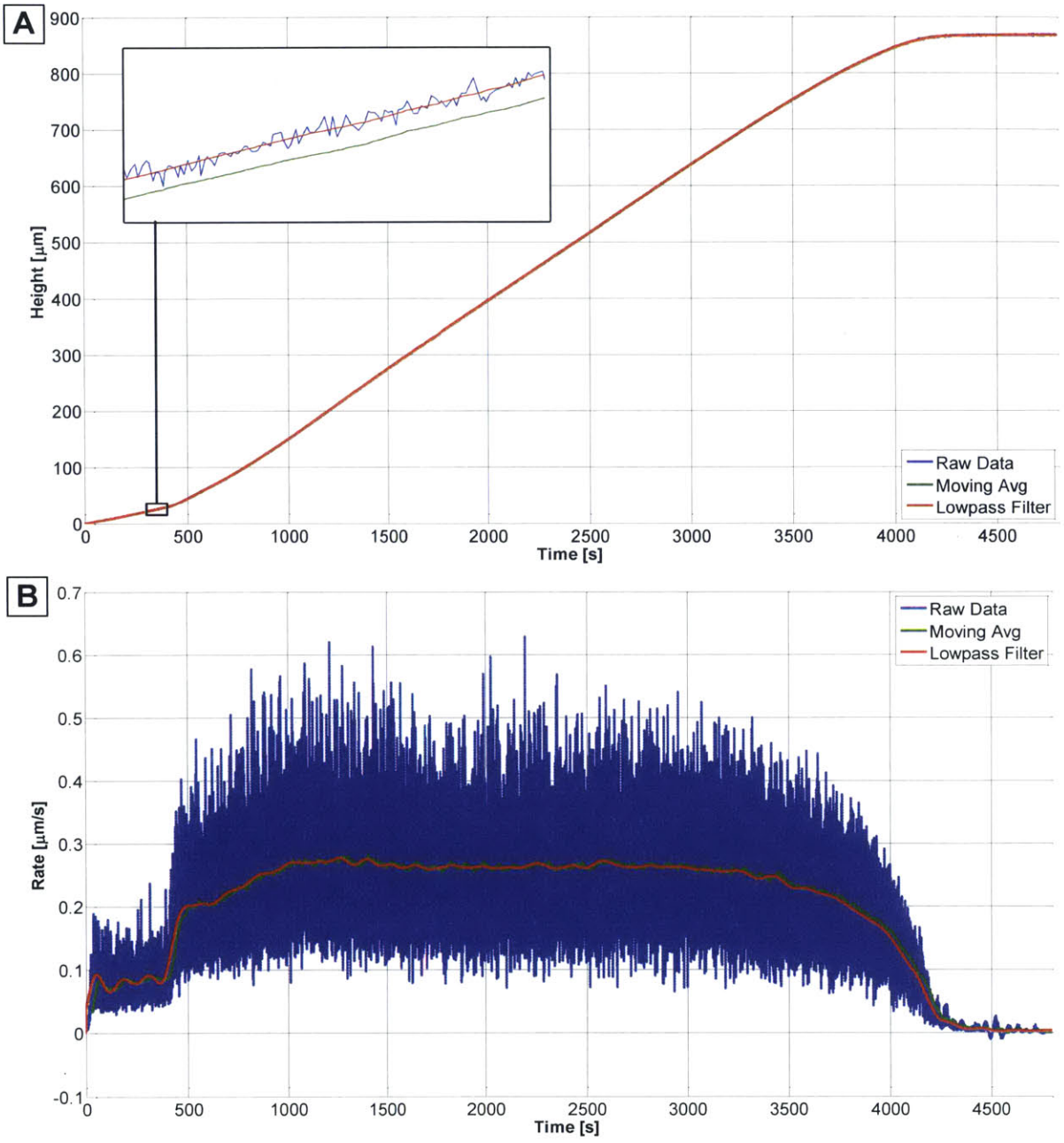

Figure 4.5 For a nominal growth of a CNT pillar under static compression, (A) height vs. time with two different smoothing methods (discernible in the inset), and (B) kinetics from numerical differentiation of the filtered height data, where "Raw Data" refers to no smoothing of the kinetics curve.

However, noise in the height measurement must be filtered in order for the numerical derivative to be an accurate estimate of the instantaneous growth rate. Two methods of signal smoothing were compared, one based on a simple moving average and another based on a lowpass filter. A third option would be to fit the height data to a smooth function then differentiate that function as an estimate of the rate. However, forces cause abrupt changes in the growth rate so approximation by a smooth function is not always possible without using a high order polynomial, and thus this method was not studied.

The simple moving average uses a lag in the beginning as the averaging window; values ranging from 10 to 1000, with 500 as the one typically used, were investigated. The lowpass filter was based on a Butterworth filter of order 12 and varying cutoff frequency for the point 3 decibel points below the passband value, in normalized frequency units of (π rad/sample). These smoothing methods still cannot recover the characteristic kinetics from the differentiated raw height data. Therefore, the height data must first be smoothed before taking the numerical derivative. The zoomed-in areas of **Figure 4.5.A** show that the moving average smoothing method with an averaging window size of 500 results in a significant delay of a few seconds, especially for the early data. By increasing the lag, the moving average appeared to better retain the shape of the kinetics data than the low-pass filter, but at a cost of increasing delay.

A lowpass filter was thus used to smooth the height data before numerical differentiation, which subsequently reveals some characteristics of the kinetics but still with far too much noise (**Figure 4.5.B**). Smoothing the rate data with a moving average showed the same characteristic delay as when applied to the height data. This is especially noticeable for the sharp jumps that are stretched by the moving average, which is a very negative effect for analyzing the kinetics as much of the interesting kinetics data occurs at these jumps. Therefore, a low-pass filter was chosen as the method to smooth the rate data as well. Finally, the cutoff frequency for the low-pass filter on the rate data was optimized. **Figure 4.6** shows that the higher cutoff frequencies of 0.01 and 0.005 display a large amount of noisy oscillations, especially at the relatively constant rate above 0.25 μm/s, but a cutoff frequency of 0.001 is not able to adequately follow the true kinetics, so 0.003 was chosen as the cutoff frequency.

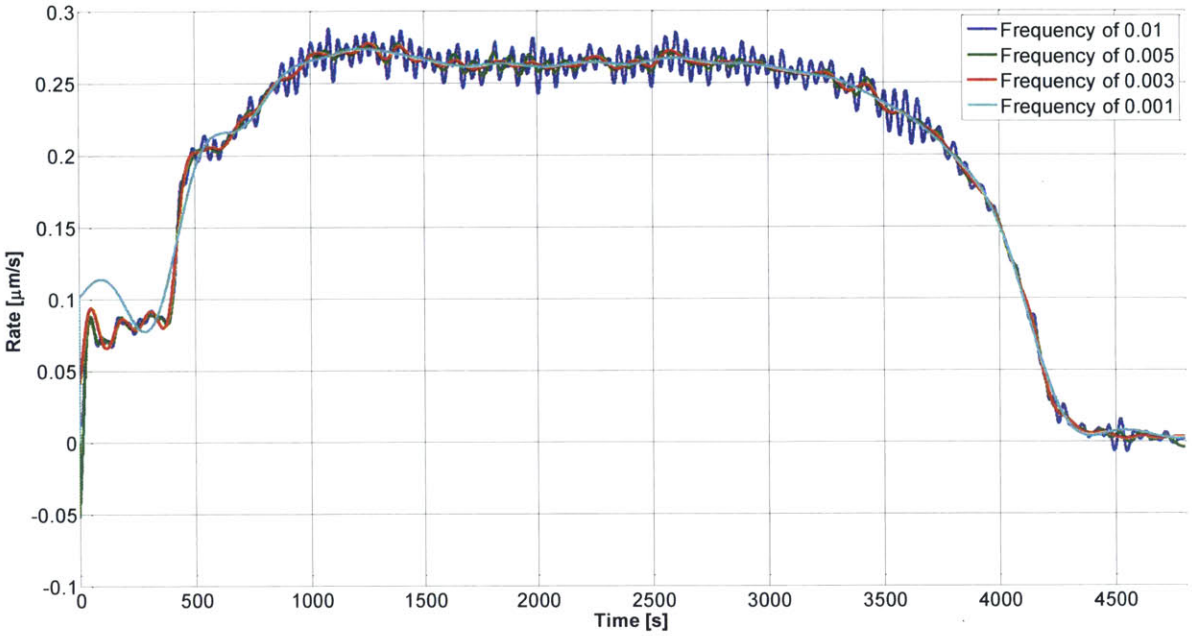

Figure 4.6 Smoothing of the kinetics of a nominal growth using low-pass filters of different frequencies.

4.3 CNT Forest Growth under Constant Compression Forces

A series of experiments was conducted to determine how the growth of CNT forests may be affected by external loads. Specifically, this series sought to answer if there is a correlation between applied load and CNT growth rate (as measured by height increase), and how the force may affect the CNT forest morphology. This was achieved by growing CNT forests under a constant force that was changed for each experiment, ranging from 0.1 g to 10 g (corresponding to pressures of 1.2 to 125 kN/m^2 as given in **Table 4.2**), according to the procedure described in **Chapter 4.1**. Each experiment was performed with the same operating procedure to attempt to remove variations amongst experiments. In particular, there were concerns of how variations in the moisture level of the system could affect run-to-run variability, as moisture level in the system has been shown to have a large impact on the growth results [71]–[73]. During this sequence of experiments, the average and standard deviation of the temperature of the room was 24 +/- 2 °C, of the relative humidity of the room was 62 +/- 7%, and of the dew point measured in the outlet of the reaction chamber was -22 +/- 3 °F.

4.3.1 Overall Trends in the Effects of Force

The heights of the CNT pillars throughout the growth experiment as measured by the probe displacement are plotted in **Figure 4.7.A**, with the corresponding growth kinetics curves in **Figure 4.7.B**. The data is processed using a low-pass filter with 0.003 cutoff frequency. First, it is known that CNT forest growth begins by accumulated nucleation of individual CNTs which self-organize into a vertically aligned configuration then begin collective upward growth. In the Mechanochamber, CNTs are initially in contact with the bottom surface of the probe yet the gap between the probe and surface varies. Therefore, vertical motion of the probe is recorded when CNTs can collectively exert enough force to displace the probe, and a sharp increase in the growth rate is noted after a short time. This can be attributed to self-organization of the CNTs, which should have greater ability to exert force and therefore displace the probe while maintaining the constant force imposed by the control system. After some time, the collective forest growth rate decreases until the measured forest height is no longer increasing with time, indicating the growth has terminated. For example, for the growth under a 0.3 g force, after 500 seconds the growth rate increases to 0.2 μm/s, then increases further to a maximum of 0.28 μm/s, then decreases rapidly after a total time of 3200 s.

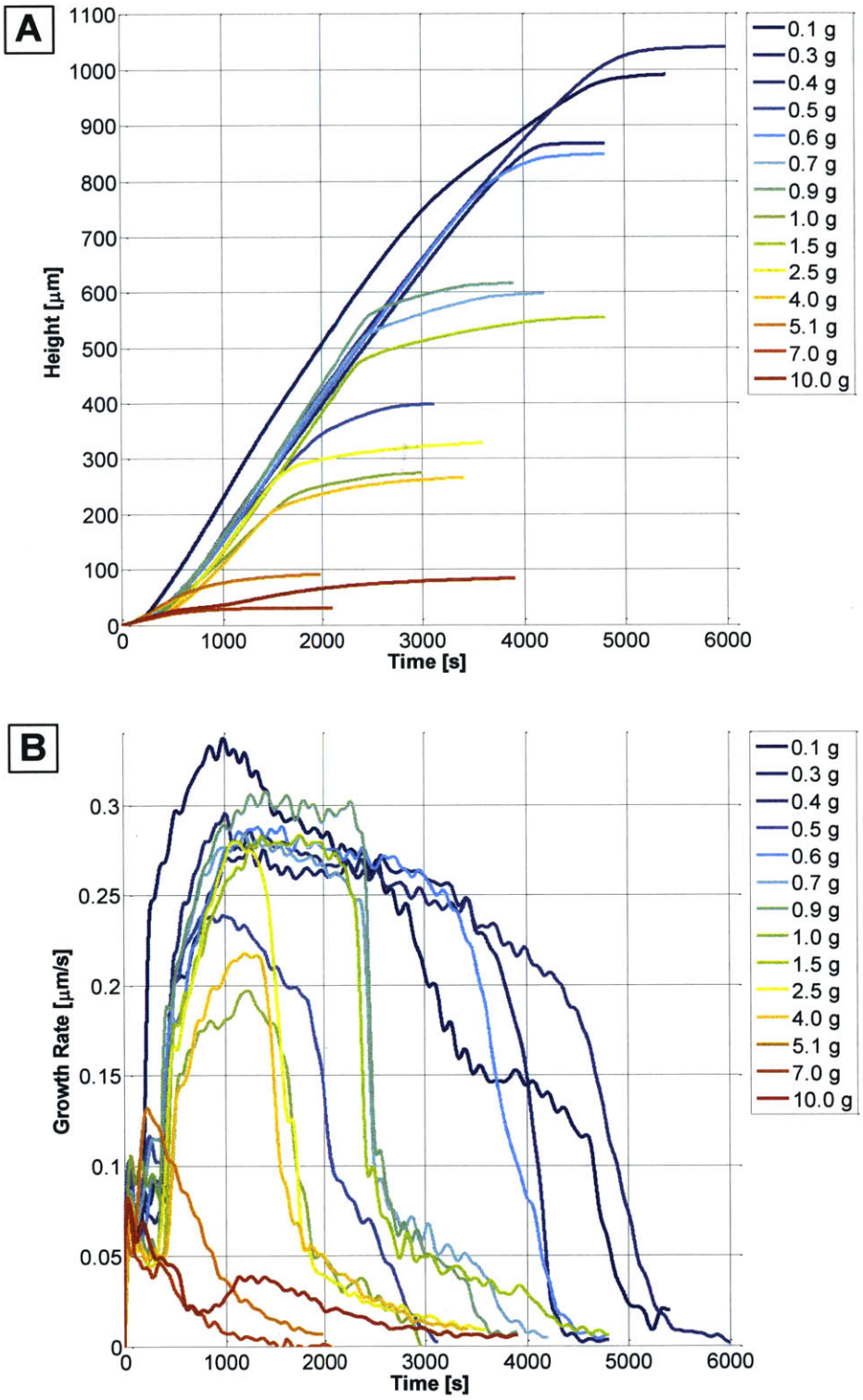

Figure 4.7 (A) Height and (B) corresponding kinetics for a series of CNT pillar growths under different static compressive loads.

The maximum CNT forest height, which is the height measured *in situ* at termination of growth, is plotted in **Figure 4.8.A**, and is 1040 μm and 31 μm for the 0.4 g and the 7 g growths, respectively. There is a general trend of decreasing forest height with increasing applied force in the constant force experiment series. The maximum growth rate, which is expected to be achieved shortly after lift-off of the collective forest and early in the growth, is plotted in **Figure 4.8.B**. The fastest growth rate is 0.34μm/s as under 0.1 g load, while the 10 g load resulted in a maximum rate of 0.08 μm/s. The maximum growth rate is also found to decrease with increasing applied force, though with some notable scatter in the values for small forces.

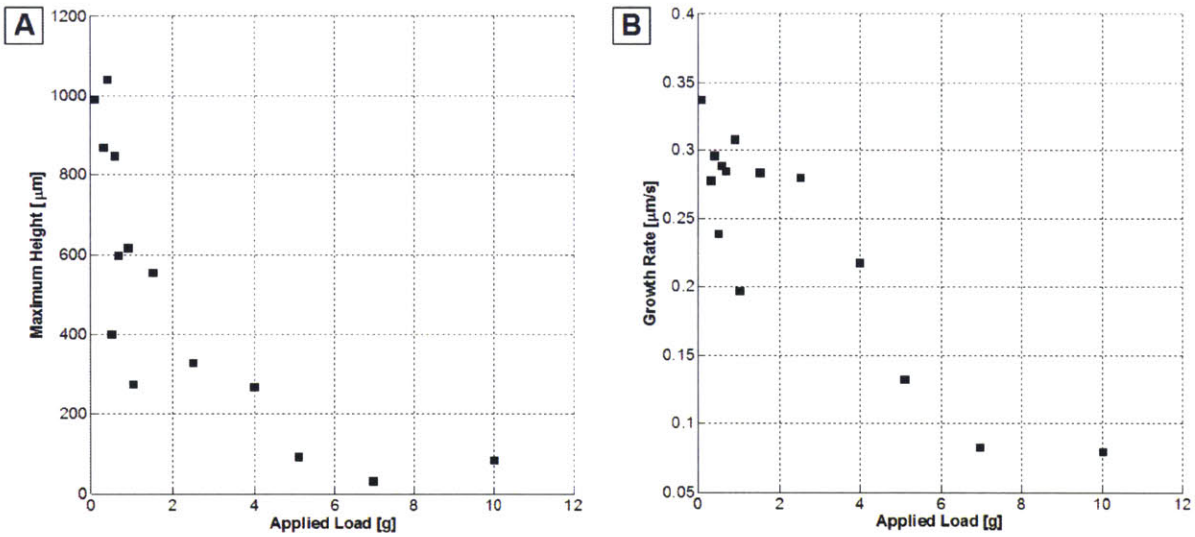

Figure 4.8 Maximum (A) forest height and (B) growth rate for each experiment under a static compressive load.

From this data, it is evident that external forces can retard the growth rate and terminal height of CNT forests. The effect is especially evident in looking at how much the termination height changes with increasing small applied forces. For instance, an increase from 0.1 g to 0.7 g results in a forest growing to 1000 um to only growing 600 um. Run-to-run variations could partially contribute to these changing heights; for example, different humidity levels in the system will cause differences in the development of catalyst particles since humidity has been shown to affect the dewetting and annealing of the catalyst [72]. Despite this, there is a dramatic decline in height that is consistent for the collective experiment set.

A closer look at the height and kinetics curves reveals some common characteristics. **Figure 4.9** shows a plot of the height and growth rate vs. time for one of the growths, during which a 0.9 g static compressive force was applied. The initial height increase is most likely due to thermal expansion of the

system resulting from the changing gas environment, as detailed in **Chapter 3.3.4**. There is then a sharp increase in growth rate to the point circled in black on the curve, as the CNT density reaches a point that allows for it to withstand the applied load and push back against the probe. The rate then slowly increases to a maximum as the CNT density continues to increase after self-organization as shown by Bedewy *et al.* [27]. The forest will continue to grow at a high rate until the onset of termination and the growth rate rapidly drops. In experiments with moderate forces, a sharp change in the shape of the height versus time curve is noted by the sharp decrease in the growth rate; this corresponds to the CNT forest buckling at the base as seen in the SEM image of **Figure 4.12.G**. The forest continues to grow upwards, but at a much slower rate as individual CNTs continue to grow in a much more tortuous manner. The growth rate continues to decline as the growth of more individual CNTs is halted until eventually there is termination of the collective forest growth, marked by the black cross-mark on the rate curve.

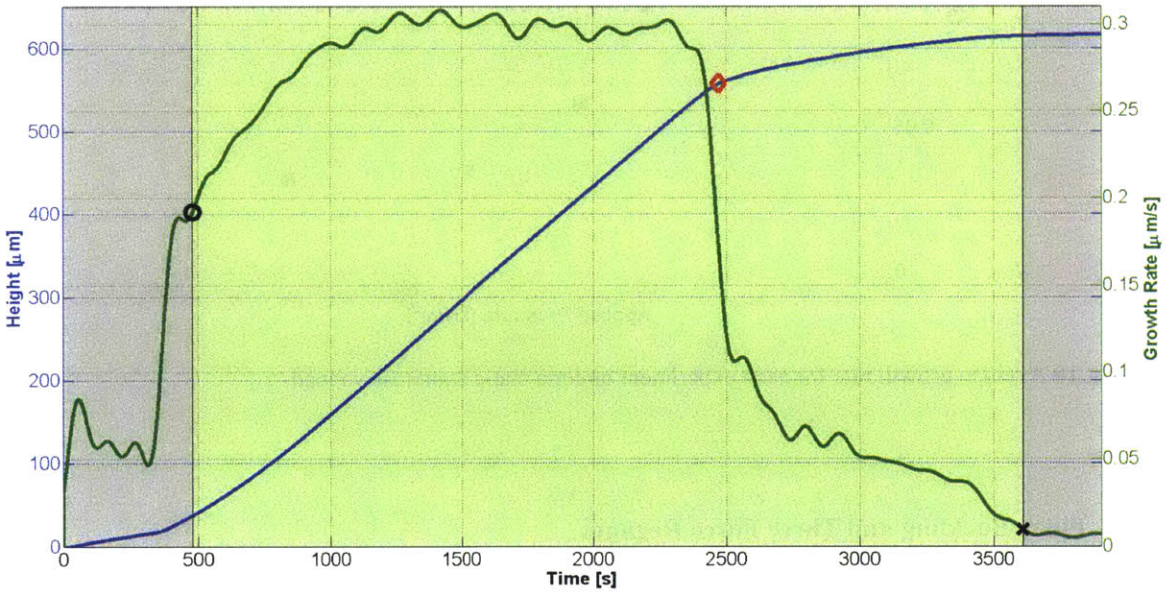

Figure 4.9 Height (blue) and growth rate (green) for a representative growth of a CNT pillar under a moderate static compressive load. The red diamond on the height curve highlights the point at which buckling first occurs. The green region represents the time period that was used for determining the average growth rate.

The average growth rate can be determined by averaging the growth rate for the time period shown only in the green region and excluding the gray regions denoting the initial measured rate and the rate after termination. The average growth rate for all of the experiments is shown in **Figure 4.10**, ranging from 0.23 μm/s to 0.03 μm/s for applied forces of 0.3 g and 10 g, respectively. This shows a clearer trend in decreasing

rate with increasing pressure than the plot of maximum growth rate with pressure, since the average rate takes into account the effect of force on the longevity of the growth and the onset of buckling.

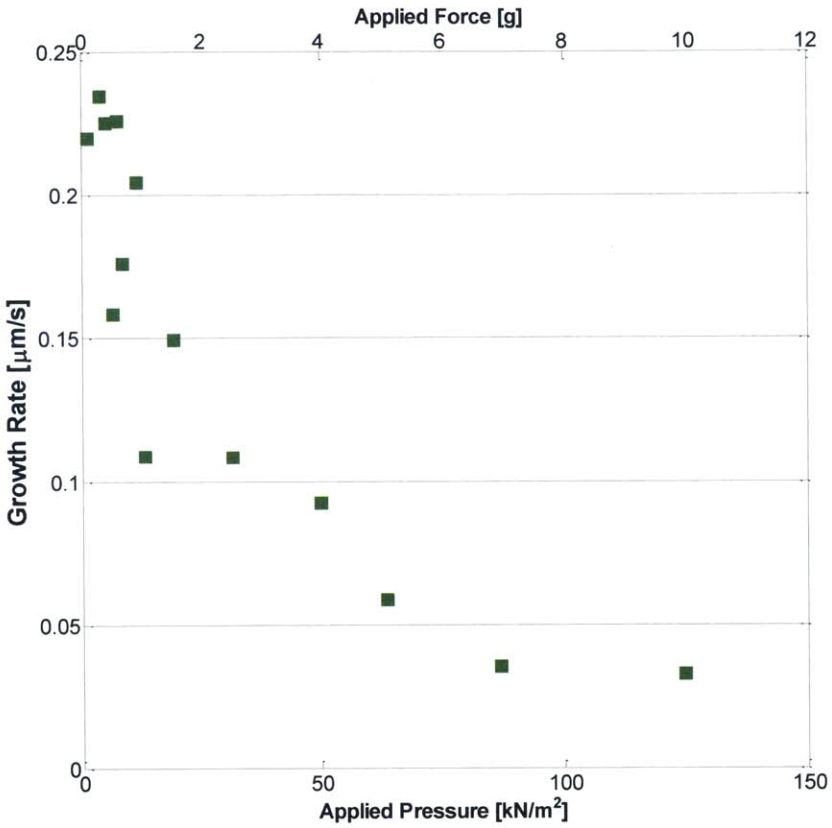

Figure 4.10 Average growth rate for each experiment under a static compressive load.

4.3.2 Pillar Buckling and Three Force Regimes

It is found that the kinetic behavior under constant applied force, as measured by the CNT height, can be divided into three regimes ranked according to the magnitude of nominal applied pressure:

- Regime I: 0.1-0.6 g, equaling 1.2-7.5 kN/m^2 over the area of the pillar
- Regime II: 0.7 g to 4 g, equaling 8.7-50 kN/m^2
- Regime III: 5.1 g to 10 g, equaling 63.7-124.9 kN/m^2

Figure 4.11 shows a summary of the growth kinetics of representative samples from each of the three regimes. Scanning electron microscope (SEM) images of representative samples from each regime are shown in **Figure 4.12**. These images show the relative height difference among the three cases, and

evidence of the buckling as indicated by ripples in the side walls. The low force (0.4 g) growth does not show evidence of buckling; though there is a crease near the bottom. The crease does not wrap around the whole pillar and it does not show CNTs buckled underneath. The moderate force (1.5 g) growth shows clear buckles near the bottom, supporting the assertion that the kink in the height curves and the sharp drops in rate correspond to the pillar buckling during the later part of growth after CNT density at the base has declined due to catalyst deactivation. Finally, the growth under 10 g shows buckles throughout the height of the pillar.

For Regime I (low applied forces), a growth rate near the maximum is maintained for a large portion of the growth. The shape of the corresponding height vs. time curves is similar to previous work where no external load is supplied. In these studies, it was found that abrupt termination of growth occurs when the density at the base has decayed such that the CNTs that remain growing can no longer support the growth of the collective forest [74]. In the force-controlled experiments, this is indicated by the abrupt flattening of the height curve and drop of the growth rate to zero.

If a moderate amount of force is applied (Regime II), the forest buckles sometime after growing at a high rate. This is observed by a kink in the height curve, and by the rapid drop in growth rate followed by sustained growth at a much lower rate. The SEM image in **Figure 4.12.G** for growth under moderate force shows clear buckles at the bottom of the forest, supporting the assertion that the kink in the height curves and the sharp drops in rate correspond to the pillar buckling during the later part of growth after CNT. After this time, CNTs continue to grow in a tortuous geometry so that the collective forest increases in height at a much lower rate until termination. Therefore, we hypothesize that termination is caused by the applied force combined with the density decay of the CNTs known to occur in the CNT forest growth process [27].

Finally, if enough force is applied (Regime III), the force appears to be of sufficient magnitude to oppose the self-organization of the CNTs and the CNTs within the forest do not show vertical alignment. Consequently, the height versus time curves increase very slowly, and the resulting rate shows a maximum at the beginning that steadily declines.

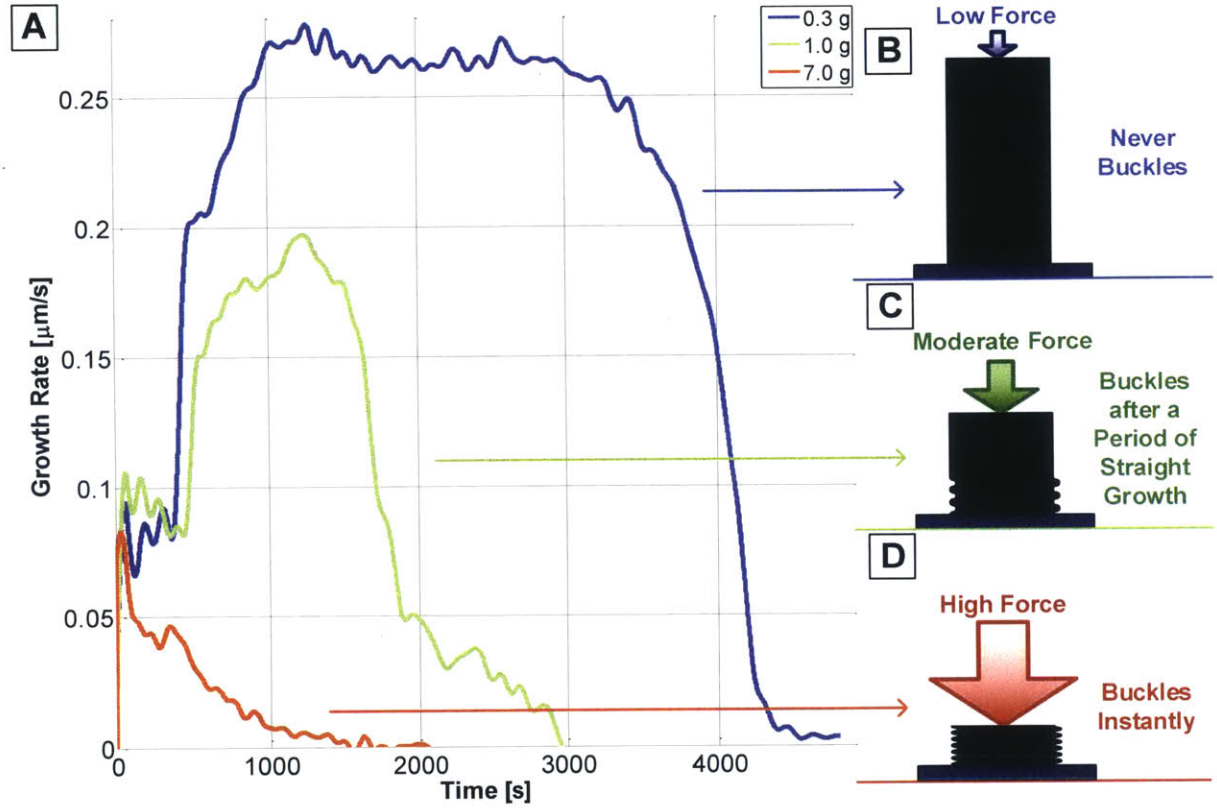

Figure 4.11 (A) Kinetics plots for representative samples of three growth regimes occurring under low, moderate, and high static compressive loads, depicted in schematics (B-D, respectively).

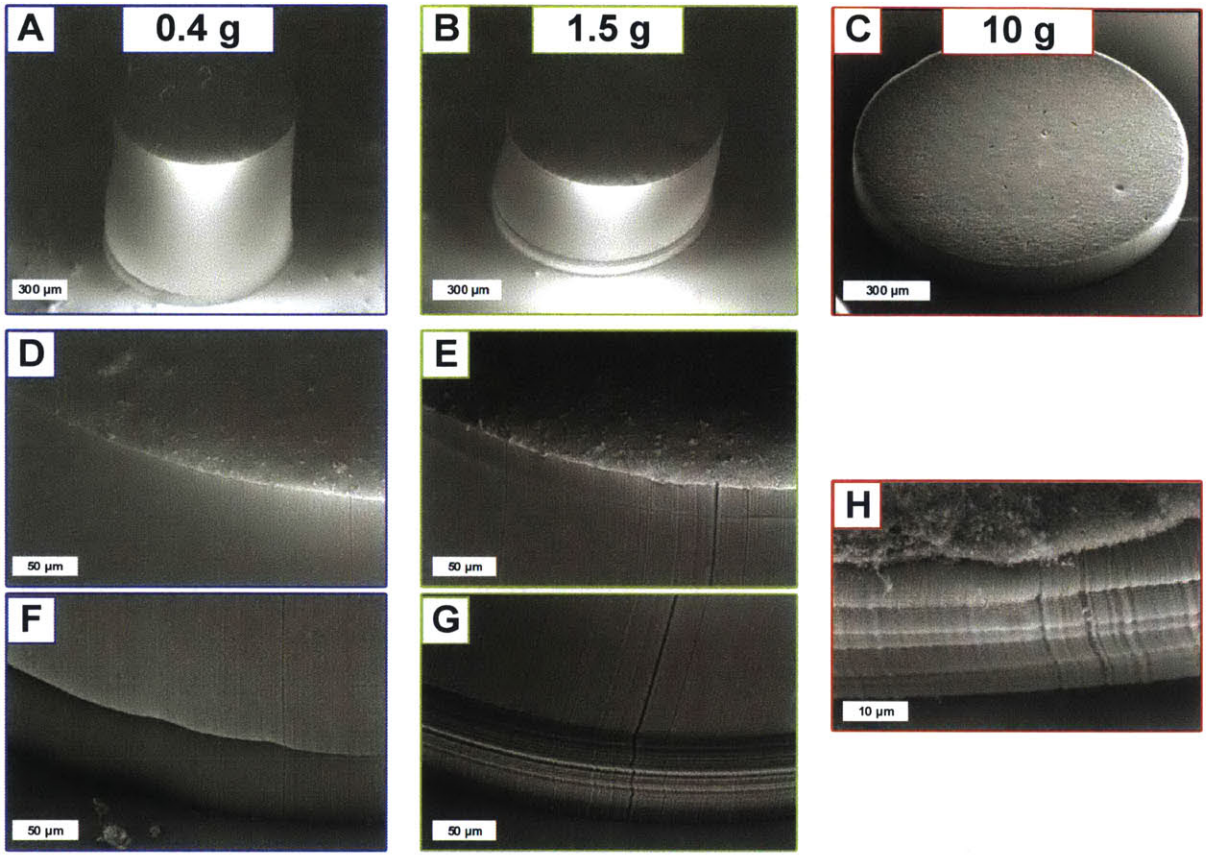

Figure 4.12 SEM images of representative samples of each of the three growth regimes, showing the whole pillar (A-C), the top of the pillar side-wall (D,E), the bottom of the pillar side-wall (F-G), and the whole pillar side-wall (H).

The time and height of the forest at which buckling first occurs, determined by the sharp change in the height vs. time curve, for each growth is plotted in **Figure 4.13**, for Regime II and Regime III. Generally, there is a decrease in time and height to buckle with increasing force. However, there is a sharp transition from Regime II to Regime III between applied force of 4 g and 5.1 g (50.0 kN/m^2 and 63.7 kN/m^2). It appears that pressures above 50 kN/m^2 will induce immediate collapse of the forest so that the pillar only grows with a deformed geometry. The pressures required to cause buckling (8.7 kPa) or complete collapse of the forest (50 kPa) are nearly an order of magnitude lower than the amount needed to buckle an already-grown forest by compression, measured at values ranging between 0.2 and 4.3 MPa [66], [75]. Therefore, such external forces during growth should be avoided if a forest devoid of buckles is desired.

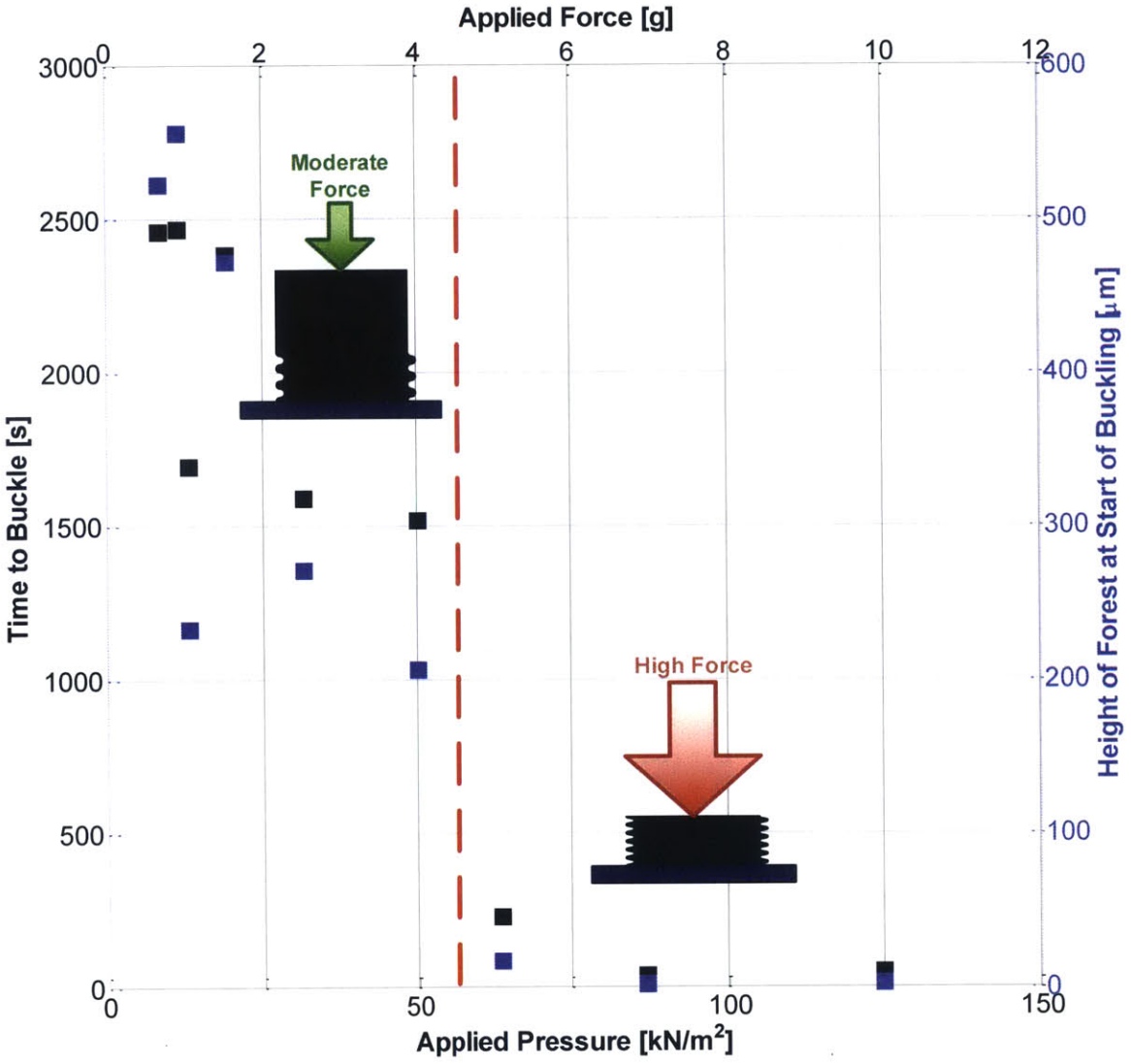

Figure 4.13 Plot of the time it takes for buckling to start (black) and the height at which buckling starts (blue) for CNT pillars grown under moderate and high static compressive loads.

The microstructure of the CNT forest is drastically affected by the applied forces. SEM images of higher magnification of the top, middle, and base of the pillars are shown in **Figure 4.14**. The individual CNTs remain relatively straight and aligned throughout the height of the pillar for forests grown under low forces. For moderate forces, there is a large difference in the tortuosity of the CNTs between the areas higher in the forest and those that constitute the buckling. However, the CNTs are much more misaligned and tortuous in forests grown under high loads, especially in the middle of the forest.

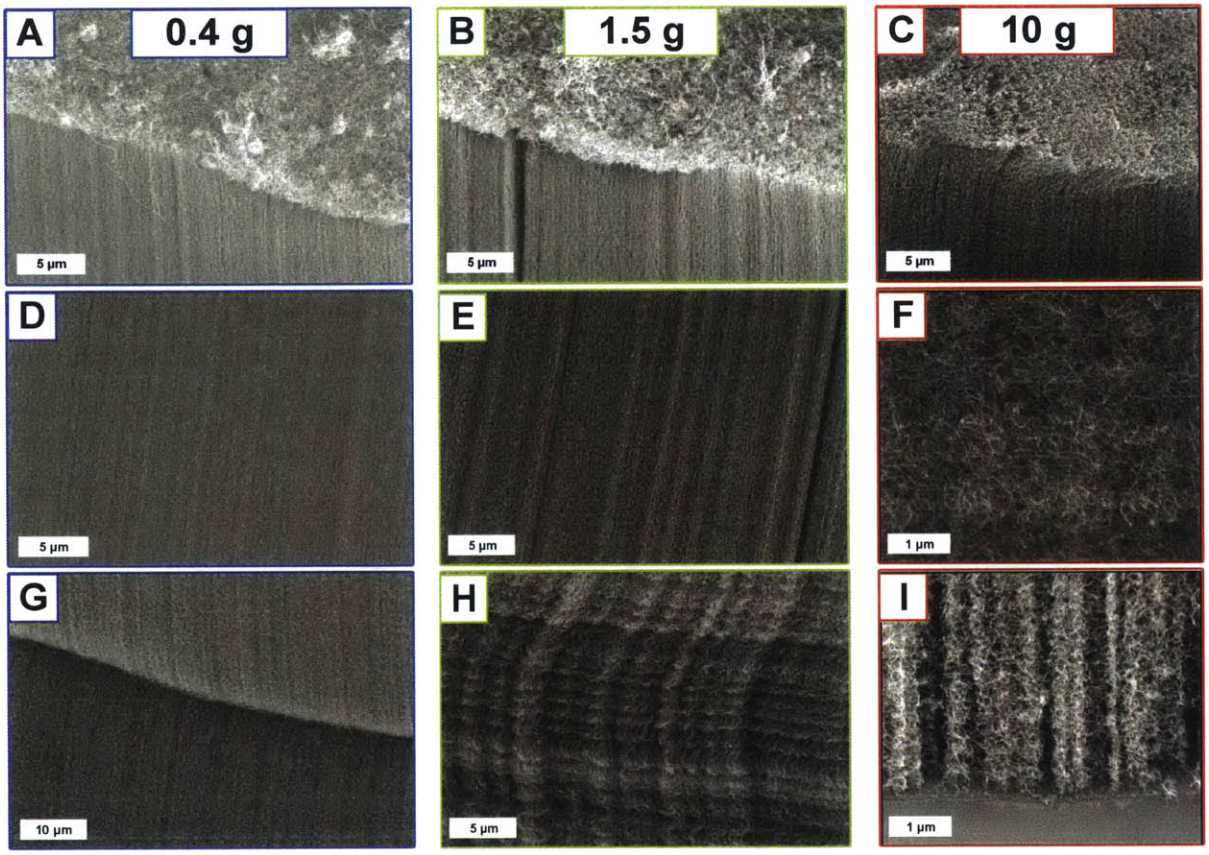

Figure 4.14 More detailed SEM images of the representative samples from the three growth regimes, showing the top (A-C), middle (D-F), and bottom (G-I) of the pillar side-wall.

The degree of misalignment is quantitatively described by the Herman's orientation parameter, which ranges from 1 for perfect vertical alignment, 0 for completely random orientation, and -0.5 for alignment in the horizontal direction. Previous studies of CNT forests grown conventionally under similar CVD conditions found that the orientation parameter ranges from 0.2 at the top of the forest, to up to 0.5 in the middle of the forest, and then as low as 0.1 at the forest base [76]. This Herman's data for the middle of the forest was collected by Mostafa Bedewy and colleagues by placing the CNT forests in the beamline of a synchrotron X-ray source and mapping the scattered X-rays, as shown in **Figure 4.15** for nominal samples of each Regime. Integration of the intensity of the X-ray map allows one to obtain the Herman's parameter. The CNTs of forests grown under 0.4 g, 1.5 g, and 4 g show less vertical alignment with increasing force. However, they still exhibit preferred orientation in the vertical direction (the direction of growth). This is in stark contrast to the forest grown under 10 g, which is actually more horizontally oriented

than vertically as indicated by its negative Herman's value; the CNTs have become so entangled that the characteristic vertical alignment of the CNT forest is lost.

The effects of static compressive forces during CNT forest growth on the growth kinetics and the resulting forest morphological characteristics have been investigated. It has been found that forces as small as 0.1 g (1.2 kN/m^2) affect growth, while forces of 0.7 g (8.7 kN/m^2) may cause deformation of the CNT structure during growth. Even large applied forces, of 50 kN/m^2 or greater, will result in the complete collapse of the CNT structure immediately after the forest lifts off the substrate. The individual CNTs become more tortuous and misaligned as force increases. Applied force also limits the achievable height and growth rate of the forests. Further characterization of the forests to obtain a number density at the base might reveal a general critical force per CNT that if exceeded would cause termination of growth of an individual CNT.

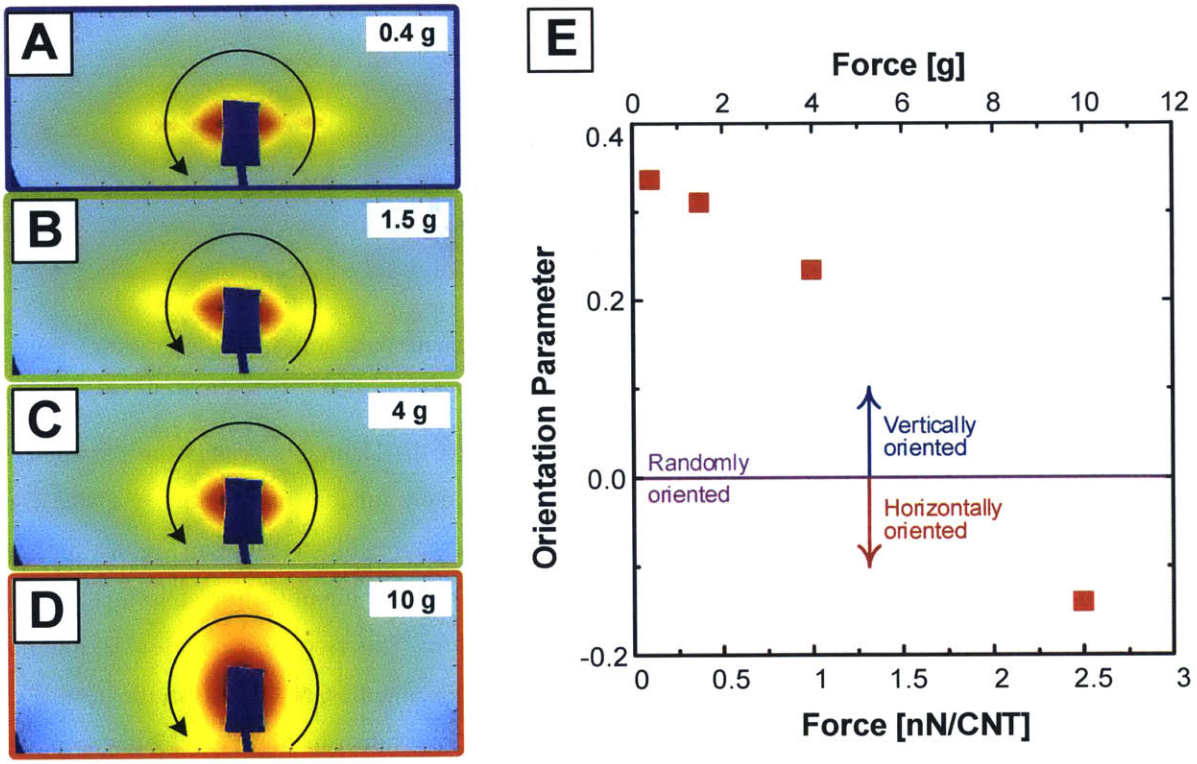

Figure 4.15 (A-D) Maps of scattered x-rays from CNT pillars representing each regime placed in the beamline of a synchrotron x-ray source. (E) Plot of the corresponding orientation parameters.

4.4 CNT Growth under Time-varying Forces

Now that an understanding of the effects of static force on CNT growth has been established, the effects of time-varying forces can be investigated. These dynamic growth experiments were conducted in a different lab setting and at a later time than the static force experiments, so the limiting values of applied force inducing a change in the growth behavior cannot be compared to those of the preceding section (for example, no forests detailed in this section grew taller than 500 μm), but the relative trends amongst growths within the set hold. The samples used in the dynamic force experiments were of the same Al_2O_3/Fe catalyst design and 1mm diameter circle pattern as used in the static force growth experiments. Three methods of applying time-varying forces were used: stopping the probe at a fixed position after a certain growth height is reached; administering a sudden change to the amount of force applied; and using cyclic forces. Above all, the previous experiments show that the response of the forest to force may be different depending on the forest morphology and density. For example, it was found above that force can influence the rate of CNT self-organization. Therefore, experiments varying the force with time at certain stages of the growth process (e.g. after self-organization has occurred) can further our understanding of the dynamics of CNT growth in response to force.

4.4.1 Hard Stop Tests

The first instance of CNT growth under time-varied forces studied concerns initially growing at a steady force until self-organization was assumed to be complete, then holding the probe at a fixed position after a certain duration of CNT growth. This experiment is an attempt to discover the maximum load that a growing CNT forest will be able to exert on a rigid body, and to determine how an impediment to the vertical growth of the CNT forest affects its morphology. One experiment was conducted by first growing a CNT forest pillar under a load of 0.1 g to a height of 150 μm to allow for the forest structure to fully develop. After the forest had grown 150 μm, the probe height was held fixed so that further growth resulted in the forest pushing against the probe. Rather than the load slowly increasing to some maximum value and maintaining that value as expected, the load peaks in periodic fashion as shown in **Figure 4.16**.

The assertion is that the peak corresponds to the maximum force that the forest exerts, and thus the maximum force the forest can withstand, before the load is too great for the CNTs to support and the forest buckles while growth continues. The rapid decrease in the load as shown in **Figure 4.17** corresponds to the forest buckling, and the measured height drops briefly in response. The probe then quickly returns to the set height of 150 μm, and further CNT growth slowly pushes the forest back against the probe until the load increases and the forest buckles again. The frequency of the peaks corresponds to how often the forest

buckles. As detailed in **Table 4.3**, the forest initially buckles once every 22.3 seconds on average, as further growth of the CNTs is required to return the forest to the set probe height and to subsequently reach the critical value needed to induce buckling. The period decreases over time as the time between load peaks decreases and the load peaks broaden until eventually, by minute 15 there is a constant increase and decrease in the load. At this point, termination of the forest growth is reached, and the peaks in measured is caused by an over-crowded area under the probe, which results in the probe being pushed slightly above its set value. The probe's feedback control responds by compressing the forest, which springs back in a repeating fashion. Releasing the probe from this constraint so that it maintained a constant load instead of a constant height did not result in the probe increasing in height, further proving that growth had terminated. The force needed to induce buckling can be determined from **Table 4.3** as the load amplitude plus the offset from the baseline initial value, or 3.1 +/- 0.4 g. This value might partially reflect the effect of the spring back of the forest after growth had terminated and thus be a measure of the forest stiffness rather than capacity to resist buckling, though the two are inherently related. **Figure 4.18** shows SEM images for this forest, highlighting the regions of frequent buckles near the base of the forest (E,F).

	Peak-to-peak Height [μm]	**Load Baseline [g]**	**Load Amplitude [g]**	**Load Peak Width [s]**	**Load Period [s]**
Minute 1	5.3	0.0	2.5	4.4	22.3
Minute 10	4.0	0.1	3.2	7.6	21.2
Minute 15	2.4	0.1	3.2	11.1	19.0
μ	3.9	0.1	3.0	7.7	20.8
σ	1.5	0.1	0.4	3.4	1.7

Table 4.3 Summary of characteristics of the height and load curves corresponding to Fig. 4.12, obtained by holding the force probe fixed after 150 μm of growth under 0.1 g of applied force. Values were averaged for the 2-4 peaks present during the selected minutes, with mean μ and standard deviation σ across the selected minutes. The peak-to-peak height is the total vertical displacement of the probe for a cycle, the load baseline is the average value of the load outside of the peaks, the load amplitude is the height of the load peak, the load peak width is the time during which the load spikes, and the load period is the time from one load peak to the next.

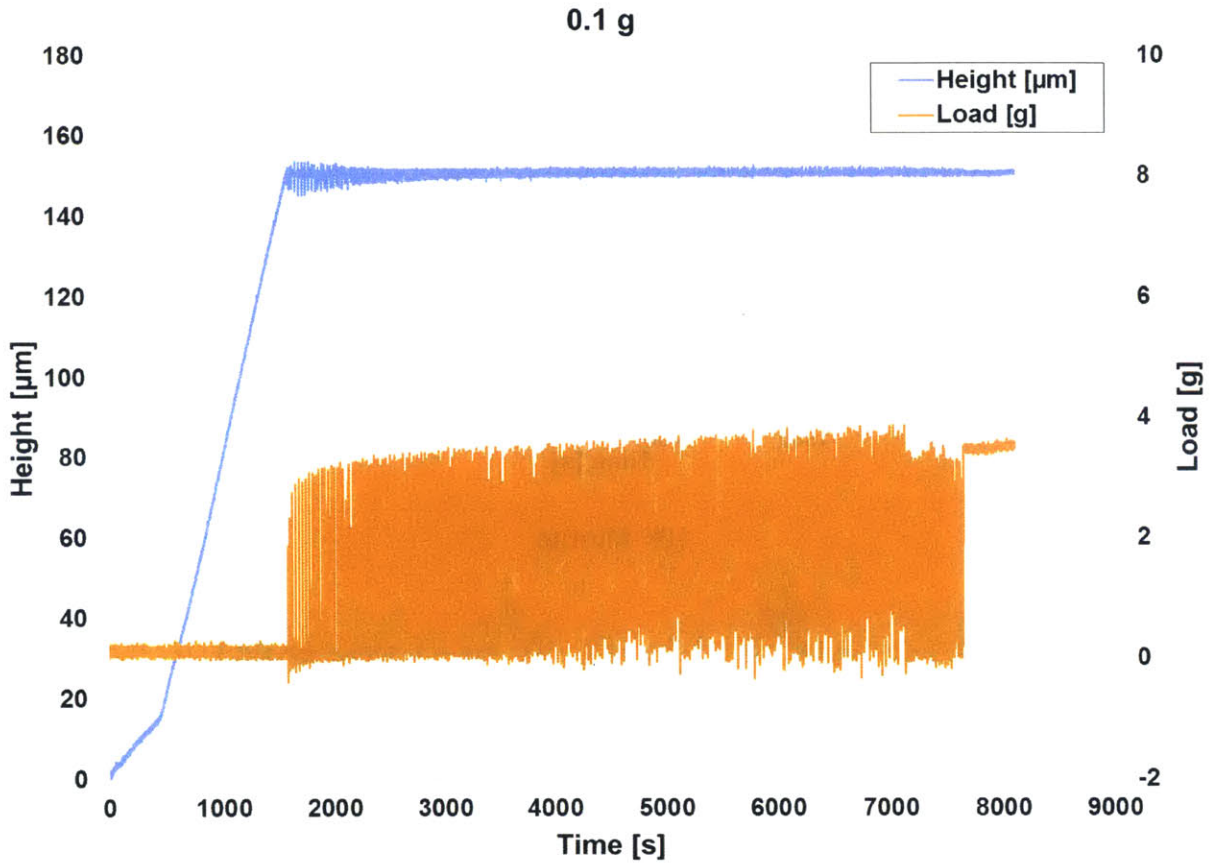

Figure 4.16 (A) Measured height and load for a pillar grown under 0.1 g compression for the first 150 µm of growth, after which the probe was commanded to maintain that height. Subsequent growth created large oscillations in the measured load as well as some dips in the height curve, as highlighted in **Figure 4.17**

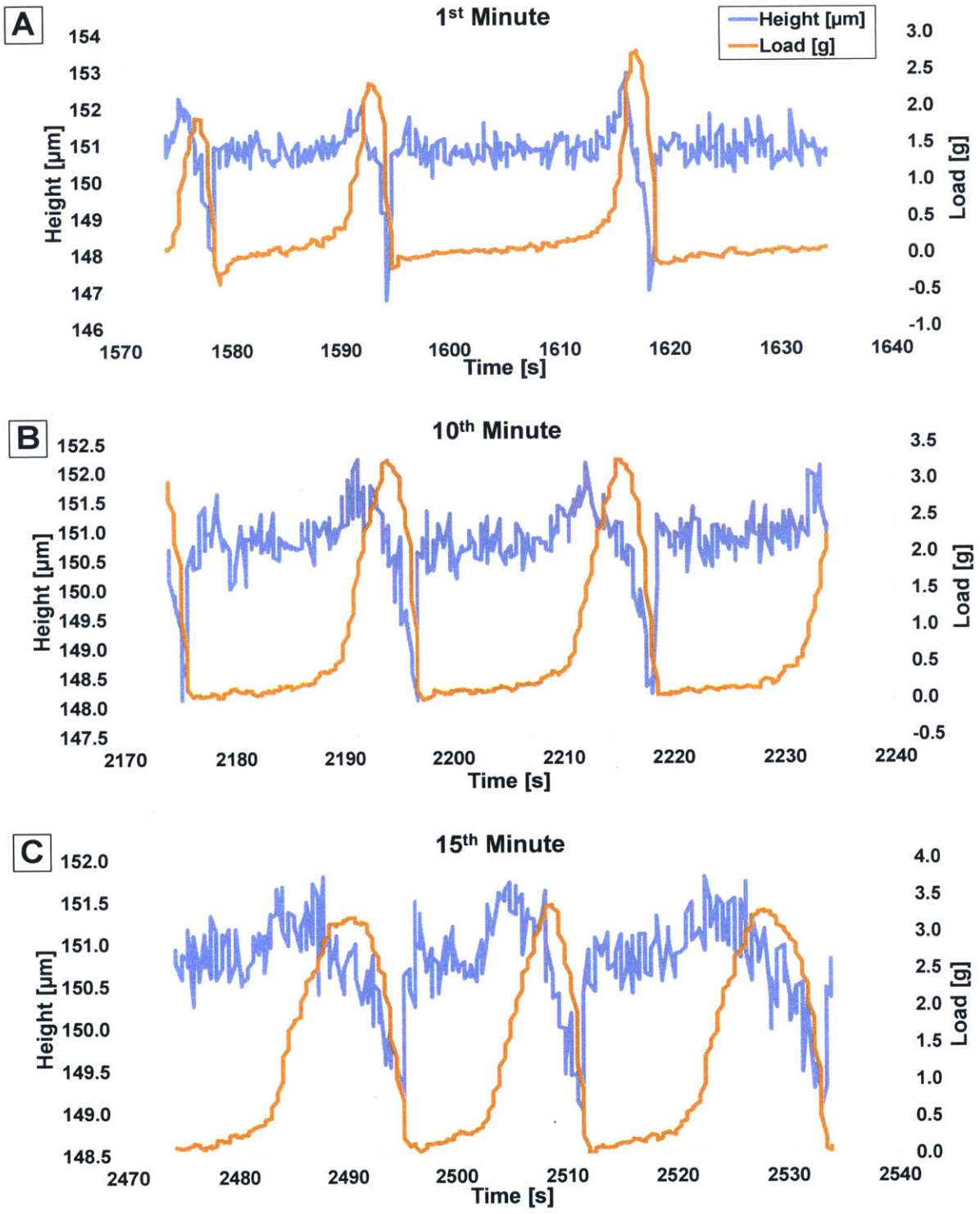

Figure 4.17 For the 0.1 g hard stop test, the (A) 1st, (B) 10th, and (C) 15th minutes after the forest reached a height of 150 µm.

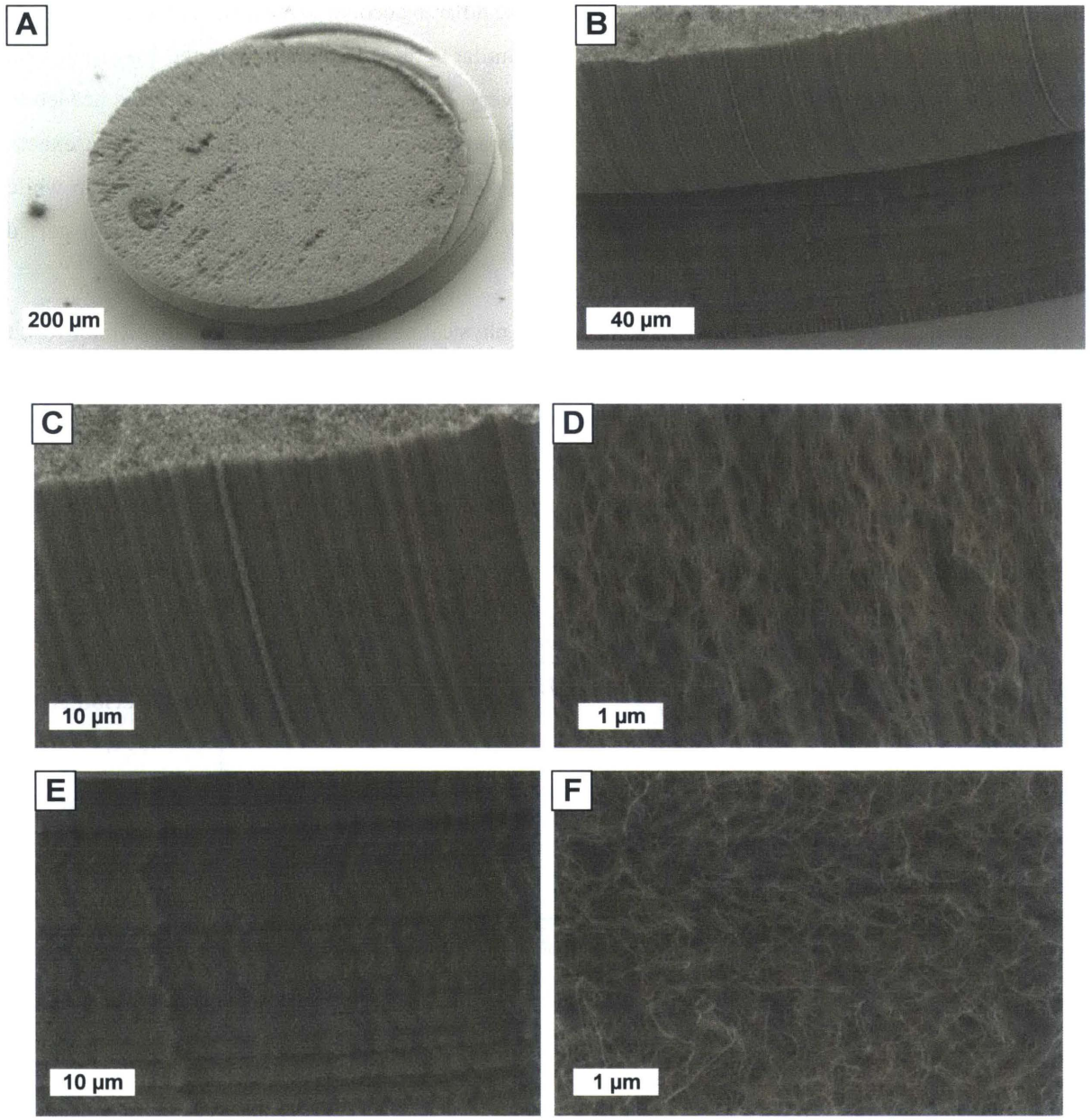

Figure 4.18 SEM images of (A) the whole pillar, (B) the whole side-wall, (C,D) the top of the side-wall, and (E,F) the base of the forest.

Figure 4.19 shows results from a similar experiment starting with growth under an applied load of 1 g rather than 0.1 g, with characteristic values for the selected minutes of the height and load curves detailed in **Table 4.4**. The load curve for this experiment exhibits an odd behavior of decreasing load amplitude with time (though with the same maximum load reached of around 3 g. A review of the SEM

images of **Figure 4.21** reveals a large crease (E) causing the pillar to become slanted, which would influence the force transmission between the probe and the base. Similar to the 0.1 g experiment, the 1 g experiment also finds the frequency of buckling to be around once every 20 seconds and the value of force needed to induce buckling at around 3 g (1 buckle per 18.4 +/- 2.9 seconds and 2.9 +/- 0.9 g respectively, to be exact). The load baseline is 0.9 g, caused by the initial growth conditions of having the probe hard stop while already applying a 1 g load. The load amplitude of 2.0 +/- 0.5 g is smaller than that of the growth started under 0.1 g applied force.

In summary, these hard stop tests showed that a physical obstacle to forest growth will not result in abrupt termination of the growth. Additionally, the CNT forest will buckle immediately upon reaching a critical load. For this given CNT catalyst system, geometry, and number density, a maximum load of around 3 g (37.5 kN/m^2 pressure) was measured. These results also give an indication that buckling might be avoided if the external load can be relieved before a critical value of force or time is reached.

	Peak-to-peak Height [μm]	**Load Baseline [g]**	**Load Amplitude [g]**	**Load Peak Width [s]**	**Load Period [s]**
Minute 1	5.0	0.0	2.5	4.3	16.7
Minute 10	1.5	1.5	1.5	11.2	16.8
Minute 15	1.6	1.1	1.9	15.7	21.8
μ	2.7	0.9	2.0	10.4	18.4
σ	2.0	0.8	0.5	5.7	2.9

Table 4.4 Summary of characteristics of the height and load curves corresponding to Fig. 4.14, obtained by holding the force probe fixed after 150 μm of growth under 1 g of applied force. Values were averaged for the 2-4 peaks present during the selected minutes, with mean μ and standard deviation σ across the selected minutes. The peak-to-peak height is the total vertical displacement of the probe for a cycle, the load baseline is the average value of the load outside of the peaks, the load amplitude is the height of the load peak, the load peak width is the time during which the load spikes, and the load period is the time from one load peak to the next.

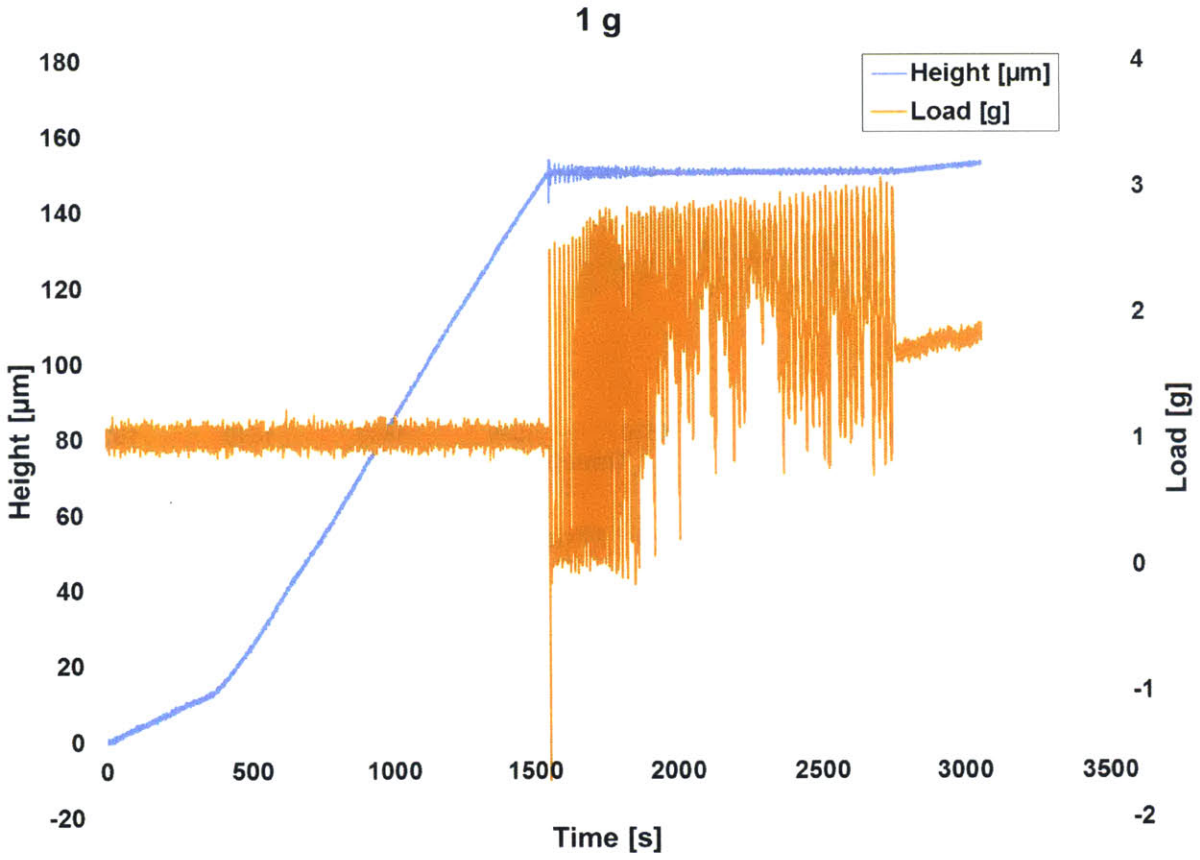

Figure 4.19 (A) Measured height and load for a pillar grown under 1 g compression for the first 150 µm of growth, after which the probe was commanded to maintain that height. Subsequent growth created large oscillations in the measured load as well as some dips in the height curve, as highlighted in **Figure 4.20**.

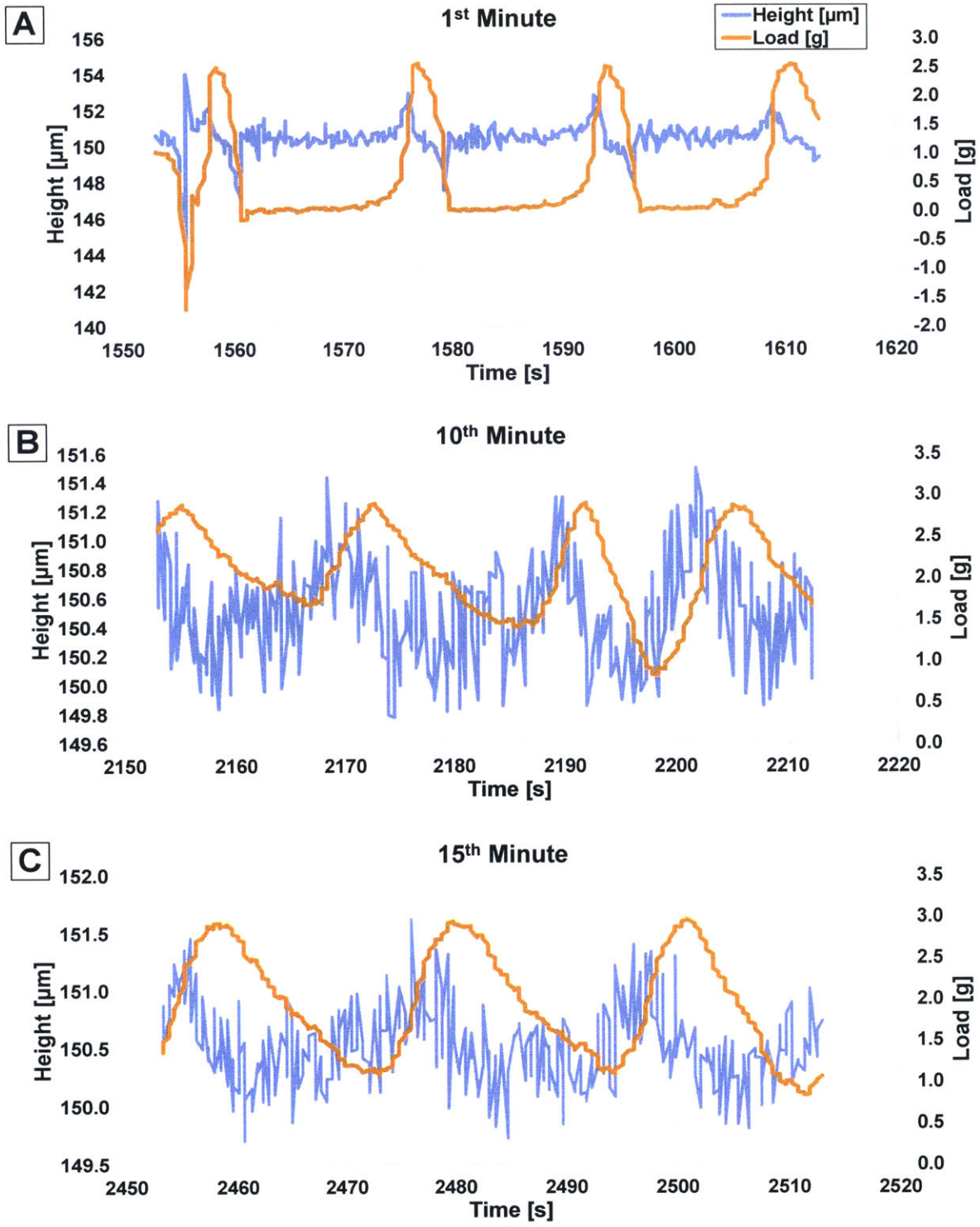

Figure 4.20 For the 1 g hard stop test, the (A) 1st, (B) 10th, and (C) 15th minutes after the forest reached a height of 150 µm.

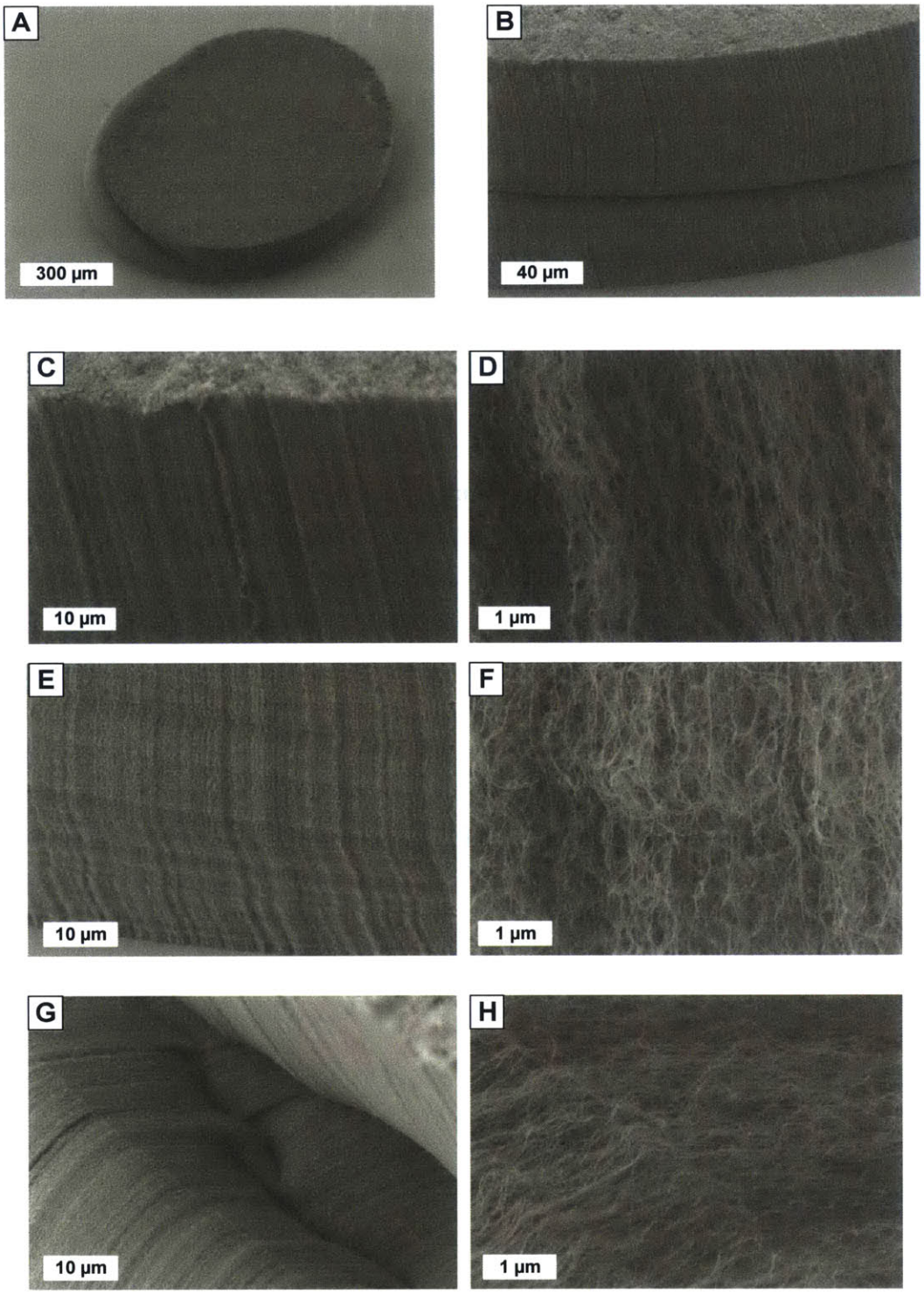

Figure 4.21 SEM images of (A) the whole pillar, (B) the whole side-wall, (C,D) the top of the side-wall, (E,F) the base of the forest, and (G,H) a crease in the forest.

4.4.2 Force Jump Experiments

Another simple case to investigate CNT forest growth under time-varying loads is to allow the forest to grow unhindered with the probe waiting above the substrate, and to see how the forest responds to applied force after contact with the probe. In a test case, the probe was moved to 150 um above the substrate, a height determined to be enough to allow for proper self-organization of the CNT forest and growth to develop and to be comparable to the hard stop tests. The probe was kept there and upon contact the probe was commanded to exert a force not to exceed 1.0 g; therefore, the probe remained at a constant position as the CNT forest increased the force exerted and then began moving upward.

Figure 4.22 shows the time-dependent load, height, and growth rate throughout the experiment. The starting height is measured from where the probe waits initially for the CNT forest to grow into it, so the terminal height is approximately 275 μm rather than 125 μm as shown in the plot. Assuming a constant growth rate for the first 150 μm of growth since the rate was not measured, the initial growth rate until probe contact 0.13 μm/s. The average rate from after the load change to termination is 0.049 μm/s, a significant decrease. The numbers on the kinetics plot indicate important features in the kinetics. Point 1 indicates right before the forest grows into and begins pushing the probe upwards. The second point is when buckling of the forest first occurs, and point 3 is a time close to termination of growth. The SEM images on the right of the figure show how the features in the kinetics translate into features in the forest microstructure. The initial stage of growth, corresponding to the top section of the forest side-wall (**Figure 4.23C,D**) results in fairly straight and vertically-aligned CNTs, as there is no external load limiting their self-organization and upward motion. However, the forest responds immediately to the application of force with the development of a crease in the forest (near point 1) and an increase in the tortuosity of CNTs. This is seen after the forest has buckled near point 2 as in **Figure 4.23E,F**, and especially near the base of the forest as in **Figure 4.23G,H**, where CNT density is lower and there are fewer CNTs supporting the load.

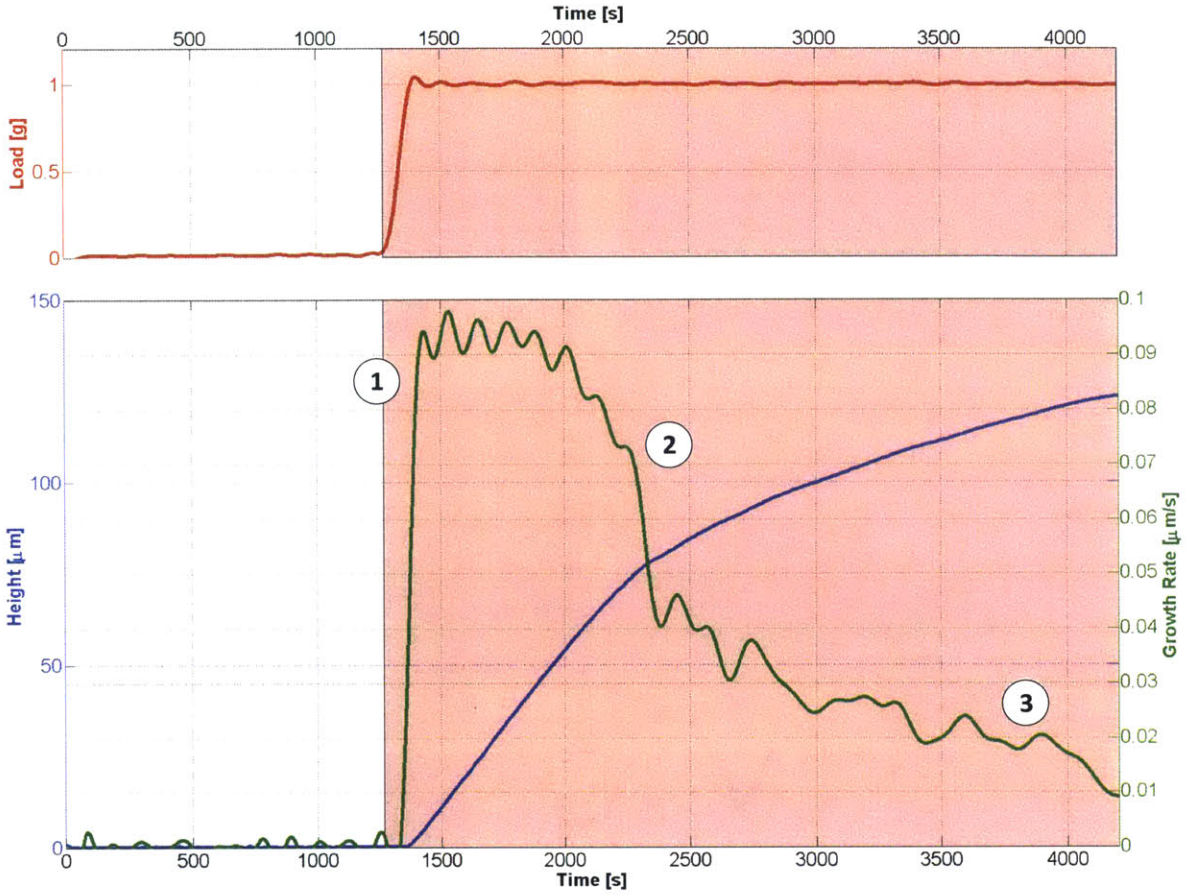

Figure 4.22 Height and growth rate curves for sudden increase in load from zero during growth.

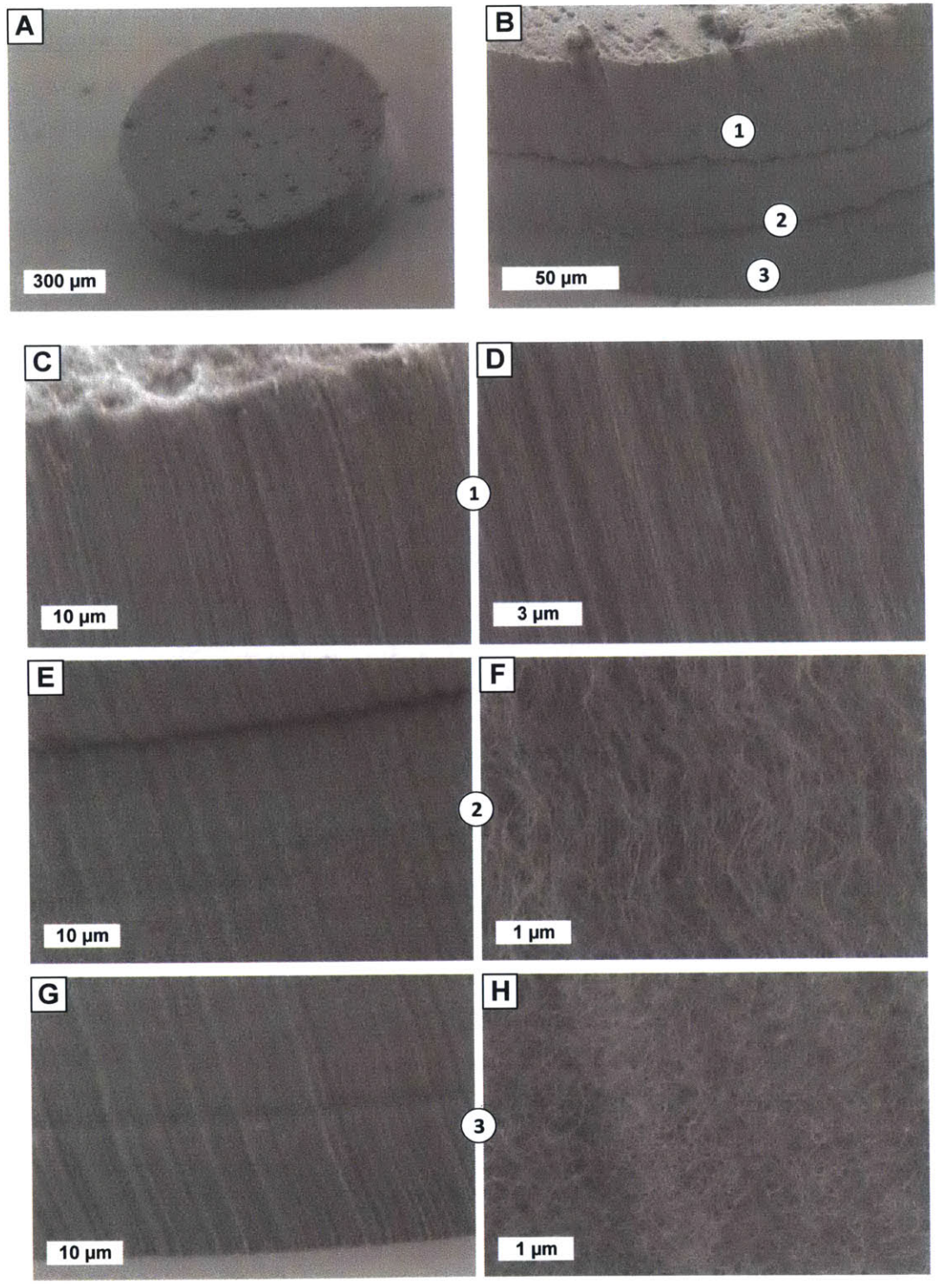

Figure 4.23 SEM images of the forest from **Figure 4.22**: (A) the whole pillar, (B) the whole side-wall, and the side-wall (C,D) top, (E,F) middle, and (G,H) base. Features of the kinetics curves indicated by numbers are highlighted in the microstructure.

Two experiments were performed in which there was an initial period of growth under low force (0.1 g), and then a sudden change to higher force (1 g) after the forest had grown 150 μm. The goal of these experiments was to observe if a rapid increase in load would cause irrecoverable deformation and premature termination of the forest, and to measure the response in growth rate. The height and kinetics curves are shown in **Figure 4.24** and **Figure 4.26**, and SEM images of the pillar structures are shown in **Figure 4.25** **Figure 4.27**. In both cases, there is a brief halt in the height increase and a sharp dip in the rate curve as load is increased (point 2). However, the rate almost immediately recovers to an amount slightly lower than what it was at prior to the load change. This demonstrates the ability of a growing CNT forest to withstand sudden loads and to continue growth. Both of the forests display a crease in the side-wall, caused by the load change and indicated by point 2. These pillars also both display an increase in waviness and misalignment of individual CNTs from the top to the bottom of the pillar, as the effect of CNT density decrease in the later stages of growth is compounded with the increase in force.

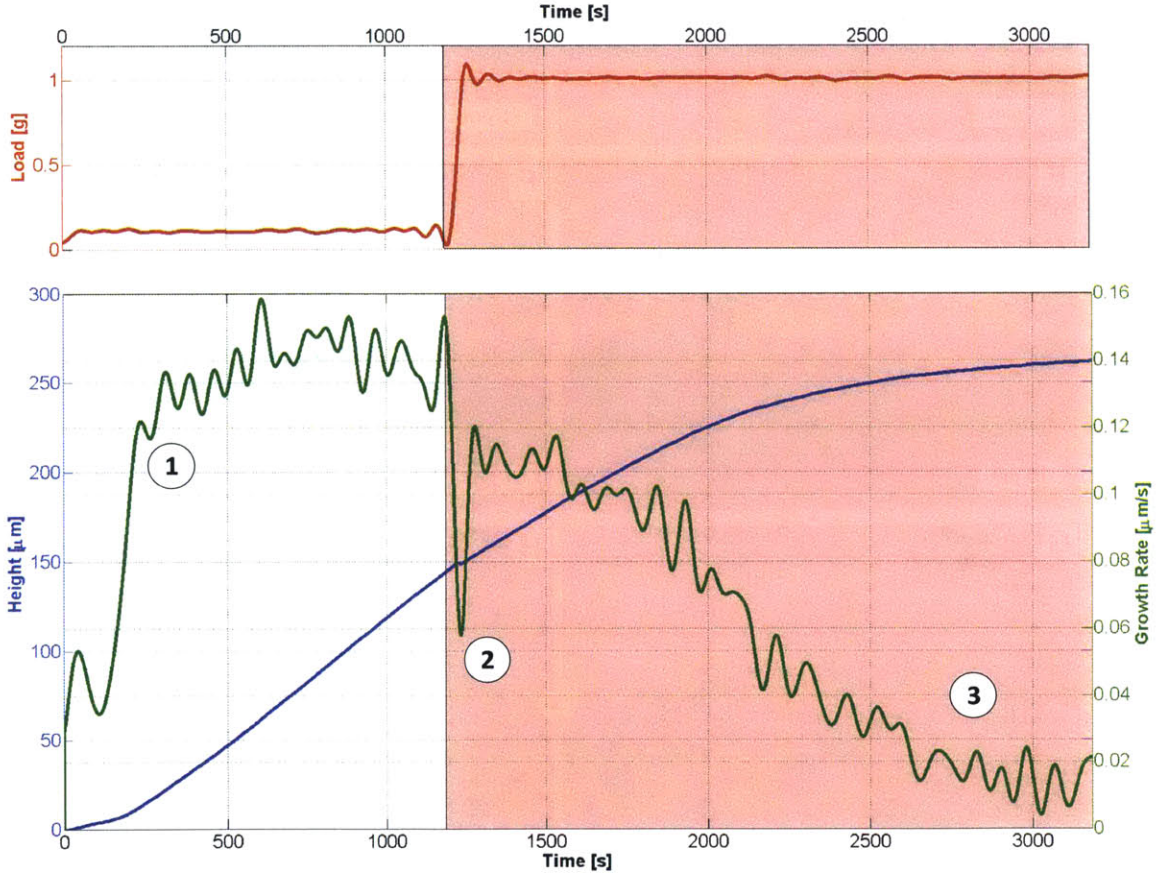

Figure 4.24 Height and growth rate curves for sudden increase in load during growth

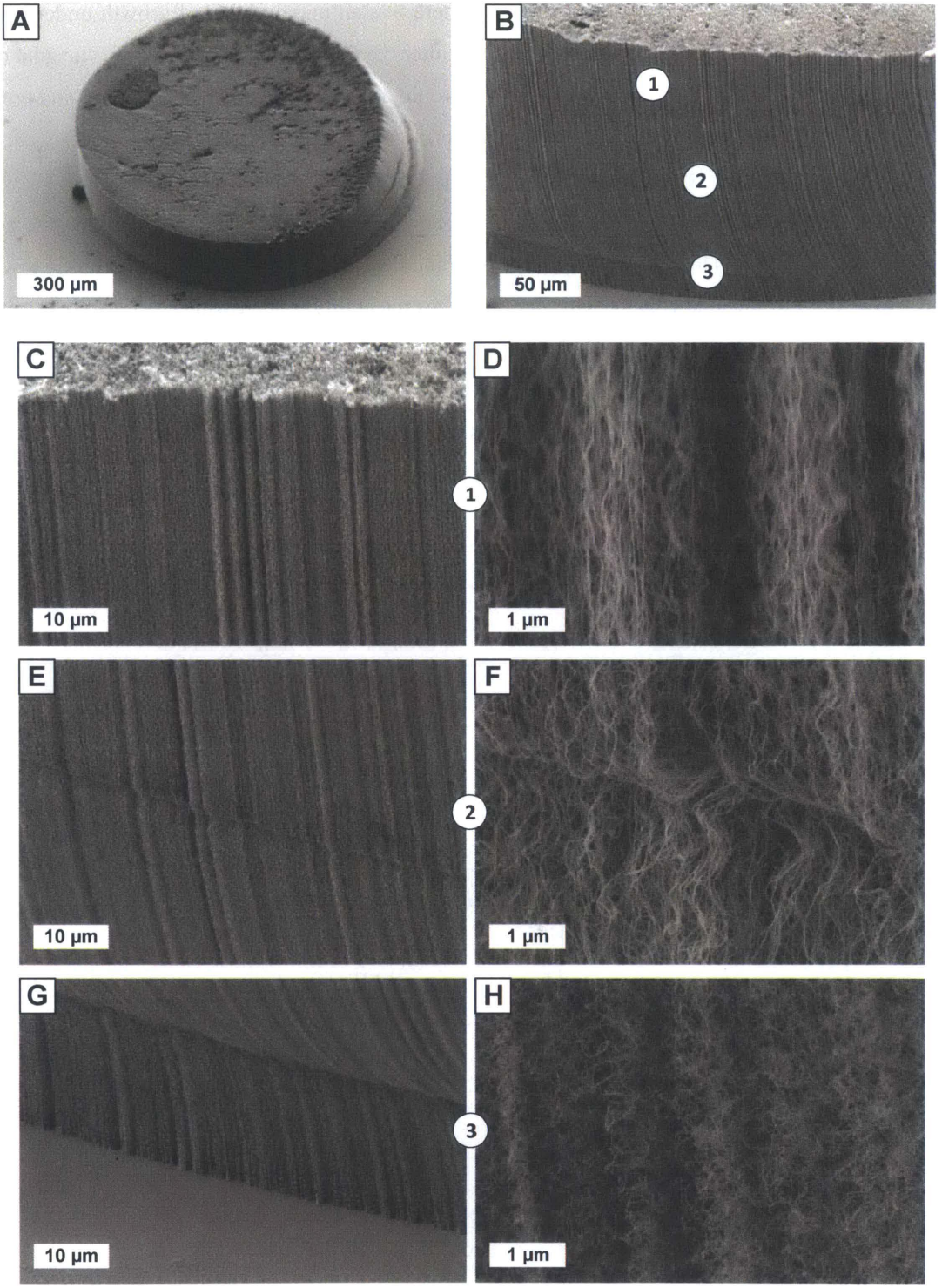

Figure 4.25 SEM images of the forest from **Figure 4.24**: (A) the whole pillar, (B) the whole side-wall, and the side-wall (C,D) top, (E,F) middle, (G,H) and base. Features of the kinetics curves indicated by numbers are highlighted in the microstructure.

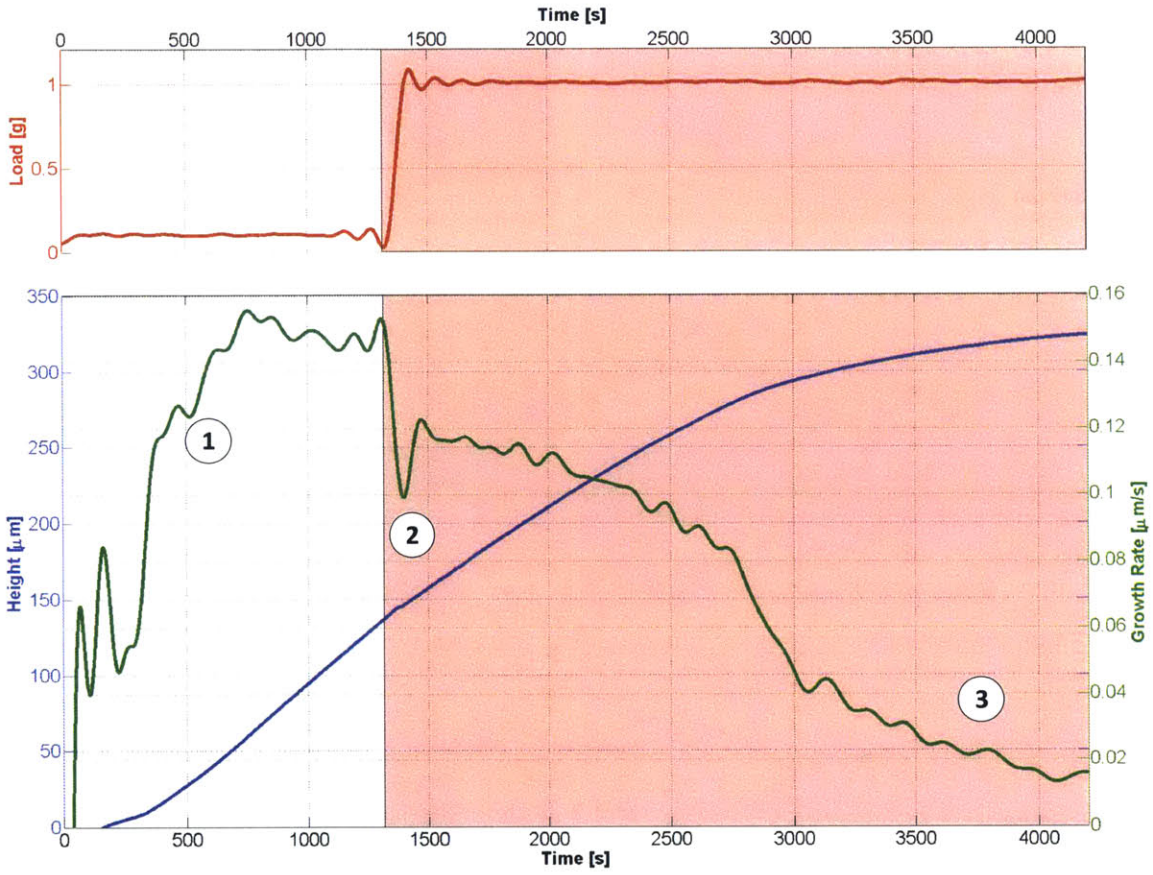

Figure 4.26 Height and growth rate curves for another experiment of sudden load increase during growth

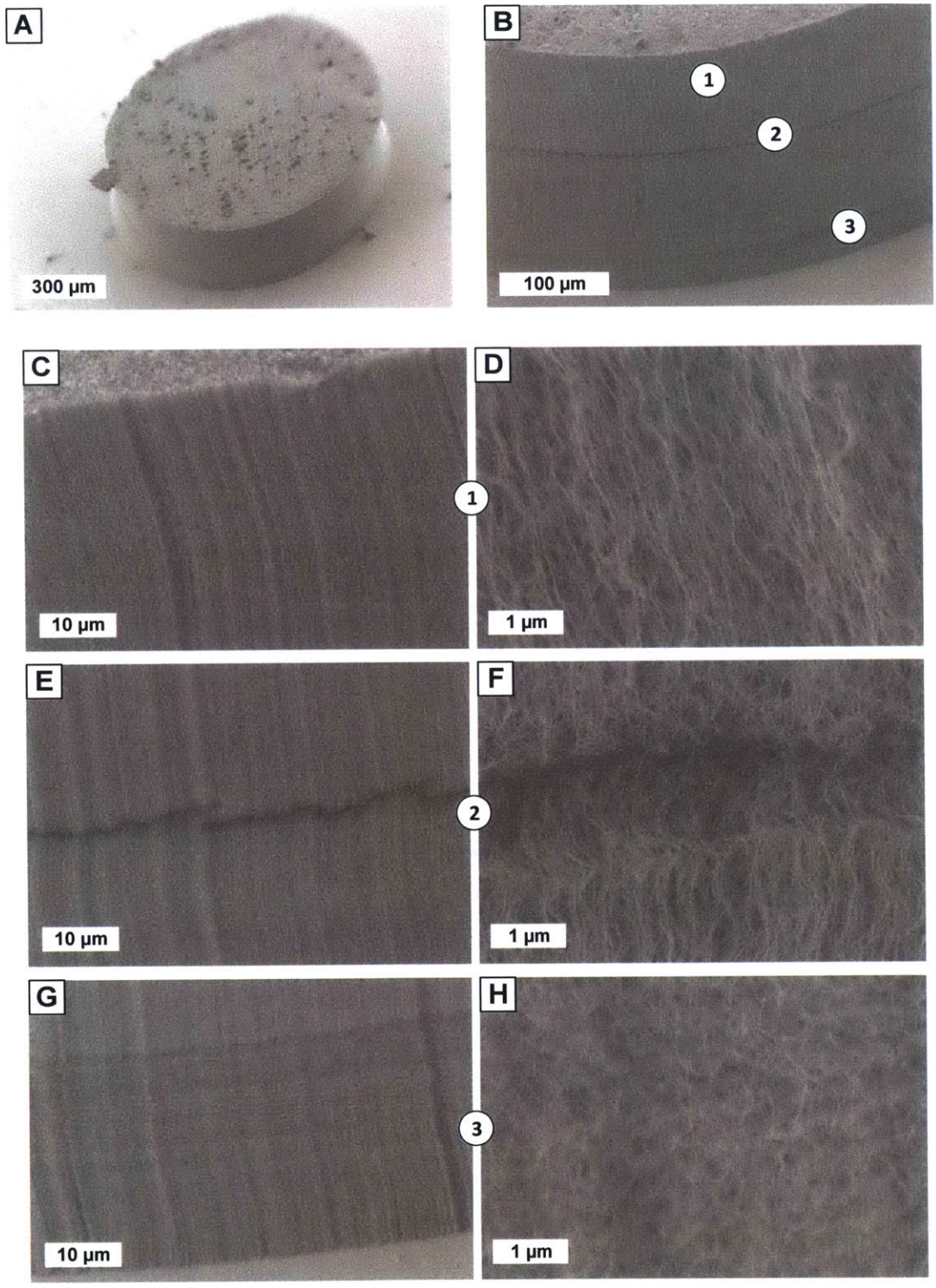

Figure 4.27 SEM images of the forest from **Figure 4.26**: (A) the whole pillar, (B) the whole side-wall, and the side-wall (C,D) top, (E,F) middle, (G,H) and base. Features of the kinetics curves indicated by numbers are highlighted in the microstructure.

Figure 4.28 shows what happens if the load is decreased instead of increased during a growth. For this experiment, the load is decreased from 1 g to 0.1 g after the forest had grown 150 μm. The forest grew at a rate near 0.14 μm/s at the time of the load change, comparable to the corresponding rates of the previously discussed dynamic experiments (grown at lower forces to start). However, in contrast to the increasing load growths, decreasing the load from 1 g to 0.1 g resulted in the full recovery of the growth rate at point 2. Subsequent growth is with a slowly declining rate until rapid termination (point 3). This behavior is characteristic of the static low force regime. However, inspection of the microstructure with SEM (**Figure 4.29**) reveals that at the top of the forest the CNTs are fairly tortuous, comparable to the bottom of the forests grown under increasing loads. The bottom of the forest grown under decreasing load does have some creases, and the CNTs show some degree of misalignment. However, there are no buckles of the forest throughout its height; the distinction between buckles and creases being that buckles are when all of the CNTs at that height bend to cause the overall forest to collapse, while a crease just has local deformation of the forest structure. This experiment is important because it showed that the forest will increase in growth rate when load is decreased.

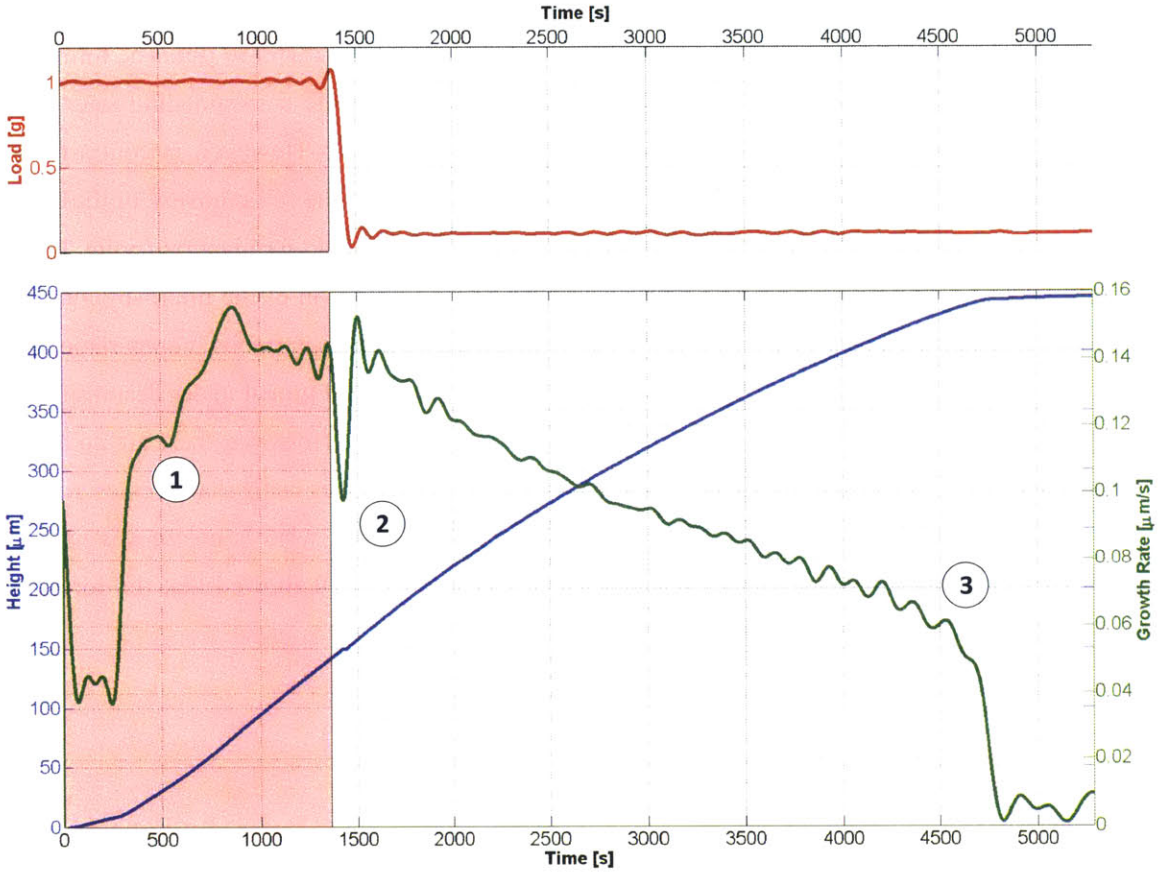

Figure 4.28 Height and growth rate curves for a sudden decrease in load during growth

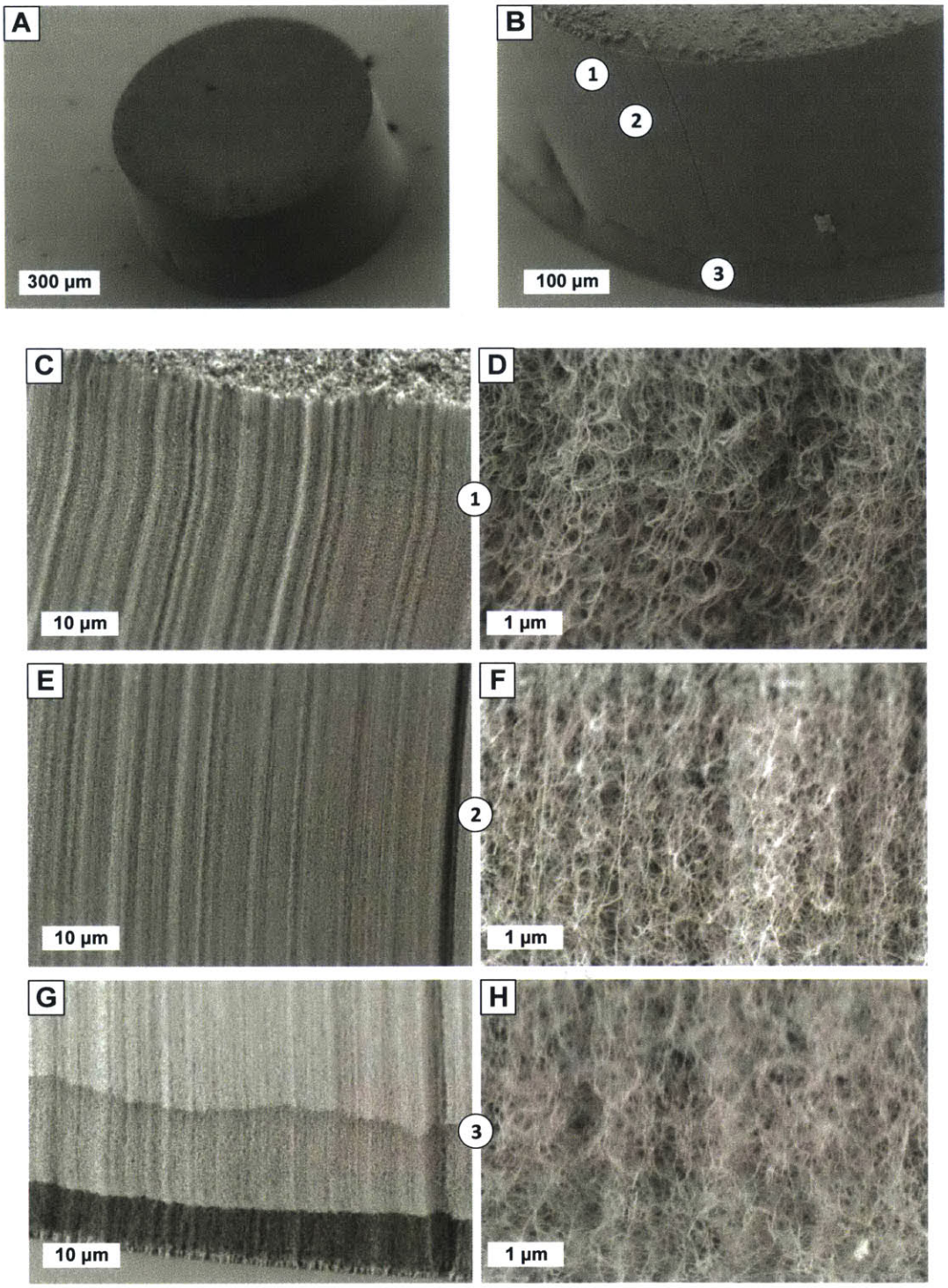

Figure 4.29 SEM images of the forest from **Figure 4.28**: (A) the whole pillar, (B) the whole side-wall, and the side-wall (C,D) top, (E,F) middle, (G,H) and base. Features of the kinetics curves indicated by numbers are highlighted in the microstructure.

Another experiment of decreasing the load from 1 g to 0.1g was performed (**Figure 4.30**), but with drastically different results as shown in **Figure 4.28**. In this case, the forest grew very slowly even to start (at no more than 0.065 μm/s), and the growth rate drastically declined before the forest had even grown 50 μm. Relieving most of the load seemed promising, as the growth rate rapidly increased to a peak rate, though this rate declined immediately and quickly to termination. This growth shows that the growth rate can be recoverable (and may even be exceeded) upon relief of external force, but the extent of the improvement is limited by the initial growth conditions. The SEM images (**Figure 4.31**) seem to indicate that the CNT density was low and misalignment was high to begin, with enhanced effects visible near the forest base. This experiment offers hope that deteriorating growth might be overcome, though it also serves as a warning that prolonged growth under a moderate load may be unrecoverable.

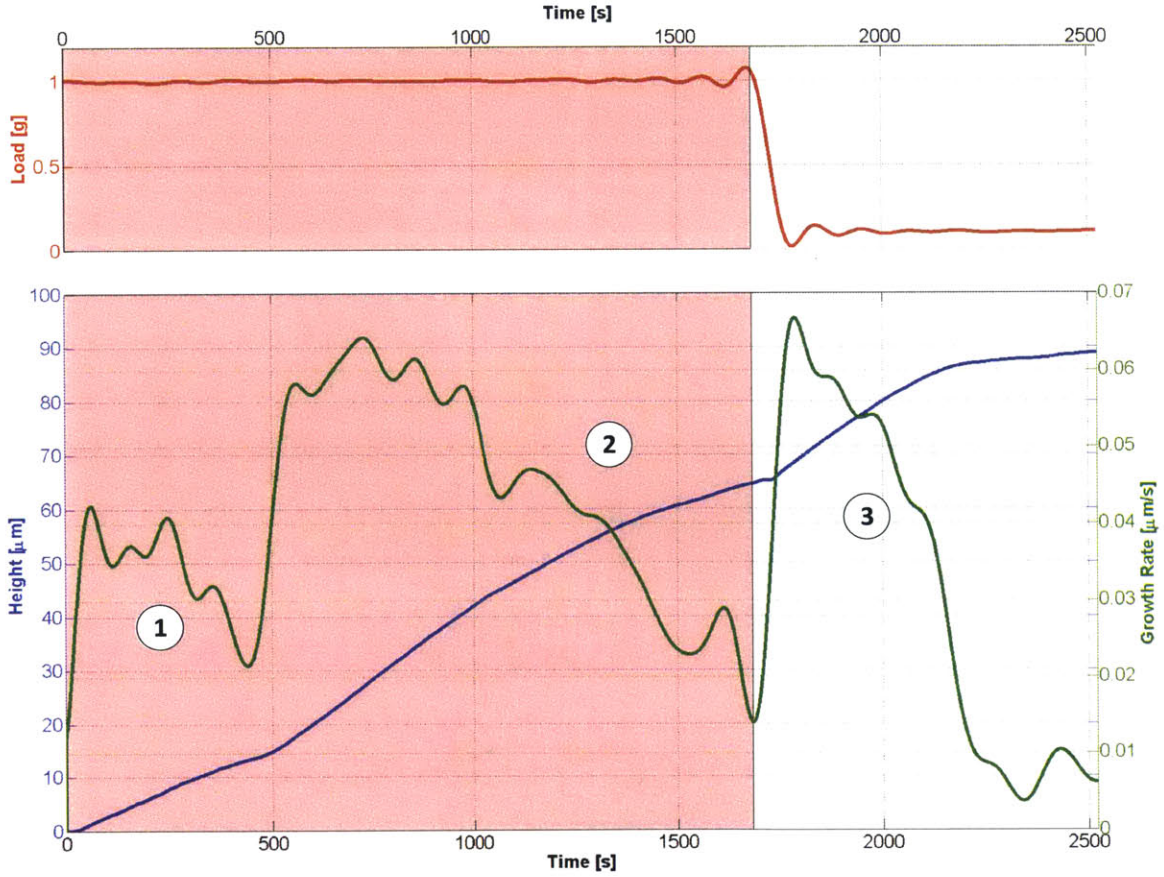

Figure 4.30 Height and growth rate curves for a sudden decrease in load after the pillar had already begun buckling during growth.

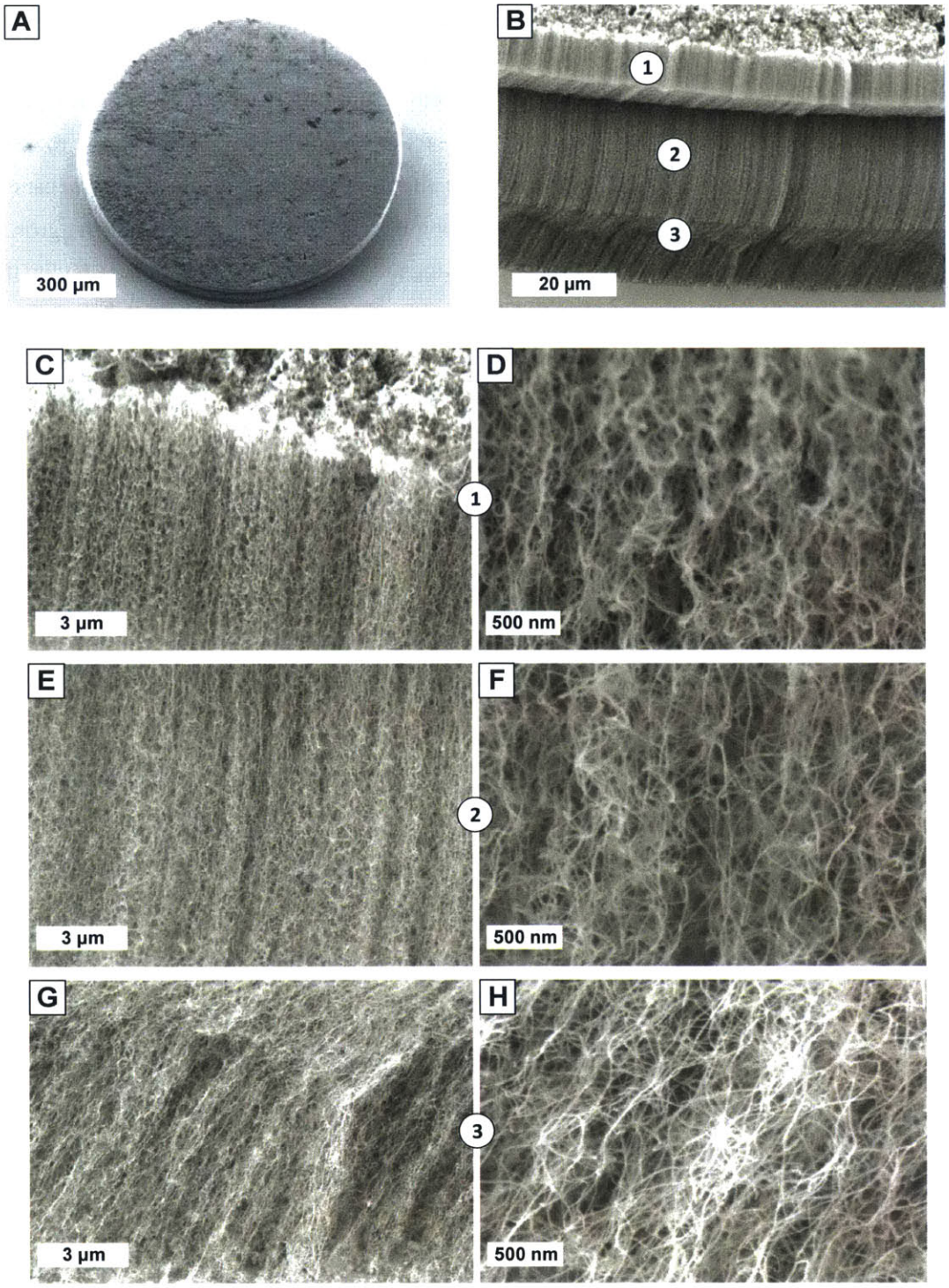

Figure 4.31 SEM images of the forest from **Figure 4.30**: (A) the whole pillar, (B) the whole side-wall, and the side-wall (C,D) top, (E,F) middle, (G,H) and base. Features of the kinetics curves indicated by numbers are highlighted in the microstructure.

A final investigation into the effect of decreasing the load during growth focused on a sudden switch from a high load of 5 g to low one of 0.1 g. This was to test the limiting case of whether normal forest growth can still be achieved after a load shown previously to prevent self-organization into a vertical morphology is applied. As indicated in **Figure 4.32**, the forest grew at a very low rate under the 5 g load. After 15 minutes of growth under the 5g load, when the pillar was not yet visible in the *in situ* camera, the load was suddenly decreased, resulting in a rapid response in the growth kinetics, and the growth rate increased rapidly. Even though the forest had been growing in a collapsed configuration, relieving the load allowed for subsequent growth to proceed with CNTs arranged more vertically aligned, thereby reducing the constrictions from mechanical coupling and allowing for the growth rate to be much higher. The divide between the initial, more tortuous section of CNT growth and the area of rapid growth after the load relief is visible in the SEM images in **Figure 4.33**.

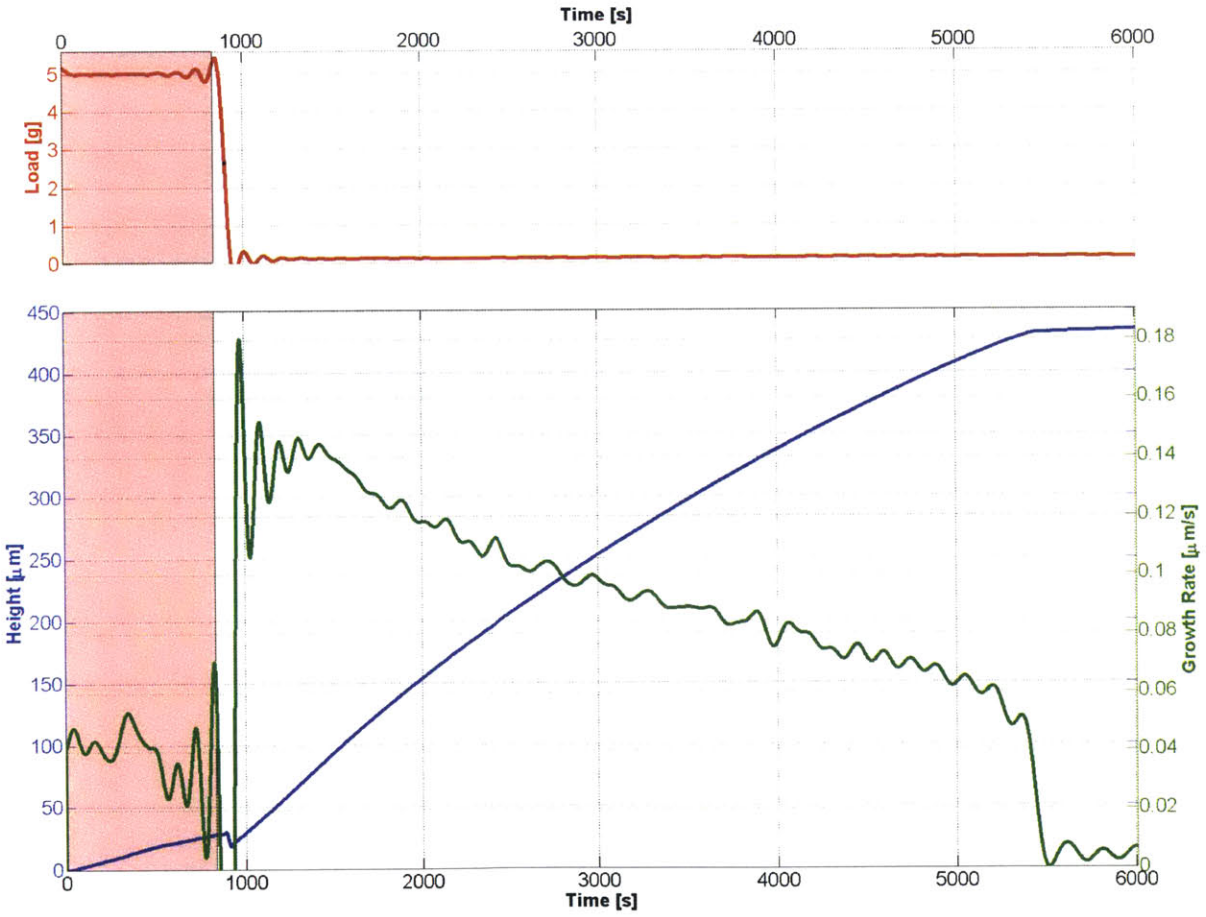

Figure 4.32 Height and growth rate curves for a large sudden decrease in load during growth.

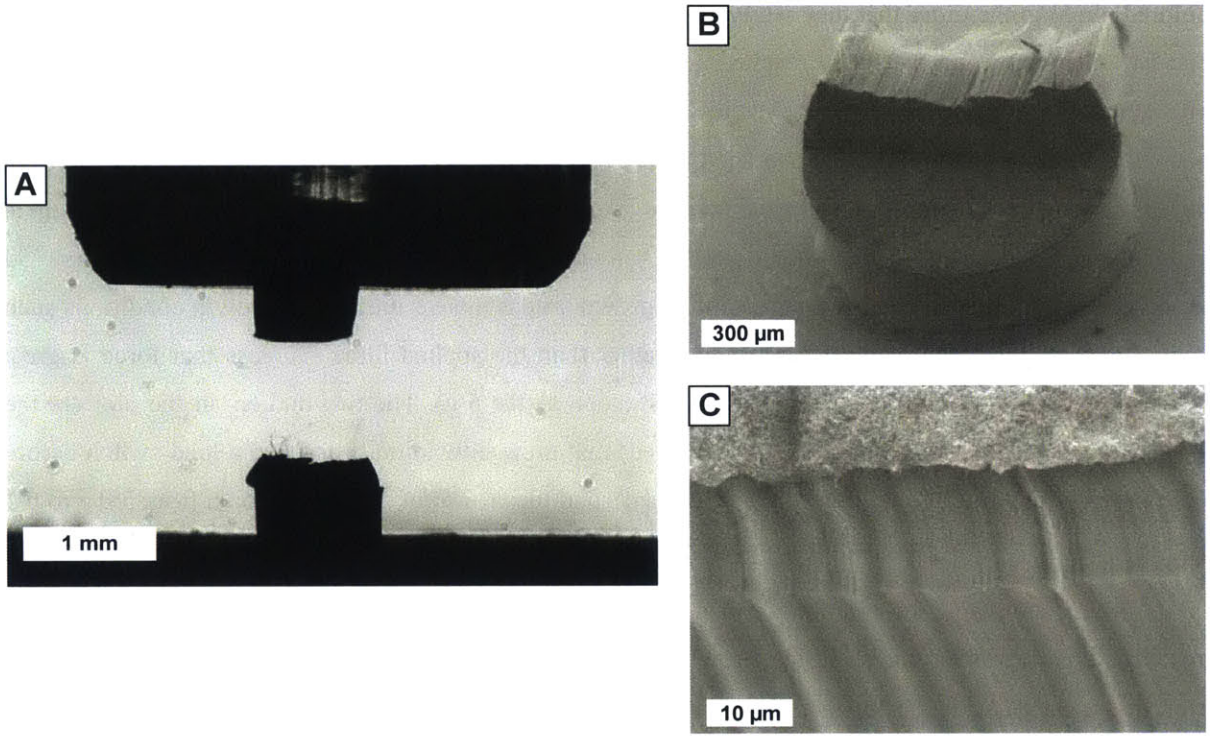

Figure 4.33 Images of the forest from **Figure 4.32**: (A) an optical image taken by the Mechanochamber camera after retraction of the probe, and SEM images of (B) the whole pillar and (C) the top of the side-wall.

One question this experiment proposes is whether the regions of the CNTs that grow in a collapsed state can be unwound to lengthen the forest and improve its properties after growth. This seems unlikely, based on the result of retracting the probe after the growth had finished and the system had cooled down to 35 °C. As seen in the *in situ* picture of the probe retraction in **Figure 4.33** and an SEM of the remaining pillar, a chunk of the forest remained adhered to the probe and pulled apart from the substrate and from the rest of the pillar upon probe retraction. This indicates that application of the 5 g load enhances the adhesive force between the forest and the probe as CNTs are forced to grow further into the roughness of the probe surface and increasing the van der Waals attractions between the forest and the probe. Although relieving the load allowed for a long period of rapid growth, the forest may have been growing under the collective power of just enough CNTs to withstand the low 0.1 g load.

The results of these experiments of a single sudden load change are summarized in **Figure 4.34**, along with two static force growths shown for reference. The average growth rate for before and after the load change is plotted with the height of the forest at the load change and the terminal height, respectively. The size of square points is proportional to the applied load. The legend lists the dynamic force growths

(colored plots) in the order that they were presented in this chapter. For most of the dynamic growths, the load was changed when the forest reached a height of 150 μm. The static growths, shown by the black arrows and gray points, frame these dynamic growths well. Since the static force growths did not have a load change, the growth rates were averaged before and after the forest reached a height of 150 μm. The plot of the growth of increasing load from zero to 1.0 g, represented in blue, starts at a height of 150 μm at an assumed average growth rate of 0.126 μm/s. Even under 1.0 g, the average growth rate for the first 150 μm is around 0.13 μm, indicating that this initial growth rate is more a function of growth conditions such as the moisture level and catalyst preparation, rather than the applied force – unless that force is great enough to cause immediate collapse of the forest (such as the 5 g). The two outliers in the plot are the growth of decreasing force from 1.0 g to 0.1 g (red) that grew slow initially and had a load switch before reaching 150 μm (which it ultimately never reached), and the growth of decreasing force from 5.0 g to 0.1 g (green) that was growing too slow to reach 150 μm before the load switch, but grew rapidly afterwards.

The first notable information gleaned from the plot is that the static growth of 0.1 g gave the best growth results (i.e. tallest forest, fastest growth rate on average), but this high terminal height and growth rate can almost be achieved for forests grown at high forces initially. The growths represented by purple and green plots achieved this; the red one did not. It is even possible to increase the average growth rate, if the decrease in load is large enough. Additionally, there is very little separating the dynamic growths that underwent an increase in load from the growth under a static moderate force of 1.0 g. This means that increasing the load after a short period of growth will likely harm the growth, causing it to grow slower and shorter than its potential, but it will not prevent further growth from occurring unless the increase in force is too great or it happens too late in the growth process. Therefore, a single sudden change in load during growth can be used to control the terminal height, the growth rate, and consequently the microstructure.

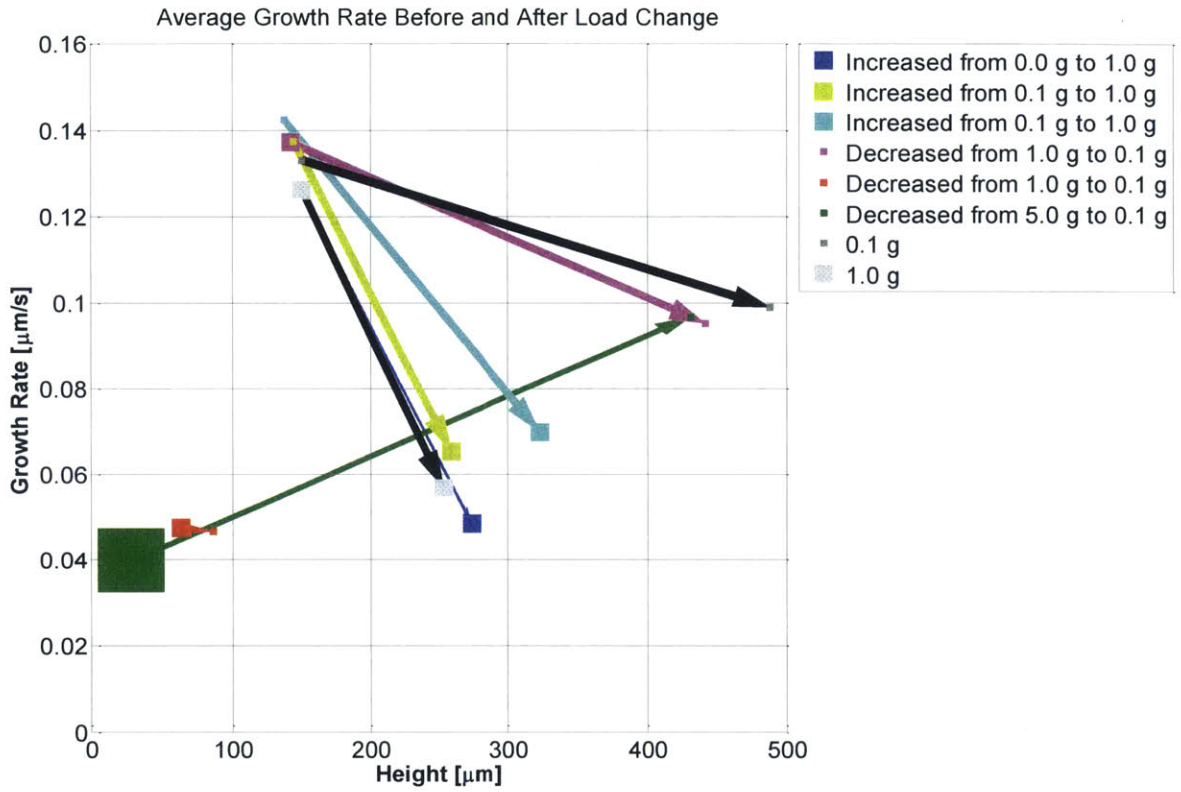

Figure 4.34 The average growth rate before and after load change for each experiment (colored arrows), along with two static force experiments (black arrows) for comparison. The first point corresponds to the height at which the load changed (taken to be 150 um for the static force cases), and the second point is the termination height. The size of the square points is proportional to the applied load.

4.5 Conclusions

To conclude, external forces have a large effect on the growth of carbon nanotube forests, and can change the achievable terminal height of the forest, the growth kinetics, and the morphology of the forest. These effects can be studied with the *in situ* force application and height measurement capabilities of the Mechanochamber system, coupled with post-growth characterization. It has been found that applied loads drastically limit the achievable height and average growth rate of a CNT forest. In addition, a load as small as 0.7 g can induce eventual buckling in the forest during growth, corresponding to a much smaller force than those typically required to buckle pre-grown forests. Applying time-varying loads has revealed further characteristics of CNT forest growth. It was found that a 3 g load can cause instantaneous buckling, a forest can resume growing at nearly the same rate if the load is suddenly increased, and a large enough decrease in load can allow for the forest to grow at a higher rate. Future experiments might reveal a method of improving the quality of CNT forests or the growth rate. For instance, a high-frequency cyclic force might be enough to break CNT-CNT contacts without the force being transmitted all the way to the growth front at the substrate, allowing for the CNTs to rearrange and become more aligned. Additionally, applying tensile forces to growing forests might be a way to improve the quality of growths by promoting the alignment of CNTs within the forest and providing mechanical energy to the growth front at the catalyst to increase the growth rate. External forces applied in a controlled manner can thus be used to administer changes to the forest morphology and to growth kinetics.

Chapter 5 Modeling of Mechanical Coupling between Growing Carbon Nanotubes

To complement the experimental observations of force-modulated growth, it is important to understand how CNT-CNT mechanical coupling can influence the growth process, and transmit externally applied forces to the catalyst. Simulations can provide a means of approximating these forces and further understanding the mechanism of mechanical coupling during growth. This chapter will present the framework for modeling the intrinsic forces that develop when CNTs become mechanically coupled during growth, and can be related to variations in the diameter and/or growth rate of CNTs coupled by van der Waals attraction. Simulations of the growth of a pair of CNTs are used to show the mechanism of contact formation and evolution, and it is found that the force acting on the catalyst can exceed 10 nN. Finally, a preliminary simulation of an 8 CNT array demonstrates the scalability of the model. This work was performed in collaboration with Abhinav Rao.

5.1 Analytical Model of CNT-CNT Interactions

A CNT forest consists of vertically aligned CNTs with a primary orientation direction yet typically significant tortuosity [77]. Locally, the CNTs can be grouped together as segments of CNTs in close proximity are drawn together due to van der Waals attraction forces (**Figure 5.1**). This mechanical coupling allows the CNTs to grow upwards collectively in the forest configuration, and it has been hypothesized that varying growth rates along with mechanical coupling cause waviness to develop as growth proceeds [28].

Molecular dynamics simulations and TEM studies have shown that the van der Waals forces cause local radial deformation of the CNTs within those contact regions [78]–[80], and the extent of the deformations depend on the diameter and number of walls of the CNTs [78]. The CNTs will bend to align in the contact region and the cross section of the CNTs will flatten, in a geometrical configuration as described by **Figure 5.2**. The CNTs will assume a geometry that minimizes the potential energy U_T between the contributions from elastic deformation and from van der Waals forces, and can be described as the sum of the elastic strain energy to bend the CNTs (U_S) and the potential energy of the contact (U_C):

$$U_T = U_S + U_C \tag{5.1}$$

The following discussion details the determination of each of the energy terms with a methodology derived by Abhinav Rao and colleagues [81].

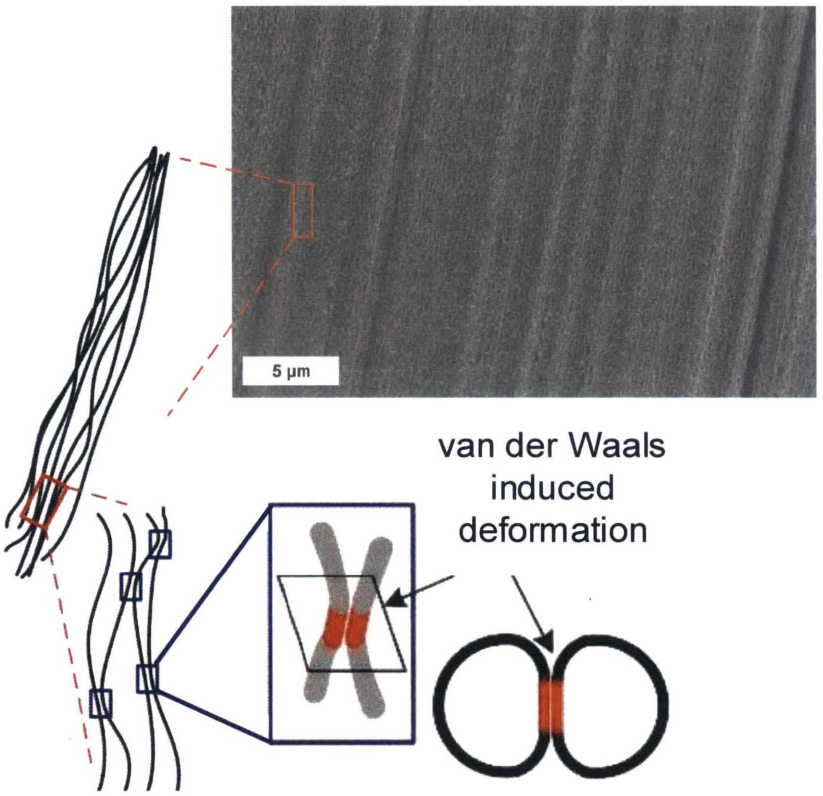

Figure 5.1 SEM image and schematics [81] illustrating the multi-scale phenomenon of mechanical coupling

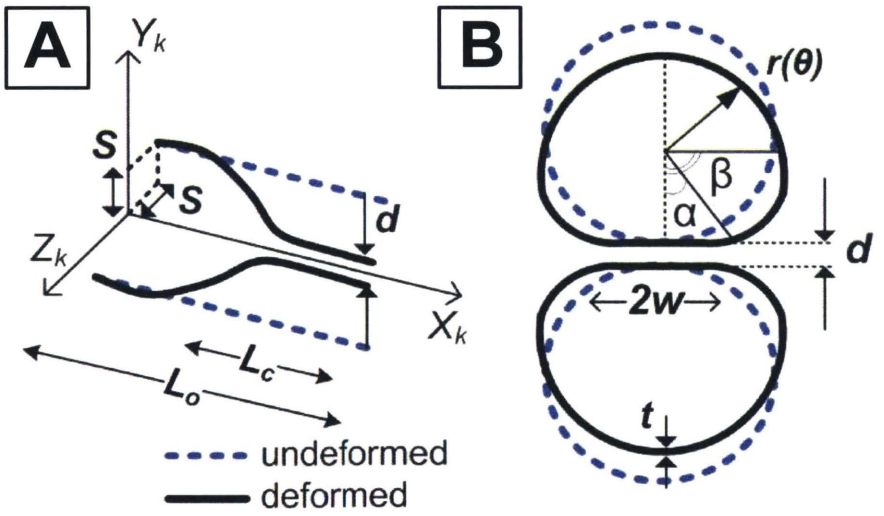

Figure 5.2 (A) Geometry of CNTs deforming to form a contact. (B) Cross section of two CNTs of equal diameter deformed by the contact [81].

Assuming a multi-walled CNT can be modeled as a series of concentric hollow cylinders, continuum mechanics can be used to find the elastic strain energy as a function of curvature (κ) using Bernoulli-Euler beam theory:

$$U_S = 2\int_0^{L_o - L_c} EI\,\kappa^2\,dx \tag{5.2}$$

The total length of the CNT that is deformed by the contact (L_o) and the contact length (L_c) are as shown in **Figure 5.2.A**. The flexural rigidity EI is the product of the axial Young's modulus E and the second moment of inertia I. For the representative CNT geometry of concentric hollow cylinders, having N walls, radius r, and wall thickness t, the second moment of inertia is given by

$$I = \frac{\pi}{4}\sum_{j=1}^{N}\left[\left(r_j + \frac{t}{2}\right)^4 - \left(r_j - \frac{t}{2}\right)^4\right] \tag{5.3}$$

The potential energy of the contact can be determined by integrating the contributions of strain energy from radial deformation and van der Waals attractions in a cross-sectional segment over the entire contact length.

$$U_C = L_C\left(U_{CS} + U_{VdW\_c} + U_{VdW\_o}\right) \tag{5.4}$$

The strain energy per unit length from radial deformation can be found from plate theory [82] as

$$U_{CS} = 2\int_{\alpha}^{\pi} \frac{D}{2r(\theta)}\,d\theta \tag{5.5}$$

where D is the cylindrical rigidity of a plate and $r(\theta)$ is the piecewise radius of the deformed CNT cross section derived by Rao and described by **Figure 5.2.B** [81].

$$r(\theta) = \begin{cases} h\left(1 + \dfrac{\theta^2}{2}\right) & 0 \le \theta < \alpha \\ a_0 + a_1(\theta - \alpha) + a_2(\theta - \alpha)^2 & \alpha \le \theta < \beta \\ r_d & \beta \le \theta \le \pi \end{cases} \tag{5.6}$$

Here α and β are sector angles, r_d is the radius at the top, and the constants are determined through geometric continuity. The angle α determines the sector that forms the width of the contact, given by

$$w = \int_0^{\alpha} r\, d\theta \tag{5.7}$$

The last term needed to determine the strain energy of radial deformation is the cylindrical rigidity D, which can be found using the radial Young's modulus E, Poisson's ratio v, and thickness h:

$$D = \frac{Eh^3}{12(1-v^2)} \tag{5.8}$$

The other terms determining the potential energy of the contact are a result of the van der Waals adhesion energy for the hollow cylinder geometry. These terms can be obtained using the extension of the interatomic potential across a surface, removing the hollow region with superposition of the surface potentials[83]. There are two terms for the van der Waals adhesion, one for the section of the CNT walls in contact with each other (U_{VdW_c}) and one for the remaining section of the walls in the cross-section (U_{VdW_o}).

$$U_{VdW\_c} = -w\left[\frac{A}{12\pi}\left(\frac{1}{d^2} - \frac{1}{(d+2t)^2}\right)\right] \tag{5.9}$$

$$U_{VdW\_o} = -\frac{1}{2\pi}\left(\frac{A}{12\sqrt{2}}\right)\int_{\alpha}^{\pi}\left\{\left(\frac{R^{1/2}}{d^{3/2}} - \frac{(R-t)^{1/2}}{(d+2t)^{3/2}}\right) - \left(\frac{\{r(\theta)\}^{1/2}}{d^{3/2}} - \frac{(r(\theta)-t)^{1/2}}{(d+2t)^{3/2}}\right)\right\} d\theta \tag{5.10}$$

Here, d is the separation between CNTs, R is the undeformed radius, and A is the Hamaker constant [81]. The total potential energy of the contact can then be determined by substituting Eq. 5.5, 5.9, and 5.10 into Eq. 5.4.

The equilibrium geometry after a contact is formed can now be obtained by minimizing U_T with respect to the contact length L_C and the sector angle α. The resultant contact width and length determine the strength of the contact. The capacity of the contact to withstand a normal force is given by

$$F_n = \left(\frac{A}{6\pi d^3}\right) wL_c \tag{5.11}$$

In addition, the capacity of the contact to withstand a shear force can be found by

$$F_s = \tau w L_c \tag{5.12}$$

where τ is the interfacial shear strength [81], [84], [85]. A contact will break if the effective shear force capacity F is overcome by external forces. With increasing distance between the two CNTs forming the

contact, F will become smaller as the van der Waals attractions weaken, until essentially no attractions are felt beyond a distance of δ_{max} (**Figure 5.3**). This method is used to calculate the strength of all CNT-CNT contacts throughout an assembly of CNTs in the subsequent sections.

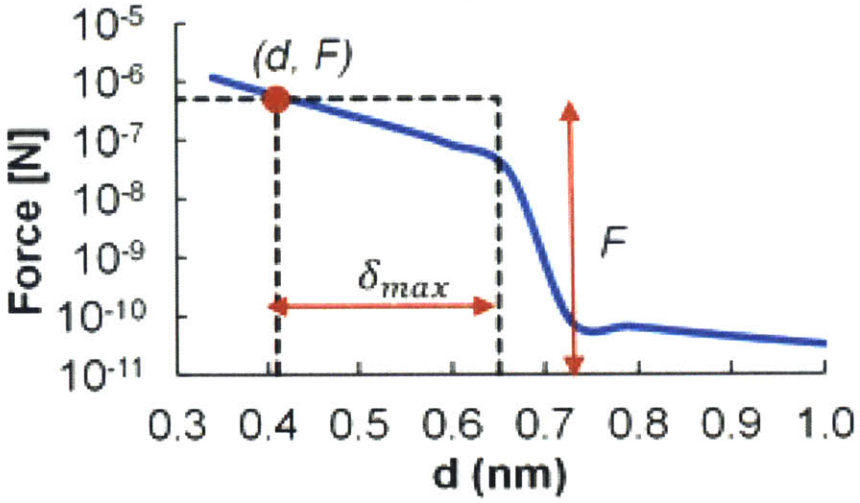

Figure 5.3 Plot of strength F of a contact with distance d between CNTs, showing the abrupt drop in strength as the distance exceeds a threshold δ_{max} beyond which the van der Waals attractions are weak.

5.2 Simulation Framework and Finite Element Structure

This simulation framework is based on a model developed by Abhinav Rao for modeling the strength of CNT yarns. It involves creating an array of CNTs of a short initial geometry, analytically computing contact properties, and simulating growth by adding segments at the base of the CNTs. The framework of the simulation performed in MATLAB, and the simulation step of the CNT growth is achieved with ANSYS finite element software. The steps involved in running a simulation are described by **Figure 5.4**, and a visual representation of the effect of the key steps on the CNT geometry is shown for two CNTs in **Figure 5.5**. First, an array of CNTs is created, with initial geometry of short straight segments of length L_{init} at angle θ and spacing s (**Figure 5.6**). Relevant CNT property constants used are shown in **Table 5.1**.

The CNTs are represented by nodes, spaced equally apart in 1 nm increments in the y direction. The first node starting at $y = 0$ represents the position of the catalyst on a substrate. Other information about the CNTs, including their diameters d and number of walls N_{walls}, are specified. Then, there is a search for any contacts between CNTs that fall within the δ_{max} range of the van der Waals attraction. Once located, the contact strength, width, and length are analytically computed for each contact, according to the method described in **Chapter 5.1**.

Growth segments are then added to the bottoms of the CNTs, with CNT-specific length L_{add}

$$L_{add} = V_d \Delta t \tag{5.13}$$

V_d is the diameter-dependent growth rate, and Δt is the simulation time step. The segments are added in a direction so as to continue the trajectory of the bottom two points of the CNTs. The diameter dependence of the growth rate is approximated from an expression derived to fit an analytical model by Puretzky *et al.* [61] to experimental data of forests of MWNTs grown in a cold-wall CVD reactor [28]:

$$V_d = 0.111d^2 - 0.02d + 0.36 \tag{5.14}$$

where the CNT diameter d is in nm, and the growth rate V_d is in μm/s. The analytical model by Puretzky takes into account the diameter-dependent kinetics of the reactions occurring simultaneously at the catalyst during CNT synthesis, with the result of a positive correlation between growth rate and CNT diameter. Some examples of growth rates calculated from Eq. 5.14 for some diameters used in simulations are shown in **Table 5.2**. The growth segments are added in the negative y direction so that the initial CNT segments remain in the same location.

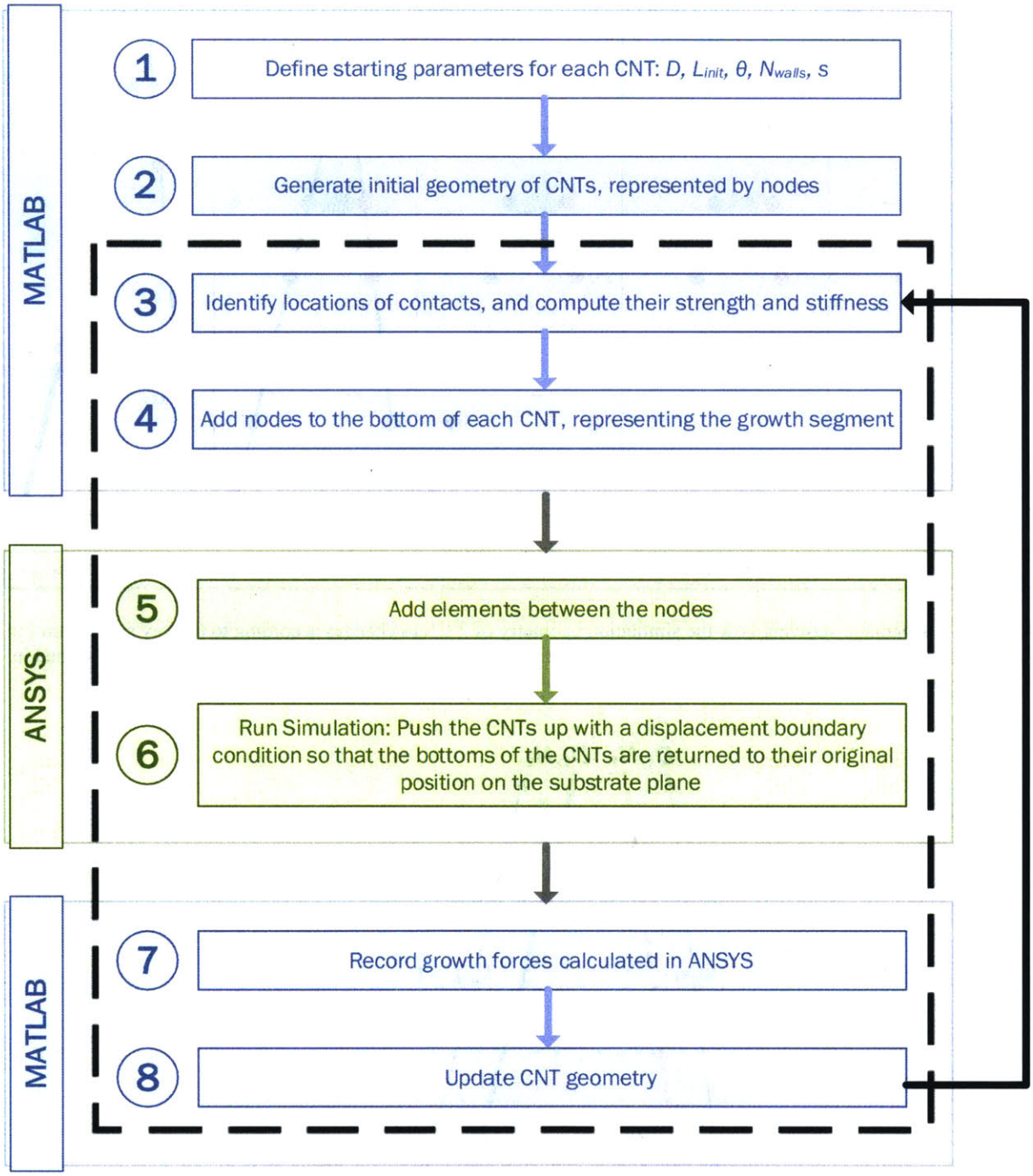

Figure 5.4 Schematic showing the workflow of performing a CNT growth simulation using a custom MATLAB code and ANSYS finite element simulation software.

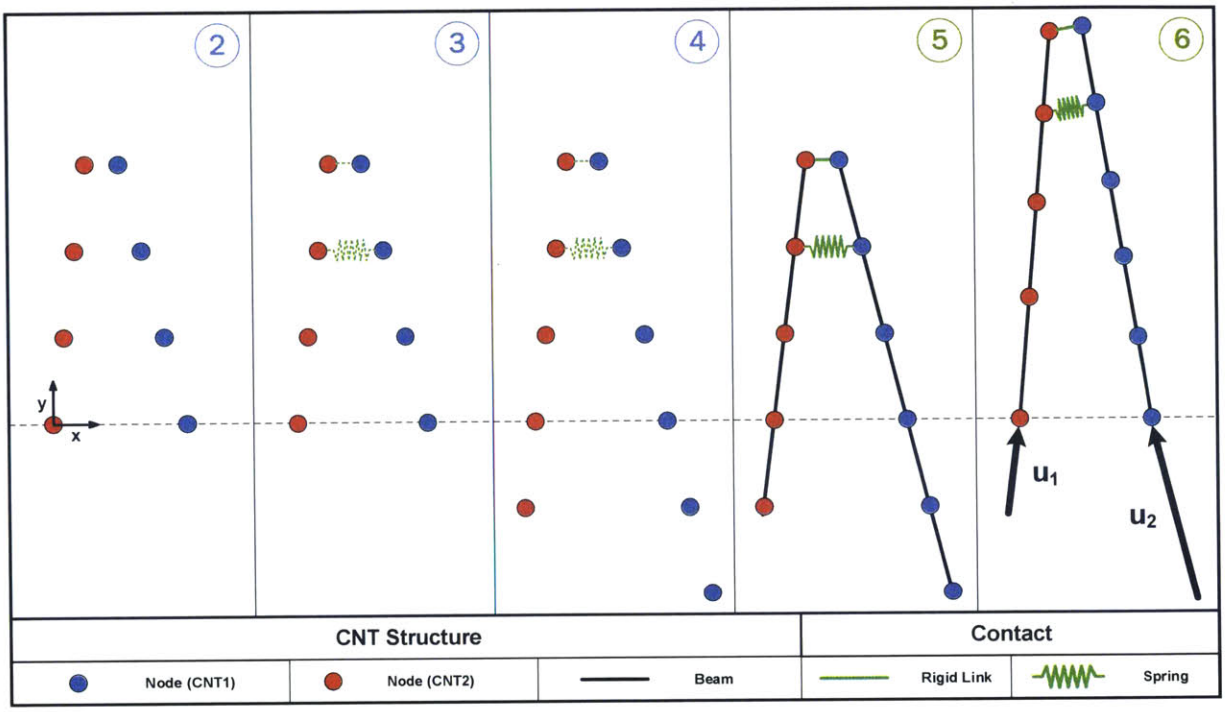

Figure 5.5 Schematic showing how the simulation geometry of 2 CNTs changes according to the key steps from Fig 4, along with descriptions of each element. Steps 2-4 are performed in MATLAB; Steps 5 and 6 are of performed in ANSYS. The dotted line represents the substrate that the CNT catalyst rests on.

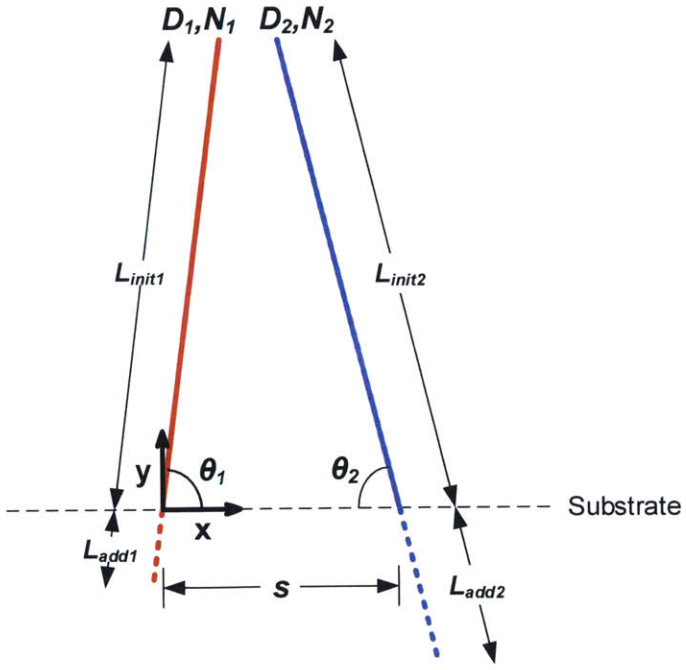

Figure 5.6 Initial geometry of two CNTs, with diameter D, number of walls N, initial length L_{init}, added length L_{add}, angle from the substrate θ, and spacing between CNTs s.

Property	Value
Minimal Interlayer spacing of MWNT [86]	0.34 nm
Axial Young's modulus [87]	610 GPa
Radial Young's modulus [88]	4 GPa
Poisson's ratio [81]	0.15
Hamaker's constant [81]	6 x 10-19
CNT mass density [81]	2200 kg m-3

Table 5.1 Relevant Properties of Multi-walled CNTs

Diameter [nm]	Growth Rate [μm/s]
6	4.2
7	5.6
8	7.3
9	9.1
10	11.2
11	13.5
12	16.1

Table 5.2 Diameters and corresponding growth rates for a series of simulations varying the smaller CNT diameter

For CNTs that do not have any contacts, the CNT position is redefined in MATLAB so that the bottom of the added segment is moved to the catalyst base position at $y = 0$ and the rest of the CNT is moved upwards, representing CNT base-growth. If there are CNT-CNT contacts, the geometries and properties of the CNTs forming the contacts are sent to ANSYS. ANSYS builds the mesh of CNTs with elements as shown schematically in **Figure 5.5**. To create a CNT structure, nodes are connected with a beam element (BEAM188). The contact is represented with a single complex element (COMBIN40) connecting the bottom nodes of the contact, composed of two springs as shown in **Figure 5.7**. The first spring has a stiffness K1 defined by the contact stiffness that had been computed analytically, with a maximum value determined by contact strength F. That spring is on a slider so that the contact can be broken without causing a convergence issue in the simulation if the force required to pull the contact apart is exceeded. The other spring has a piecewise stiffness that has a magnitude in tension of only 0.01% of K1, but an extremely high stiffness in compression representing van der Waals repulsion. Nodes that are already closer than $\delta_{min} = 0.34$ nm (the minimum interlayer spacing of MWNTs found experimentally [86]) are joined together with a rigid link element (MPC184) to ensure that the simulation does not allow for the CNTs to be pushed closer than physically possible.

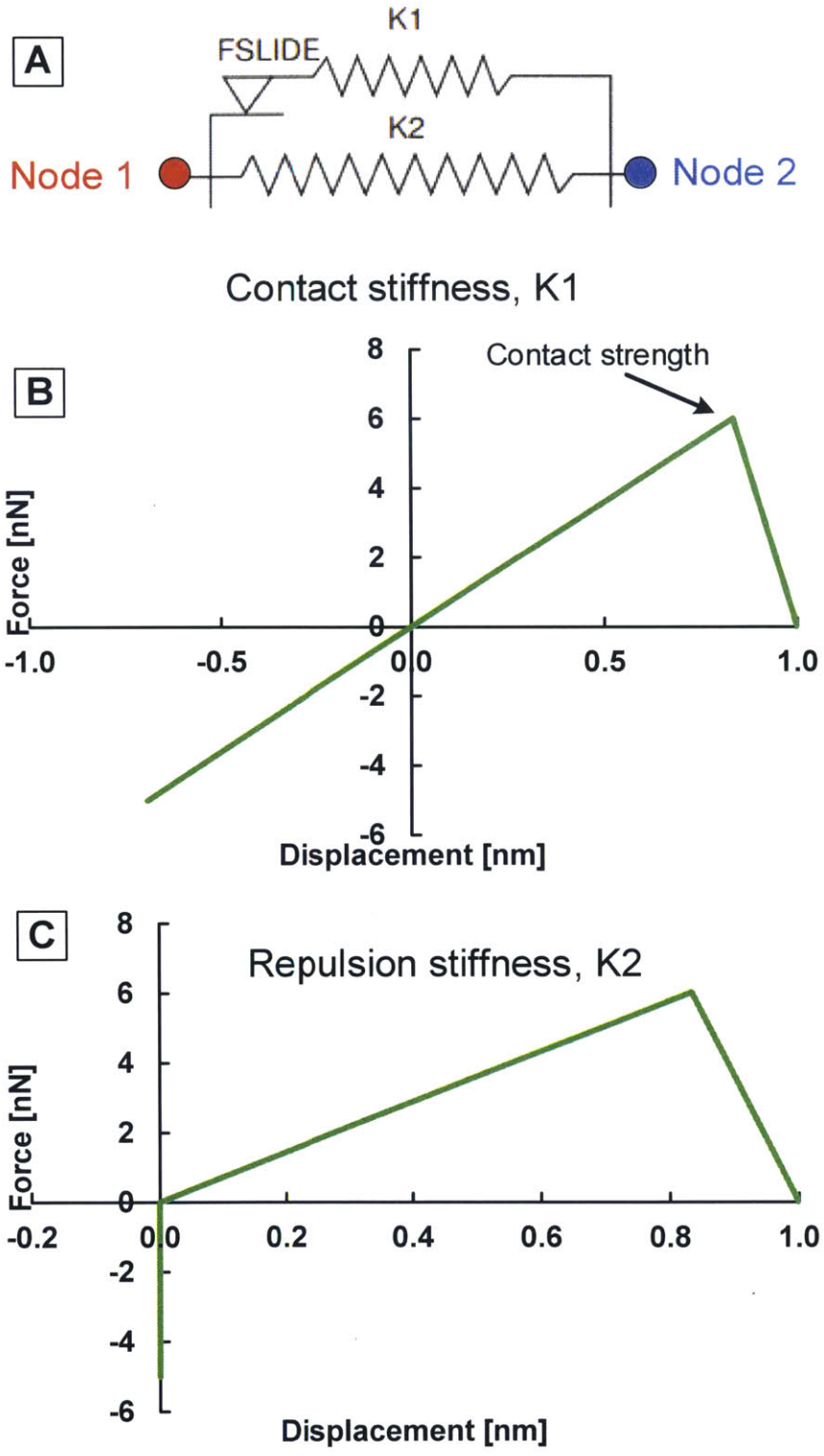

Figure 5.7 (A) Schematic of combination spring element used for contacts. The top spring can slide to allow for disengagement if the distance it is pulled exceeds δ_{max}. (B). Custom stiffness law for the attractive part of the

contact, which breaks at the analytically computed contact strength. (C) Custom stiffness law for the repulsive part of the contact.

Once the elements are added, a simulation is run using ANSYS, displacing the CNTs to move the bottom of the added segments to the catalyst base positions. Pushing the CNTs up from below the x-axis to their original start positions is akin to having the added segment grow out of the catalyst. It is important to use this configuration to emulate the growth step using ANSYS because growing the CNTs in ANSYS allows for the springs to capture all of the interactions that occur during growth. Forces in the CNTs develop during the simulation because the length of each CNT segment added is determined by the CNT growth rate. If a contact exists between two CNTs, the faster-growing CNT with the longer added segment will be put in compression and the slower one in tension. The distribution of these forces and the resulting CNT geometries are returned to MATLAB and recorded so that the next growth step can begin with the updated geometry. The simulation is completed after a pre-defined number of steps have been performed.

5.3 Simulations of Two CNTs in Contact

To understand the effects of mechanical coupling on CNT growth in the simplest of cases, simulations of the growth of two CNTs having different growth rates were performed. For each simulation, the CNTs were initialized as straight segments not in contact yet angled towards each other, as shown in **Figure 5.6**. All of the simulations were performed for the same amount of time steps, and unless otherwise stated, the CNTs shared the same parameters between each other and across simulations, which are listed in **Table 5.3**. Three series of simulations were conducted to test the effects of varying diameters, number of walls, and starting geometry on the force each CNT experiences, on the force that develops at the catalyst base, and on the final geometry of the pair.

Parameter	Value
Diameter of CNT1 [nm]	8
Diameter of CNT2 [nm]	11
Growth Rate of CNT1 [μm/s]	11.2
Growth Rate of CNT2 [μm/s]	13.5
Number of Walls	4
Initial Length [nm]	100
Initial Angle (degrees)	80
Spacing [nm]	50

Table 5.3 Parameters used in 2-CNT simulations

5.3.1 Varying Diameters

A series of simulations was performed to test the effects of varying the diameters of the CNTs, which is assumed to be the most important variable in determining catalyst force as it affects the growth rate of the CNTs, their stiffness, and the strength of the contact they can form. A nominal simulation of CNTs of diameter 9 nm and 11 nm (growth rates of 9.1 μm/s and 13.5 μm/s, respectively) was conducted. **Figure 5.8** shows the force on the catalyst, defined as the resultant force on the bottom element of the CNT, versus the mean CNT height throughout the simulation. The CNT with smaller diameter and slower growth rate is always in tension as indicated by the positive red line on the plot; the larger, faster CNT is always in compression (blue). Surprisingly, the force throughout the simulation is orders of magnitude larger than the force per CNT shown in **Chapter 4** to affect the growth kinetics of a forest. The growth force is in the range of tens of nN for the simulation compared to 0.1 nN in experiments with 12.5 kN/m^2 applied load (assuming 10^{10} CNTs/cm^2). This simulation suggests that even with relatively similar diameters and growth rates, the

stresses induced by mechanical coupling during growth may influence the quality and straightness of CNTs, as well as the growth rate.

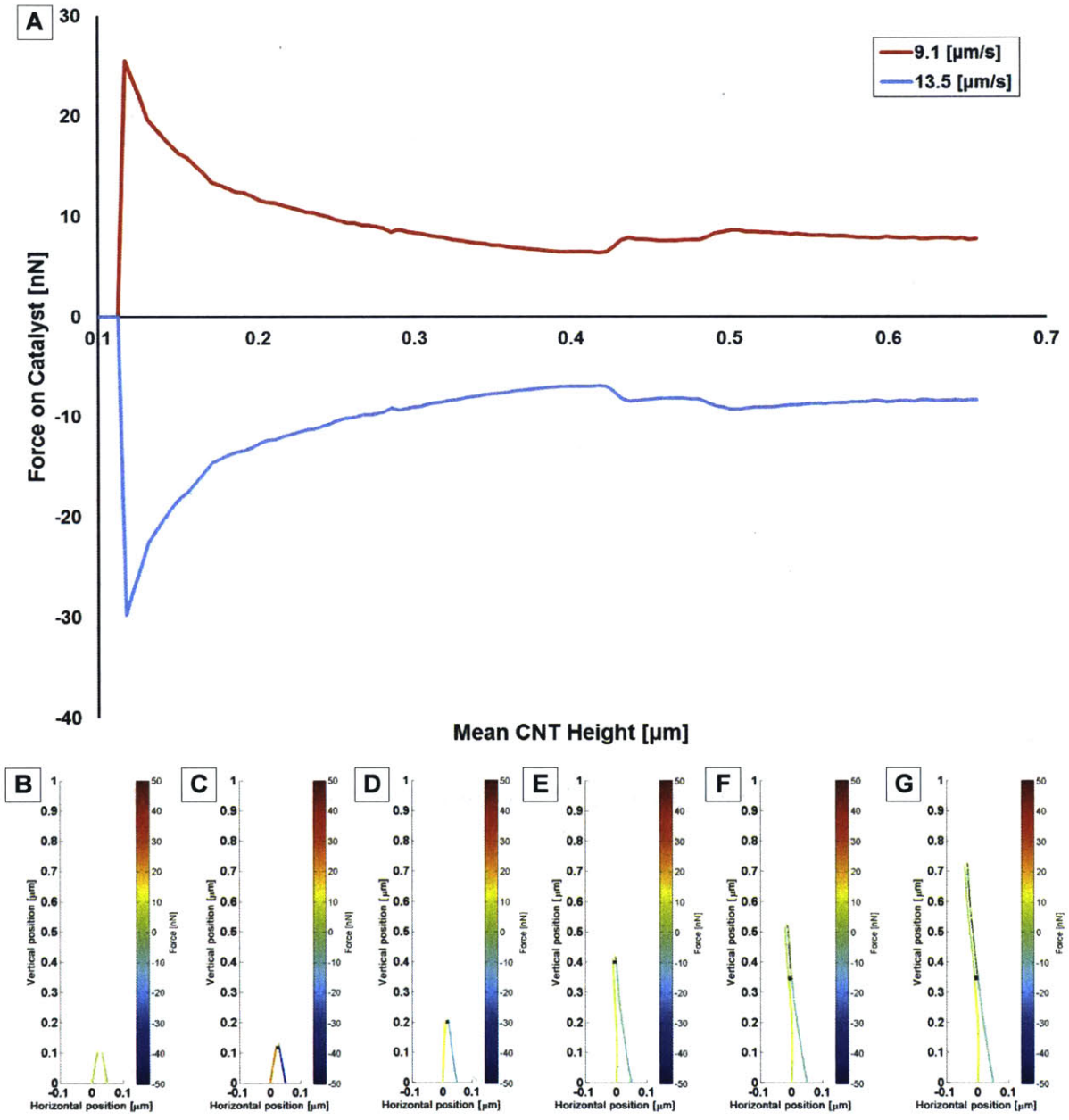

Figure 5.8 (A) Plot of force on the catalyst vs. mean CNT height for two CNTs of varying growth rates throughout a nominal simulation. (B-G) Map of force throughout each CNT (colored lines) at various stages of the simulation. Red is tensile and blue is compressive force. A contact is represented by a black line joining the two CNTs.

Also shown in the figure are colormaps of force on the two CNTs at various times throughout the simulation. The force initially starts at zero as the CNTs are uncoupled (B), yet increases rapidly and reaches a maximum after the CNTs come into contact and the differential growth causes the CNTs to bend (C). With subsequent growth, the force relaxes as the CNTs lengthen such that the bending strain is reduced (D,E). Eventually, the bending strain relaxes such that the CNTs become nearly parallel and the nodes underneath the contact are pulled within the δ_{max} threshold distance for van der Waals attraction forces, causing those nodes to join the contact (F). The contact length increases and the contact is strengthened. This results in a slight increase in the force on the catalyst as the flexural rigidity of the CNTs beneath the contact increases. As the simulation progresses (G), the CNT pair continues growing in roughly the same trajectory, the contact length continues to increase, and the force on the catalyst stays relatively constant over time.

Another simulation was performed with the same diameter for the larger CNT (11 nm), but decreasing the size of the smaller CNT to 8 nm. The resulting plot of force on catalyst vs. height is shown in **Figure 5.9**. The curves are noticeably less smooth than the previous simulation (**Figure 5.8**), with the discontinuities highlighted by the numbered labels. The first jump in force (not numbered) is when the CNTs first come into contact. The force relaxes slightly with some additional growth until the jump at (1), and similarly for (2). **Figure 5.10** shows colormaps of force on the CNTs, zoomed into the contact region at the CNT tips, for before (A,C) and after (B,D) the jumps in force. The dark black line connecting the CNTs represents the bottom of the contact, and the thin dashed lines are connecting nodes that are within the δ_{min} range of van der Waals repulsion forces. The reason for the jumps in the force plot at points (1) and (2) is that the contact is reforming with greater stiffness between steps. This forces the tips to bend slightly more, which in the colormaps is translated into the CNTs becoming darker colors, indicating that there is stronger coupling between the CNTs and greater forces that they exert on each other.

With further growth, the force on the catalyst decreases more until there is a brief dip in the force at (3) in **Figure 5.9**, highlighted in the colormap plots in **Figure 5.11**. The plots show three contacts near the CNT tips; the other two contacts had formed as more nodes were drawn within δ_{max} between points (2) and (3) on the force plot in **Figure 5.9**, as noted by the slight oscillations in the force. However, at point (3), the contacts break and slide down the CNT (**Figure 5.11.A** to **Figure 5.11.B**), furthering the alignment of the tips and moving many nodes away from the δ_{min} distance. The contacts move closer together (C), further increasing alignment of the tips, but without bending them as much. As a result, the tips are holding less force, but the increased stiffness of the contact is driving the parts of the CNTs below the contacts to bend more, causing an increase in the force plot. The CNTs are experiencing stick-slip behavior that CNTs are known to exhibit [89], [90]. This behavior was not evident in the previous simulation because the

diameter and growth rate differences were small enough for the CNTs to bend the amount needed to compensate for the growth mismatch to conform to each other without requiring too large of a strain energy penalty to do so. Finally, at point (4), as illustrated in **Figure 5.12** there is a large increase in force as the contact increases in size and shifts orientation, forcing the CNTs to bend more below the contact.

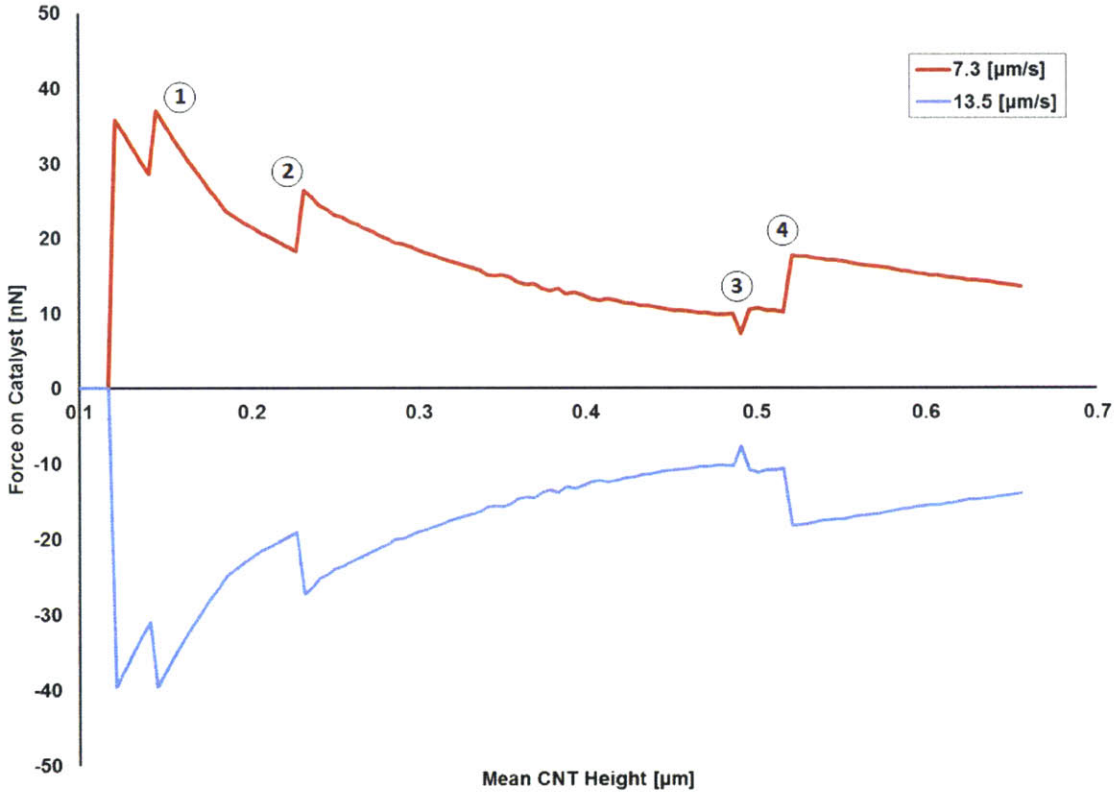

Figure 5.9 Force on the catalyst vs. mean CNT height for two CNTs with larger differences in growth rate than those of **Figure 5.8**. Moments of interest in the force plots are noted by numbers and further explained in **Figure 5.10-Figure 5.12**.

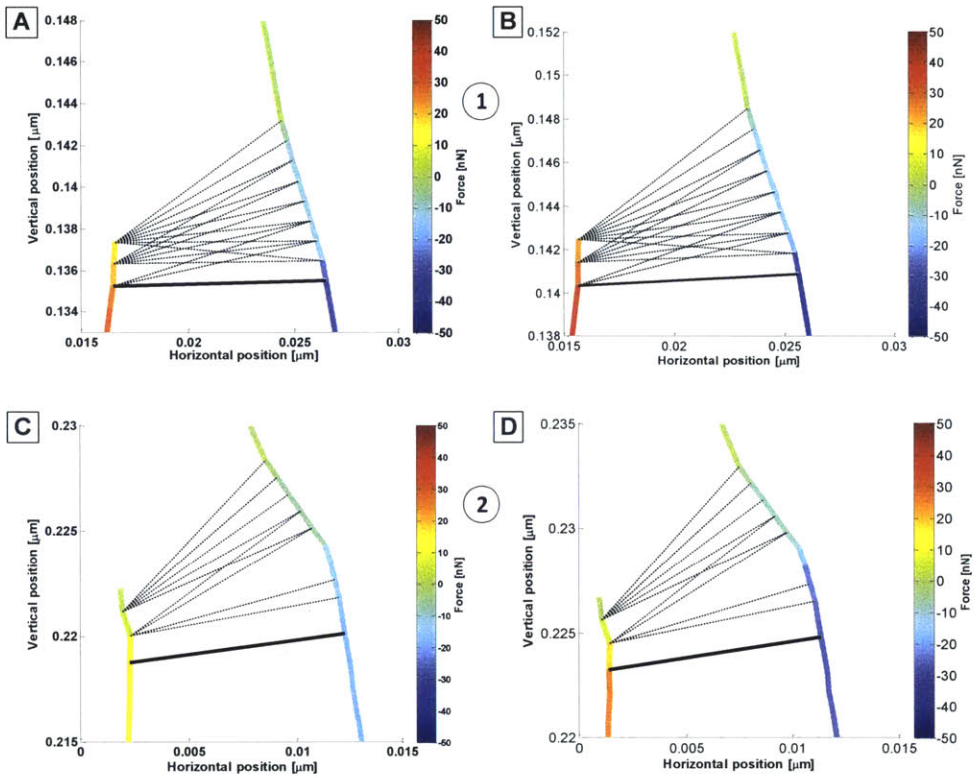

Figure 5.10 Map of force throughout the contact region at the tips of the two CNTs, before (A,C) and after (B,D) the early jumps (1) and (2) in the force plots of **Figure 5.9**. The CNTs are in color, the thick black line is the contact element, and the thin dashed black is the contact element, and the thin dashed black lines are rigid elements.

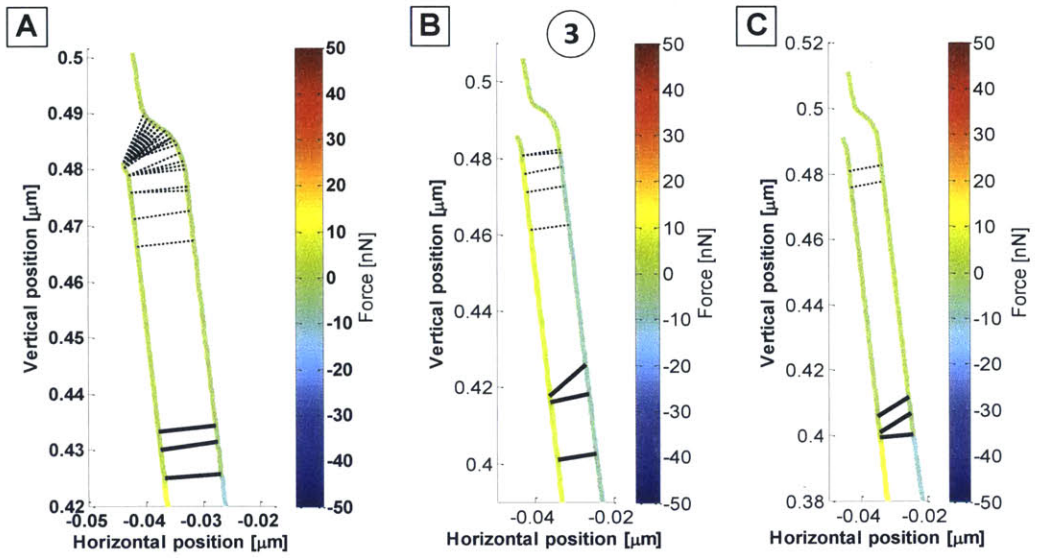

Figure 5.11 Map of force throughout the contact region at the tips of the two CNTs, before (A), during (B), and after (C) the dip (3) in the force plots of **Figure 5.9**.

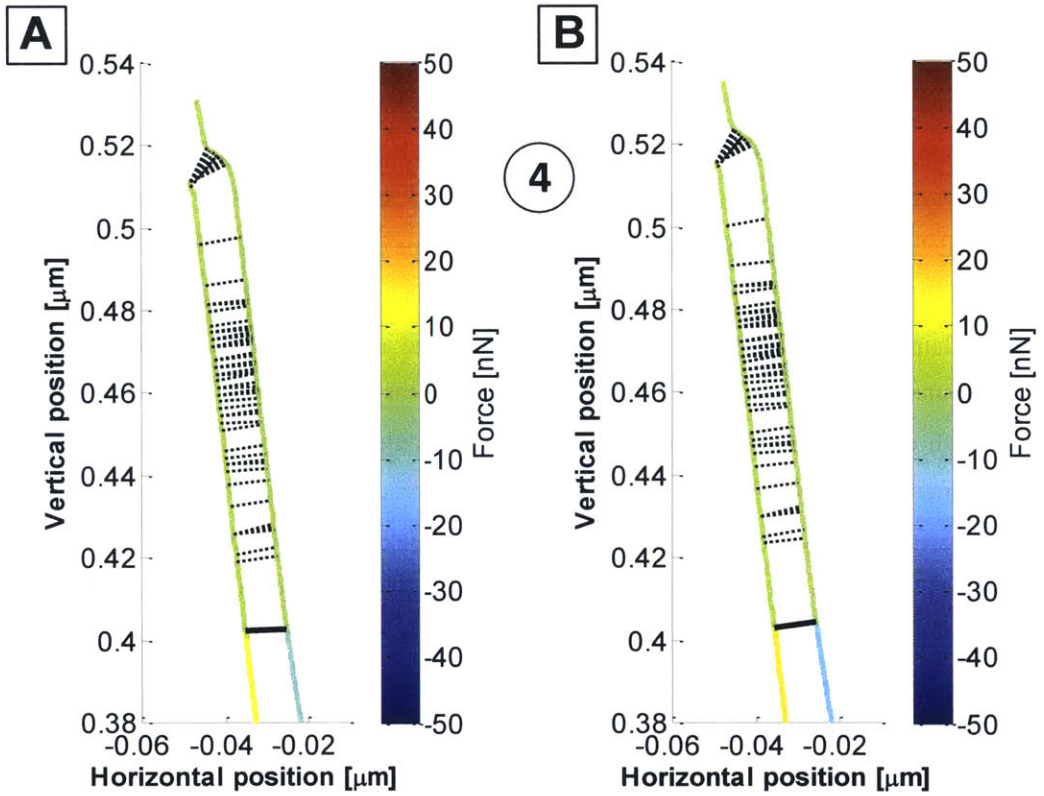

Figure 5.12 Map of force throughout the contact region at the tips of the two CNTs, before (A) and after (B) the large jump in the force plots of **Figure 5.9**.

The previous two simulations have elucidated the difference in contact behavior during a growth of a CNT pair for CNTs of small diameter difference and those of large enough diameter difference to cause stick-slip behavior. The following discussion will concern trends in the force on the catalyst and in the final growth height between simulations of increasing mismatch in diameter. The larger CNT for each simulation had the same diameter of 12 nm, and the smaller CNT diameter was varied from 6-11 nm. The corresponding growth rates are listed in **Table 5.2**.

The variation of final height of the simulation with increasing growth rate of the smaller CNT is displayed in **Figure 5.13**. The final height is defined as the average height between the CNT tips when the simulation ends. Also shown in the figure is a plot for reference of the height that a single CNT unrestricted by mechanical coupling would reach over the course of the same time period, using the same starting angle of 80° and initial length of 100 nm. Generally, the final height increases with increasing growth rate of the smaller CNT (decreasing difference in growth rate between the CNTs). However, with greater growth rates, the final height of a single CNT far surpasses what a coupled pair accomplishes; the coupling has a drastically limiting effect on the ability of the CNTs to translate growth into vertical gain as they become bent rather than staying perfectly straight.

Figure 5.14 shows the cumulative force on each catalyst throughout each simulation plotted vs. difference in diameters. For these, the diameter of the larger CNT was kept constant at 12 nm (growth rate of 16.1 μm/s), varying only the diameter (and thus growth rate) of the smaller CNT. It was seen that the force on the catalyst at any one point in a simulation can reach tens of nN; over the course of an entire simulation in which the CNT pair approaches 1 μm of height, the catalyst can feel a force in the μN range. Looking at the first point in the plot, a small difference in diameters allows for the CNTs to better conform to each other's shapes, increasing the strength of the contact and allowing for it to zip the CNTs for better alignment without requiring a large bending strain. With increasing difference in diameters and growth rates, the strength of the contacts is not enough to hold throughout the simulation; the contacts break, causing the segments of the CNTs near the contacts to be forced into increased bending to re-form the contacts. The growth is characterized by stick-slip, or the breaking and re-forming of contacts as the CNTs slide between each other However, enough stick-slip can actually cause the cumulative force to decrease, since there are repeated dips in the force that might ultimately sum to a lower force. Finally, at very large differences in growth rate and diameter, the strain energy to bend CNTs to extend a contact might be too great, so there is no strengthening and downward shifting of the contact that caused large jumps in force as noted in the discussion of **Figure 5.9**. This results in the decrease in magnitude of cumulative force on the catalyst for the largest difference in growth rate simulated.

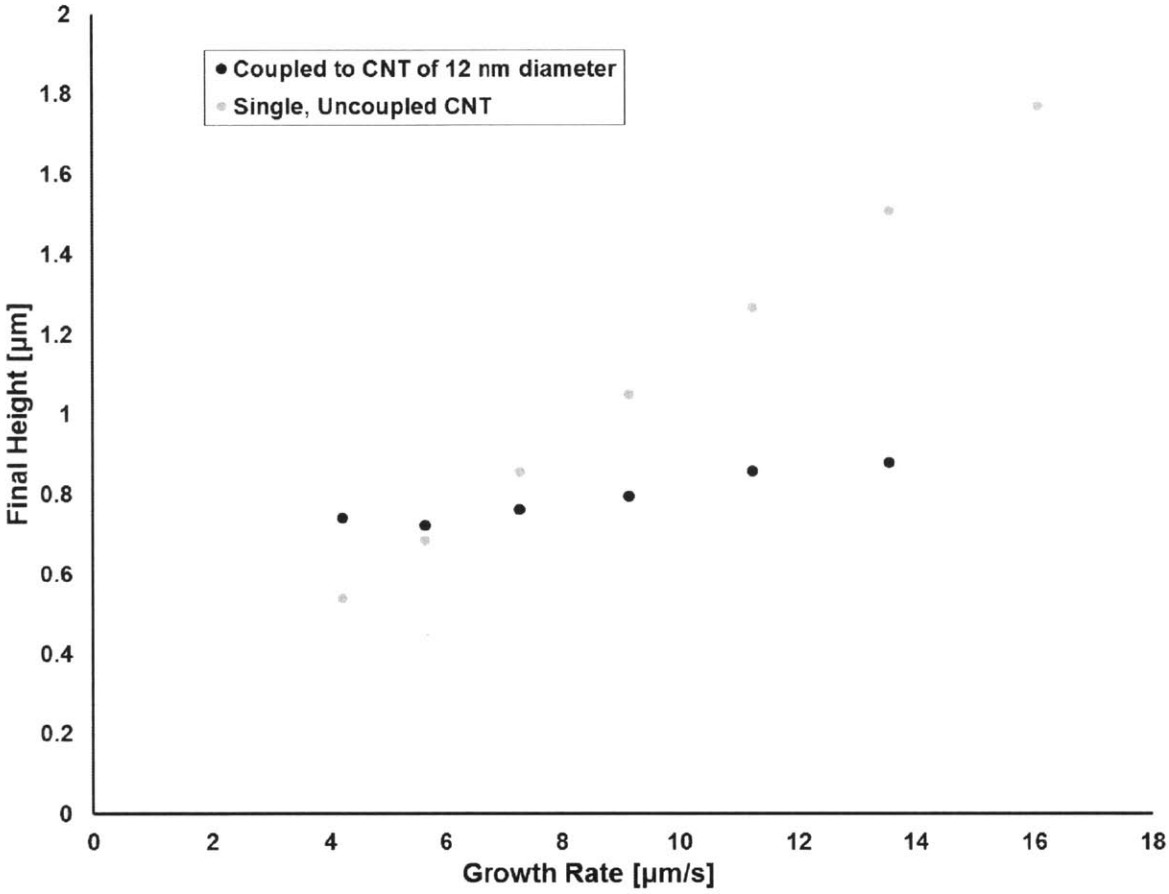

Figure 5.13 Final Height of the CNTs as a function of the growth rate of the CNT with smaller diameter (black). The gray points are a reference showing the height that a single CNT would achieve with each growth rate.

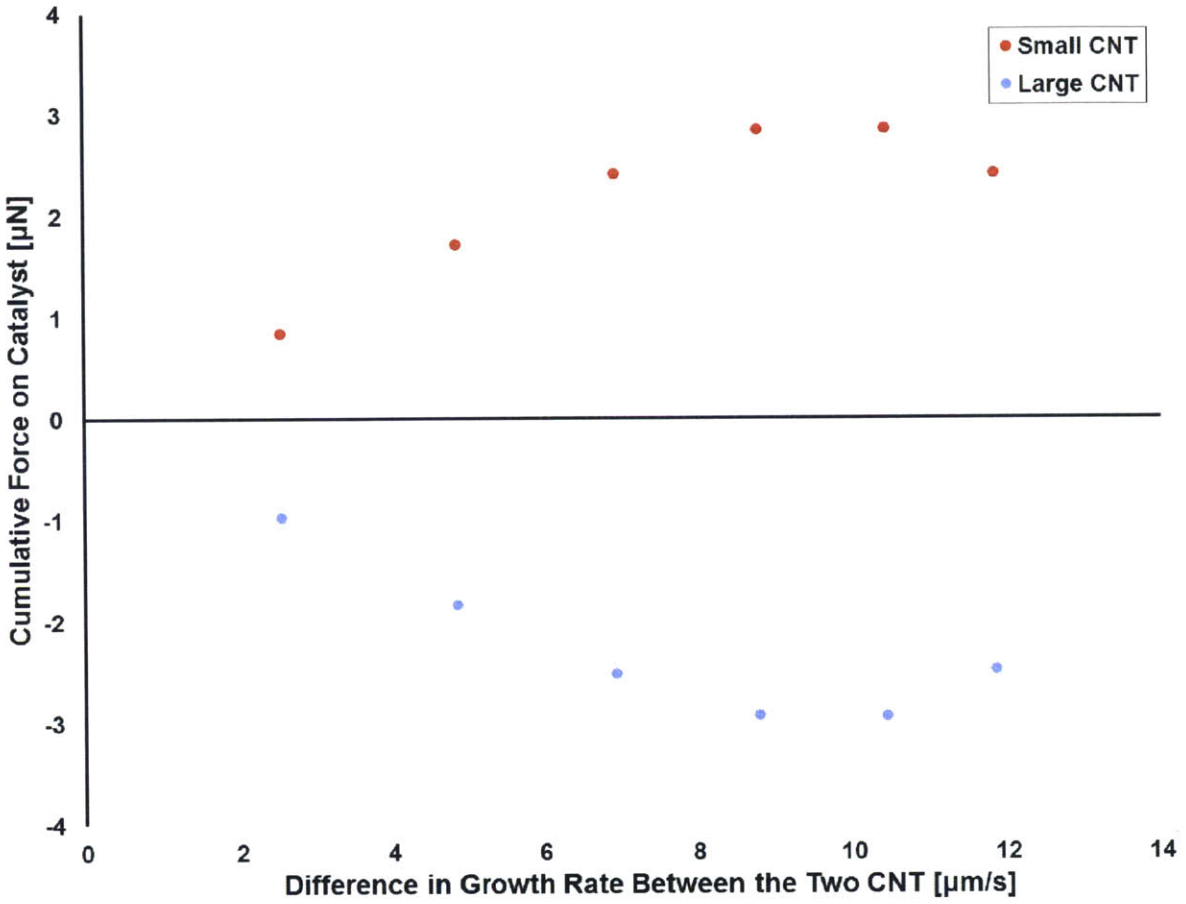

Figure 5.14 Cumulative force on the catalyst when the diameter of the small CNT (red) is changed, but that of the large CNT (blue) is kept constant at 12 nm.

5.3.2 Varying Number of Walls

Varying the number of walls is another way besides varying the diameters to alter the rigidity of the CNTs and thus the stiffness of the contacts they form and their degree of mechanical coupling. The number of walls was increased from 2 to 10 for a series of simulations. The resulting final simulated heights of the CNT pair are plotted in **Figure 5.15**. There is an unambiguous increase in the effective height with number of walls; increasing the number of walls increases the flexural rigidity of the CNTs, so they will not bend as easily and will grow straighter. **Figure 5.16** shows the effect of changing the number of walls on the cumulative force on each catalyst. Much like the trend for increasing difference in diameters/growth rates, increasing the number of walls results in an increase in force on the catalyst, but only up to a certain point. As the number of walls gets larger, the cylindrical rigidity increases, causing an increase in the strain energy

to radially deform the CNTs, decreasing the contact width along with the contact strength. Similarly, the increase in wall number increases the flexural rigidity, increasing the strain energy required to bend the CNTs into the contact, decreasing the resulting contact length and contact strength. The end result is that increasing the number of walls from a small number (e.g. 2 to 4) drastically increases the flexural rigidity and thus the bending stress that is caused by the mechanical coupling. But by increasing the number of walls (while keeping the same outer diameter), the contact stiffness is weakened to the point that stick-slip occurs, and the cumulative force on the catalyst does not increase significantly because the CNTs may grow uncoupled.

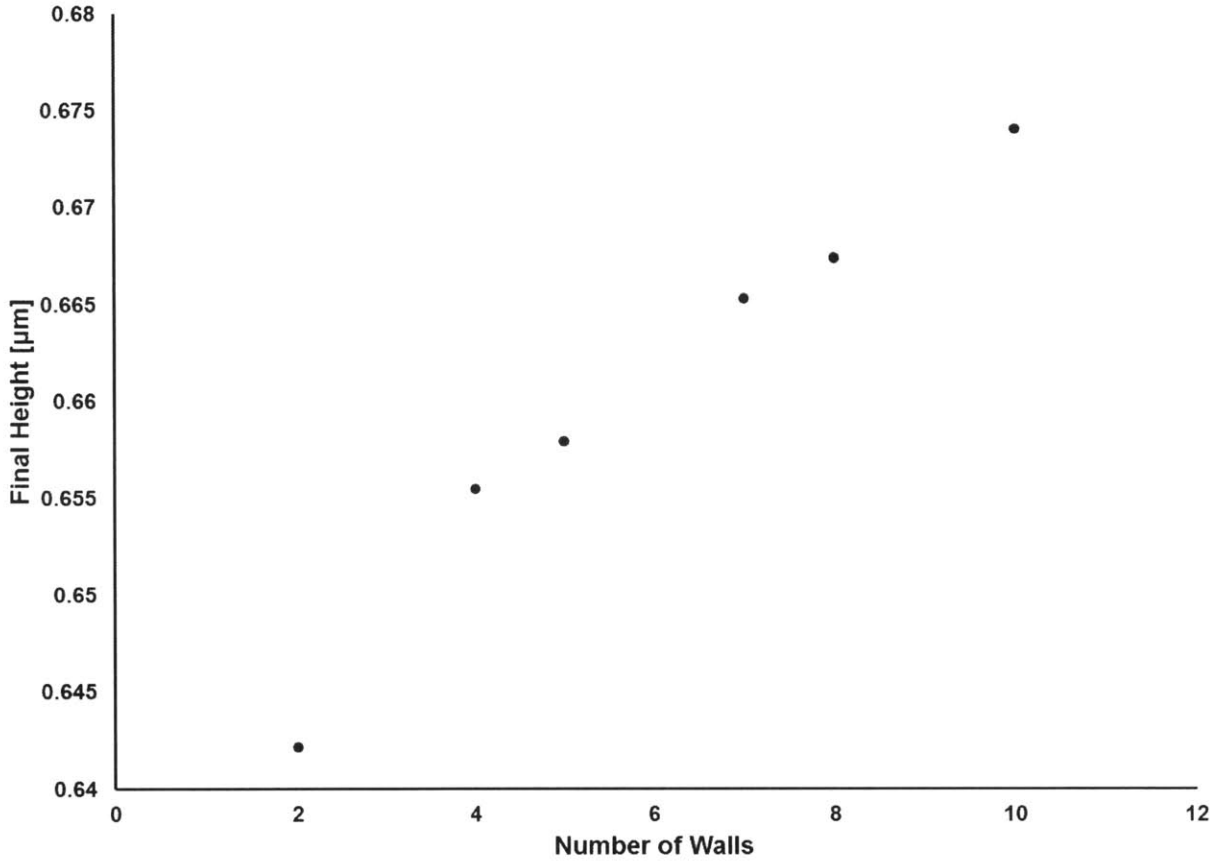

Figure 5.15 Final height when the number of walls of the two CNTs (each having the same number of walls) is changed between simulations.

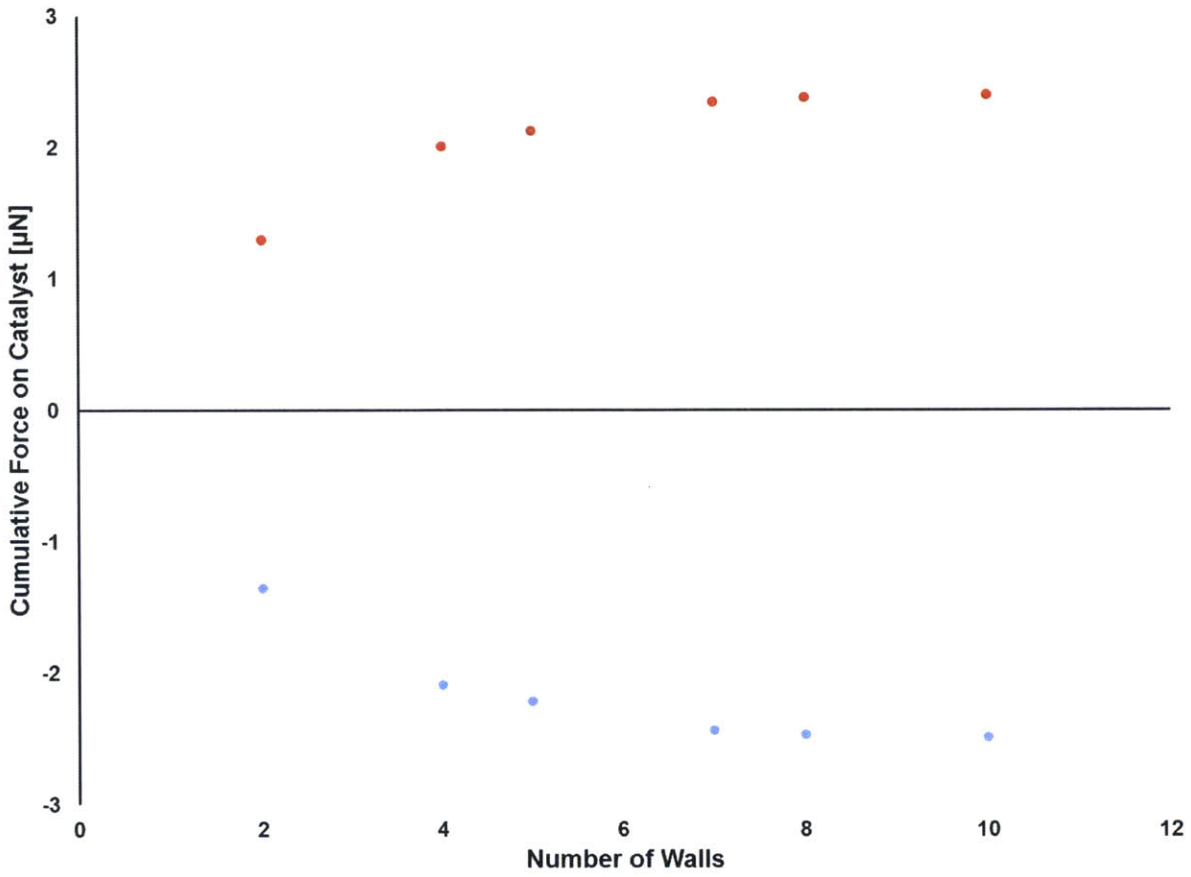

Figure 5.16 Cumulative force on each catalyst when the number of walls of the two CNTs (each having the same number of walls) is changed between simulations.

5.3.3 Varying Starting Angle

The final two-CNT study investigated the effects of changing the initial angle between CNTs. The starting angles here are defined as angles from the vertical axis (perpendicular to the substrate), as shown schematically in **Figure 5.17**. These simulations were conducted to understand how the CNTs compensate for misalignment when they come into contact. The smaller CNT is placed at the origin, and the larger one at a distance away so that there is a 5 nm lateral gap between the tips. Simulations were conducted with three different starting geometries:

1. both CNTs at the same angle $\theta/2$ (black)
2. the smaller CNT at angle θ and the larger CNT at 1° from the vertical (red)
3. the larger CNT at angle θ and the smaller CNT at 1° from the vertical (blue)

The final height of the CNT pair for the simulations is plotted vs. the starting angle θ from the vertical. For the smaller CNTs, the angle does not make a large difference as the smaller CNT becomes pulled along by the larger CNT once they form a contact. Increasing the angle from the vertical for the larger CNT, though, drastically reduces the growth height, since the larger CNT bends the smaller CNT to maintain roughly the same trajectory.

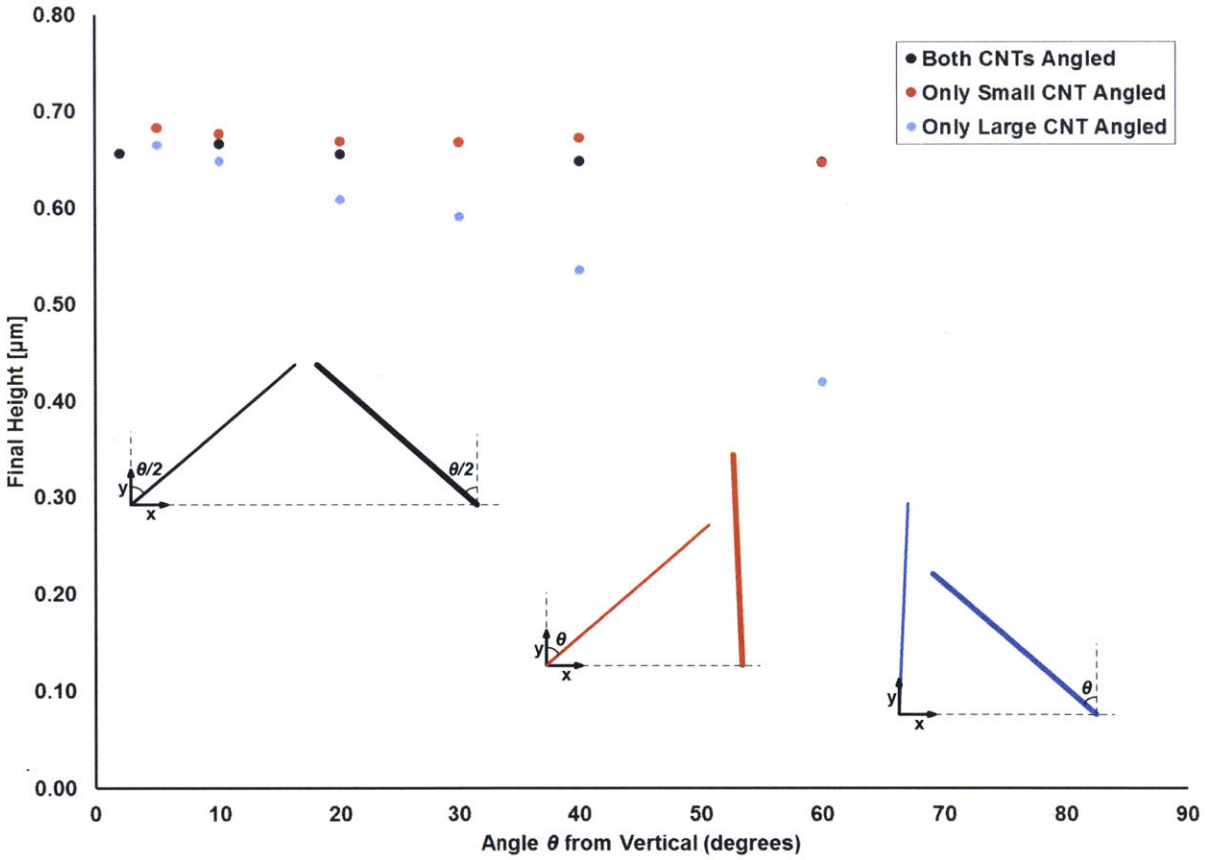

Figure 5.17 Final height when the angle from the vertical of (black) both CNTs, (red) the CNT of small diameter only, and (blue) the CNT of large diameter only is changed between simulations. The CNT with the smaller diameter in the schematics is the left one starting at the origin.

For the simulations in which both CNTs started at the same angle ($\theta/2$), the sum (θ) of the individual angles was used as the independent variable. The plot shows that if both CNTs start at the same angle, the ultimate height achieved by the CNT pair does not seem to dependent on that angle. Closer examination of the colormaps of force in the CNTs at the last step of each simulation (**Figure 5.18**) shows that with increasing θ the CNTs are actually growing more slanted while maintaining nearly the same average height.

Additionally, with increasing θ the disparity in tip height between the CNTs decreases because the contact forms closer to the tips. In comparing these colormaps to the cumulative force on the catalyst for each simulation (**Figure 5.19**), the same behavior of increasing θ (i.e. increasing the degree of misalignment and the CNT separation) as that of increasing the diameter difference and increasing the number of walls is prevalent. With small θ, the CNTs can align easily and there is hardly any bending stress (**Figure 5.18.A**). With increasing θ, the increase in bending stress as a strong contact is created and maintained (**Figure 5.18.B**) causes the force on the catalyst to increase. Further increase in θ and catalyst separation (**Figure 5.18.C,D**) results in weakening the contact as a greater bending strain is required to increase the contact length, so stick-slip occurs, decreasing the force on the catalyst. Finally, if the initial θ and separation are too large (**Figure 5.18.E**), the contact does not increase in size or strength, the CNTs are not forced to bend closer to the catalyst, and the force on the catalyst is reduced.

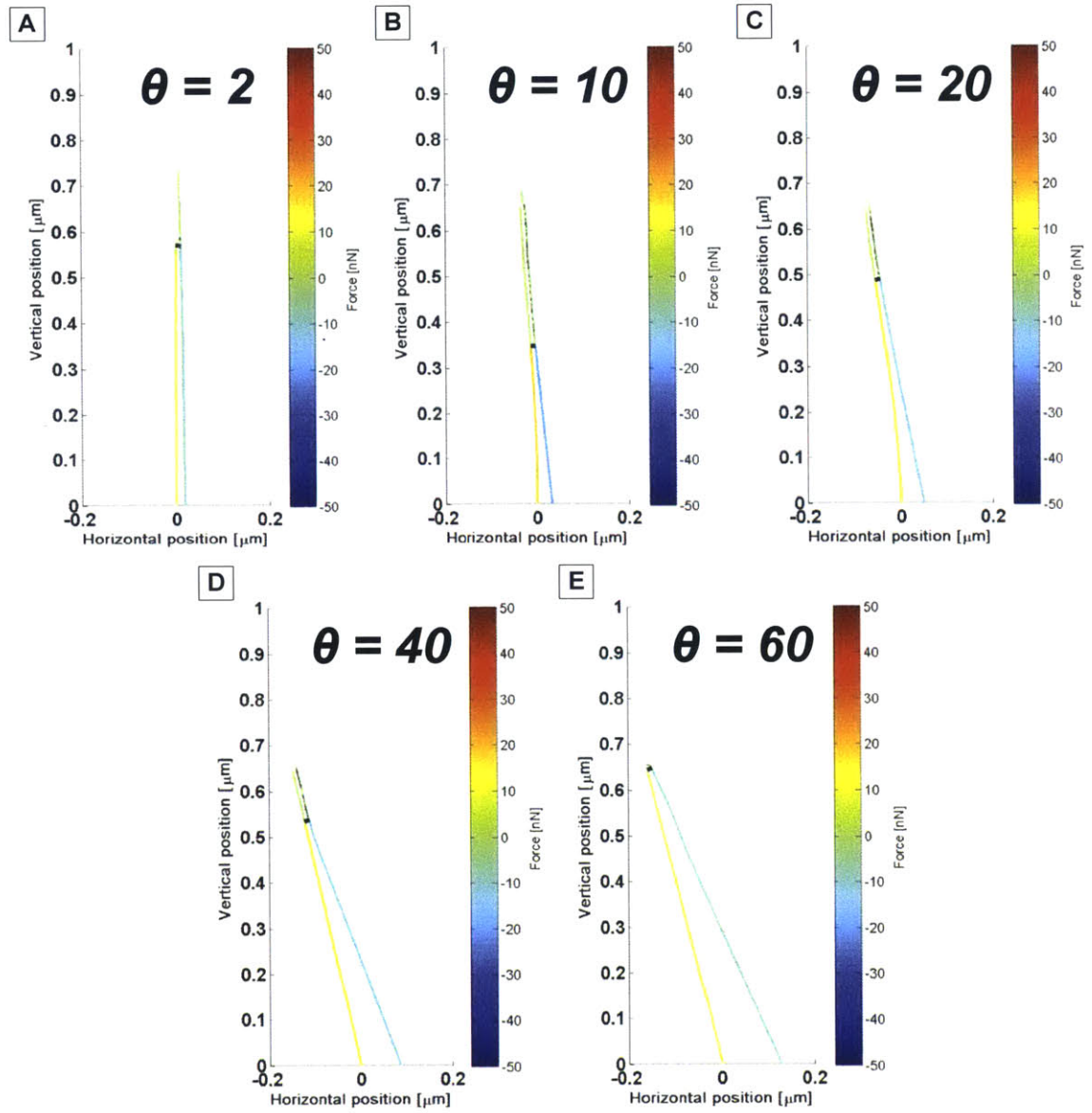

Figure 5.18 Colormaps of force in each CNT at the final step of the simulation for varying starting angle θ. Each CNT started at angle θ/2 from the vertical.

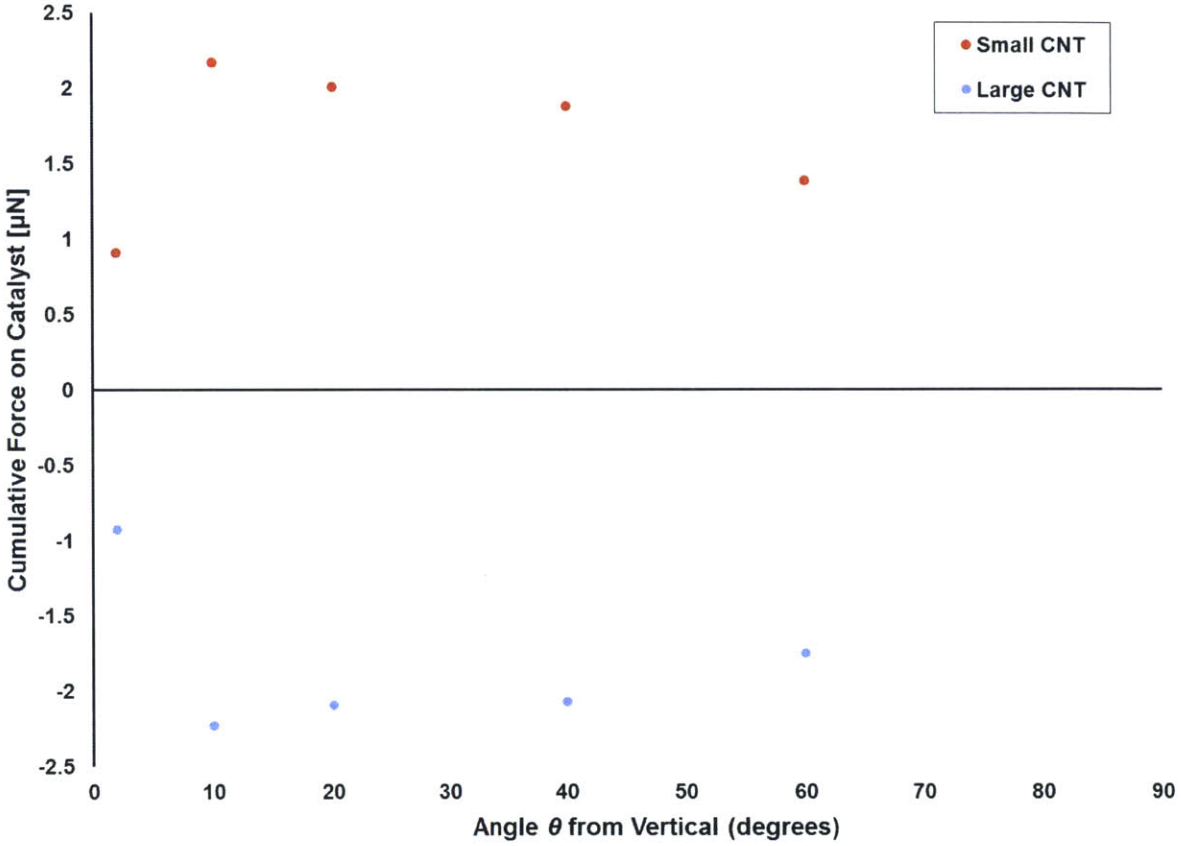

Figure 5.19 Cumulative force on the catalyst when the angle from the vertical θ/2 for both CNTs is changed. The force is plotted vs. the sum of the starting angles.

5.4 Simulation of an Array of CNTs

A growth simulation of an array of 8 CNTs was conducted to show the capabilities of this model to extend to larger sample sizes. The diameters and starting angles were chosen with a random normal distribution about a mean of 10 nm and 90°, respectively. The CNTs all had 4 walls, and started at a spacing of 5 nm with a length of 10 nm. Force colormaps of various stages throughout the simulation are displayed in **Figure 5.20**. This simulation demonstrates that CNTs will group, forming multiple contacts along their length. **Table 5.4** lists the cumulative force on each catalyst particle throughout the simulation. It is interesting to note that even for such similar diameters there is a vast range of catalyst forces from 88 nN to 3605 nN in magnitude. Additionally, half of the CNTs are in tension and half are in compression. Finally, the sum of the forces on the catalyst (and thus the force on the substrate) is compressive, suggesting that mechanical coupling might create compressive intrinsic stresses that could limit catalytic behavior.

Diameter [nm]	Cumulative Force on Each Catalyst [nN]
10.2	168
9.8	-88
9.1	2867
11.0	-3473
10.3	-211
10.4	156
10.8	-3605
9.2	3446
Total	**-739**

Table 5.4 Diameters and cumulative force on their respective catalyst for an 8-CNT simulation

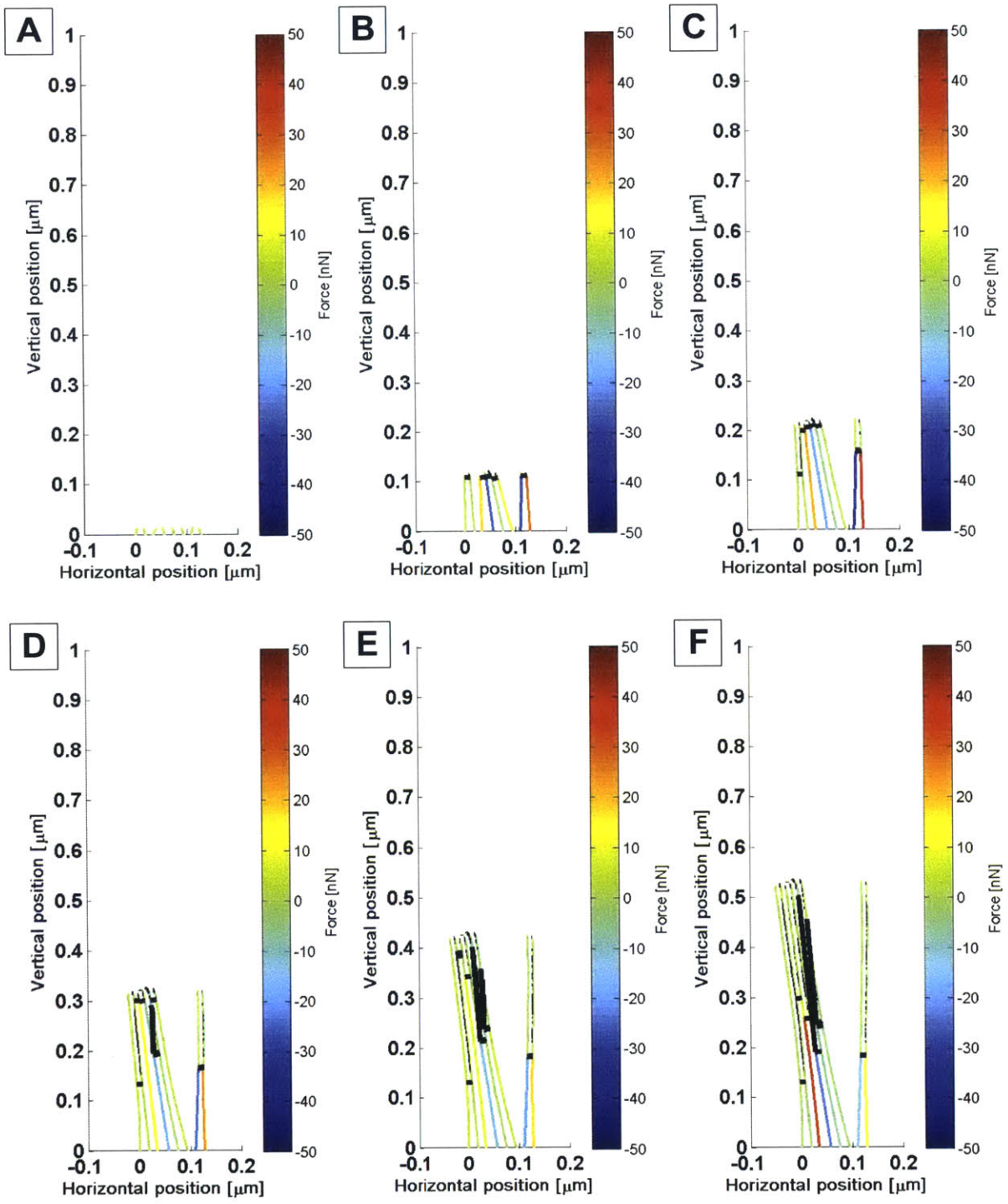

Figure 5.20 Colormaps of force in each CNT at various points throughout a nominal simulation of 8 CNTs of random diameter distribution and starting angles.

5.5 Conclusions

In this chapter, an analytical model that computes the strength and geometry of a CNT-CNT contact based on principles of energy minimization was implemented into a custom code with finite element modeling to simulate mechanical coupling in carbon nanotube growth. This code was used to discover the effects of mechanical coupling on the force and morphological development of growing CNTs. The findings from simulations of growth of two CNTs, and of one simulation of an array of 8 CNTs, are that:

1. Mechanical coupling causes tensile stress to develop in the smaller CNT and compressive stress in the larger CNT, which is transmitted to the catalyst at the base (assuming the growth rate is positively correlated with diameter as proposed by Puretzky *et al.* [61])
2. The magnitude of the force on the catalyst predicted by the simulation at any given time can exceed tens of nN, and can sum to μN during the time it takes two CNTs to grow to almost 1 μm in height. This is much larger than the extrinsic forces shown to affect the growth kinetics and morphology of forest growth (e.g. 0.1 nN for applied load of 12.5 kN/m^2 and density10^{10} $CNTs/cm^2$).
3. CNT-CNT contact behavior can fall within three regimes: (1) the contact is maintained throughout the simulation and can grow in length, (2) the contact breaks and reforms (stick-slip), and (3) the contact is maintained but does not grow in length
4. In general, transition from regime (1) to regime (3) occurs with increasing difference in diameter, increasing number of walls, and increasing separation at the base, as each of these results in increased strain energy penalty for bending the CNTs to increase the contact length
5. An array of CNTs will produce greatly varying stresses at the catalyst, even if the CNTs have similar diameters and growth rates.

The implications of these results are that mechanical coupling could have a significant effect on CNT growth kinetics, if the magnitudes of the forces created can be compared to the experimental studies of **Chapter 4**. This could potentially have a homogenizing effect on the collective forest growth, as faster-growing CNTs impart compressive stresses on the catalyst particles, possibly shifting the energetics of the reactions occurring at the catalyst and decreasing the growth rate of those CNTs. The opposite effect might also occur for slower-growing CNTs, as tensile stress might increase the growth rate of those CNTs, in effect equilibrating the growth rate amongst the CNTs in the forest. However, at this point, these are merely stipulations, and atomistic simulations are likely needed to discover the relationship between force and growth rate as a result of any change in catalytic activity. In addition, the actual relationship between diameter and growth rate has not been established, which would greatly affect the magnitude of the forces

involved. Further work on these points are needed to improve the accuracy of the model presented in this chapter.

this page intentionally left blank

Chapter 6 Conclusions and Future Work

The main goal of this thesis was to explore the influence of mechanical forces on the growth kinetics and quality of vertically aligned CNT "forests". First, using a custom-built CVD reactor with an internal micromanipulator, it was shown that compressive forces can alter the apparent growth rate and the collective morphology of CNT forests. Second, a finite element model was used to predict the strength of mechanical coupling between a pair of growing CNTs and the dynamics of force transmission to the catalyst which may influence the carbon precipitation process at the CNT-catalyst interface. The major insights and contributions of this work, as well a brief outlook for the extension of this work are highlighted below.

6.1 Insights and Contributions

The main insights and contributions of this thesis are:

- A custom-built CVD reactor was used to, for the first time, apply controlled and time-varying forces to CNT forests as they grow, and to monitor the growth kinetics in situ.
- It was found that compressive forces applied to a CNT forest during growth increase the time required for self-organization, slow the apparent growth rate, decrease the alignment, and reduce the growth lifetime. Specifically, static forces in the range of 0.1-10 g decrease the average forest growth rate from 0.23-0.03 μm/s (as measured by the rate of height increase). Additionally, time-varying forces can be used to induce a morphological change in the forest structure and modulate the apparent growth rate without causing termination of growth.
- Application of compressive forces can cause the CNT forest to buckle during growth, yet growth continues after buckling with much greater tortuosity until the growth process self-terminates.
- Finite element simulations suggest that mechanical coupling between CNTs causes them to experience dynamic forces during growth, and the magnitude of these forces depends on the relative growth rate, diameter, number of walls, initial angle from the substrate, and initial length constraint properties.
- The simulations also indicate that variation in these constraints changes the behavior of the contacts between CNTs, which affects the amount of force that is transmitted to the catalyst. For the range of constraints studied, the magnitude of cumulative force on the catalyst ranged from 0.9 μN to 2.9 μN over the same time frame.
- The force magnitude shown experimentally to influence the morphology and growth rate of a CNT forest (on the order of 0.1 nN) is much smaller than the force predicted by simulations to act on individual, mechanically coupled CNTs (up to 10 nN).

Therefore, this thesis has shown that both intrinsic and extrinsic forces can influence the morphology of CNTs growing in forests, and may be detrimental to the achievement of high CNT density and structural quality, which are essential for many practical applications.

6.2 Future Work

The findings described above suggest that forces hinder CNT growth, but can forces be used to improve CNT growth? This might be possible if forces can be applied in such a way so as to prevent or disrupt mechanical coupling without damaging the forest. This could potentially be accomplished by breaking CNT-CNT contacts without transmitting excessive load to the catalyst. Additionally, an applied electric field might allow for the application of electrostatic tension forces to increase the alignment of the CNTs. Electrostatic tension might also enable increased growth rate of the CNT forest, if it can be assumed that tension will have the opposite effect as compression.

However, it is necessary to understand the true nature of the effect of force on growth rate of individual CNTs, how forces are distributed on the catalyst, and how they affect the catalytic activity. For example, is there a force limit that results in immediate termination of growth if it is exceeded? Another vital piece of knowledge is the true relationship between CNT diameter and growth rate, as that informs the extent of mismatch in growth rates and the resulting forces that develop. Atomistic simulations of the carbon precipitation process or in situ TEM experiments might provide a method of elucidating these unknowns. Such understanding would be able to further guide the simulations of mechanical coupling to achieve a more accurate representation of the distribution of forces that intrinsically develop during growth, and how those forces affect the growth of CNTs.

Bibliography

[1] M. S. Dresselhaus, G. Dresselhaus, and R. Saito, "Physics of carbon nanotubes," *Carbon N. Y.*, vol. 33, no. 7, pp. 883–891, 1995.

[2] R. H. Baughman, A. a Zakhidov, and W. a de Heer, "Carbon nanotubes--the route toward applications.," *Science*, vol. 297, no. 5582, pp. 787–792, 2002.

[3] M. F. L. De Volder, S. H. Tawfick, R. H. Baughman, and a J. Hart, "Carbon nanotubes: present and future commercial applications.," *Science*, vol. 339, no. 6119, pp. 535–9, 2013.

[4] S. Iijima, "Helical microtubules of graphitic carbon," *Nature*, vol. 354, no. 6348, pp. 56–58, 1991.

[5] P. E., M. D., W. Q., G. K., and D. H, "Thermal Conductance of an Individual Single-Wall Carbon Nanotube above Room Temperature," *Nano Lett.*, vol. 6, p. 96, 2006.

[6] J. H. Lienhard IV and J. H. Lienhard V, *A Heat Transfer Textbook*, 3rd ed. Cambridge, MA: Phlogiston Press, 2008.

[7] B. Q. Wei, R. Vajtai, and P. M. Ajayan, "Reliability and current carrying capacity of carbon nanotubes," *Appl. Phys. Lett.*, vol. 79, no. 8, pp. 1172–1174, 2001.

[8] C. Subramaniam, T. Yamada, K. Kobashi, A. Sekiguchi, D. N. Futaba, M. Yumura, and K. Hata, "One hundred fold increase in current carrying capacity in a carbon nanotube-copper composite.," *Nat. Commun.*, vol. 4, p. 2202, 2013.

[9] B. Peng, M. Locascio, P. Zapol, S. Li, S. L. Mielke, G. C. Schatz, and H. D. Espinosa, "Measurements of near-ultimate strength for multiwalled carbon nanotubes and irradiation-induced crosslinking improvements.," *Nat. Nanotechnol.*, vol. 3, no. 10, pp. 626–631, 2008.

[10] R. D. Conner, R. B. Dandliker, and W. L. Johnson, "Mechanical Properties of Tungsten and Steel Fiber Reinforced Zr41.25Ti13.75Cu12.5Ni10Be22.5 Metallic Glass Matrix Composites," *Acta Mater.*, vol. 46, no. 17, pp. 6089–6102, 1998.

[11] J. K. Holt, H. G. Park, Y. Wang, M. Stadermann, A. B. Artyukhin, C. P. Grigoropoulos, A. Noy, and O. Bakajin, "Sub – 2-Nanometer Carbon Nanotubes," vol. 312, no. May, pp. 1034–1038, 2006.

[12] F. Fornasiero, H. G. Park, J. K. Holt, M. Stadermann, C. P. Grigoropoulos, A. Noy, and O. Bakajin, "Ion exclusion by sub-2-nm carbon nanotube pores.," *Proc. Natl. Acad. Sci. U. S. A.*, vol. 105, no. 45, pp. 17250–17255, 2008.

[13] S. Tawfick, K. O'Brien, and a. J. Hart, "Flexible high-conductivity carbon-nanotube interconnects made by rolling and printing," *Small*, vol. 5, no. 21, pp. 2467–2473, 2009.

[14] E. J. Garcia, B. L. Wardle, and a. John Hart, "Joining prepreg composite interfaces with aligned carbon nanotubes," *Compos. Part A Appl. Sci. Manuf.*, vol. 39, no. 6, pp. 1065–1070, 2008.

[15] L. Ge, S. Sethi, L. Ci, P. M. Ajayan, and A. Dhinojwala, "Carbon nanotube-based synthetic gecko tapes.," *Proc. Natl. Acad. Sci. U. S. A.*, vol. 104, no. 26, pp. 10792–10795, 2007.

[16] T. T. T. Tong, Y. Z. Y. Zhao, L. Delzeit, a. Kashani, M. Meyyappan, and a. Majumdar, "Dense Vertically Aligned Multiwalled Carbon Nanotube Arrays as Thermal Interface Materials," *IEEE Trans. Components Packag. Technol.*, vol. 30, no. 1, pp. 92–100, 2007.

[17] M. Terrones, "Science and Technology of the Twenty-First Century: Synthesis, Properties, and Applications of Carbon Nanotubes," *Annu. Rev. Mater. Res.*, vol. 33, no. 1, pp. 419–501, 2003.

[18] M. Endo, T. Hayashi, and Y.-A. Kim, "Large-scale production of carbon nanotubes and their applications," *Pure Appl. Chem.*, vol. 78, no. 9, pp. 1703–1713, 2006.

[19] V. Jourdain and C. Bichara, "Current understanding of the growth of carbon nanotubes in catalytic chemical vapour deposition," *Carbon N. Y.*, vol. 58, pp. 2–39, Jul. 2013.

[20] M. Kumar, "Carbon nanotube synthesis and growth mechanism," *Nanotechnol. Nanomater.*, no. Cvd, 2011.

[21] H. Zhu, K. Suenaga, A. Hashimoto, K. Urita, K. Hata, and S. Iijima, "Atomic-resolution imaging of the nucleation points of single-walled carbon nanotubes," *Small*, vol. 1, no. 12, pp. 1180–1183, 2005.

[22] S. Helvig, C. Lopez-Cartes, J. Sehested, P. L. Hansen, B. S. Clausen, J. R. Rostrup-Nielsen, F. Abiid-Pedersen, and J. K. Norskov, "Atomic-scale imaging of carbon nanofibre growth," *Nature*, vol. 427, no. January, pp. 5–8, 2004.

[23] S. Zhang, S. L. Mielke, R. Khare, D. Troya, R. S. Ruoff, G. C. Schatz, and T. Belytschko, "Mechanics of defects in carbon nanotubes: Atomistic and multiscale simulations," *Phys. Rev. B - Condens. Matter Mater. Phys.*, vol. 71, no. 11, pp. 1–12, 2005.

[24] J. N. Coleman, U. Khan, W. J. Blau, and Y. K. Gun'ko, "Small but strong: A review of the mechanical properties of carbon nanotube-polymer composites," *Carbon N. Y.*, vol. 44, no. 9, pp. 1624–1652, 2006.

[25] P. N. Nirmalraj, P. E. Lyons, S. De, J. N. Coleman, and J. J. Boland, "Electrical connectivity in single-walled carbon nanotube networks.," *Nano Lett.*, vol. 9, no. 11, p. 3890, 2009.

[26] R. S. Prasher, X. J. Hu, Y. Chalopin, N. Mingo, K. Lofgreen, S. Volz, F. Cleri, and P. Keblinski, "Turning carbon nanotubes from exceptional heat conductors into insulators," *Phys. Rev. Lett.*, vol. 102, no. 10, pp. 1–4, 2009.

[27] M. Bedewy, E. Meshot, M. Reinker, and A. Hart, "Population growth dynamics of carbon nanotubes," *ACS Nano*, vol. 5, no. 11, pp. 8974–89, 2011.

[28] M. Bedewy and a J. Hart, "Mechanical coupling limits the density and quality of self-organized carbon nanotube growth.," *Nanoscale*, vol. 5, no. 7, pp. 2928–37, Apr. 2013.

[29] M. K. Beyer and H. Clausen-Schaumann, "Mechanochemistry: the mechanical activation of covalent bonds.," *Chem. Rev.*, vol. 105, no. 8, pp. 2921–48, Aug. 2005.

[30] V. V Boldyrev, "Mechanochemistry of Solids : Past , Present , and Prospects," vol. 8, 2000.

[31] L. Takacs, "Quicksilver from cinnabar: The first documented mechanochemical reaction?," *Jom*, vol. 52, no. 1, pp. 12–13, 2000.

[32] J. M. D. Ribas-Arino, "Covalent Mechanochemistry: Theoretical Concepts and\nComputational Tools with Applications to Molecular Nanomechanics," *Chem. Rev.*, pp. 5412–5487, 2012.

[33] P. Baláž, M. Achimovičová, M. Baláž, P. Billik, Z. Cherkezova-Zheleva, J. M. Criado, F. Delogu, E. Dutková, E. Gaffet, F. J. Gotor, R. Kumar, I. Mitov, T. Rojac, M. Senna, A. Streletskii, and K. Wieczorek-Ciurowa, "Hallmarks of mechanochemistry: from nanoparticles to technology.," *Chem. Soc. Rev.*, vol. 42, no. 18, pp. 7571–637, Sep. 2013.

[34] E. M. Gutnam, *Mechanochemistry of materials*. Cambridge Int Science Publishing, 1998.

[35] M. K. Beyer, "Coupling of Mechanical and Chemical Energy: Proton Affinity as a Function of External Force," *Angew. Chemie - Int. Ed.*, vol. 42, no. 40, pp. 4913–4915, 2003.

[36] C. Vasiliu-Oprea and F. Dan, *Macromolecular mechanochemistry*. Cambridge: Cambridge Int Science Publishing, 2006.

[37] A. L. Black, J. M. Lenhardt, and S. L. Craig, "From molecular mechanochemistry to stress-responsive materials," *J. Mater. Chem.*, vol. 21, no. 6, p. 1655, 2011.

[38] Z. V. Todres, *Organic mechanochemistry and its practical applications*. CRC Press, 2006.

[39] M. Rief, "Single Molecule Force Spectroscopy on Polysaccharides by Atomic Force Microscopy," *Science (80-.).*, vol. 275, no. 5304, pp. 1295–1297, Feb. 1997.

[40] F. R. Kersey, W. C. Yount, and S. L. Craig, "Single-molecule force spectroscopy of bimolecular reactions: system homology in the mechanical activation of ligand substitution reactions," *J Am Chem Soc*, vol. 128, no. 12, pp. 3886–3887, 2006.

[41] J. N. Brantley, K. M. Wiggins, and C. W. Bielawski, "Polymer mechanochemistry: the design and study of mechanophores," *Polym. Int.*, vol. 62, no. 1, pp. 2–12, Jan. 2013.

[42] S. Karthikeyan, S. L. Potisek, A. Piermattei, and R. P. Sijbesma, "Highly efficient mechanochemical scission of silver-carbene coordination polymers," *J. Am. Chem. Soc.*, vol. 130, no. 45, pp. 14968–14969, 2008.

[43] A. Piermattei, S. Karthikeyan, and R. P. Sijbesma, "Activating catalysts with mechanical force.," *Nat. Chem.*, vol. 1, no. 2, pp. 133–137, 2009.

[44] Q. Deng, M. Smetanin, and J. Weissmüller, "Mechanical modulation of reaction rates in electrocatalysis," *J. Catal.*, vol. 309, pp. 351–361, 2014.

[45] Y. Yang, T. Adit Maark, A. Peterson, and S. Kumar, "Elastic strain effects on catalysis of a PdCuSi metallic glass thin film," *Phys. Chem. Chem. Phys.*, vol. 17, no. 3, pp. 1746–1754, 2015.

[46] P. Strasser, S. Koh, T. Anniyev, J. Greeley, K. More, C. Yu, Z. Liu, S. Kaya, D. Nordlund, H. Ogasawara, M. F. Toney, and A. Nilsson, "Lattice-strain control of the activity in dealloyed core-shell fuel cell catalysts.," *Nat. Chem.*, vol. 2, no. 6, pp. 454–460, 2010.

[47] M. F. Francis and W. a. Curtin, "Mechanical work makes important contributions to surface chemistry at steps," *Nat. Commun.*, vol. 6, p. 6261, 2015.

[48] M. J. Aziz, E. Nygren, J. F. Hays, and D. Turnbull, "Crystal growth kinetics of boron oxide under pressure," *J. Appl. Phys.*, vol. 57, no. 6, pp. 2233–2242, 1985.

[49] G. Q. Lu, E. Nygren, M. J. Aziz, D. Turnbull, and C. W. White, "Pressure-enhanced solid phase epitaxy of germanium," *Appl. Phys. Lett.*, vol. 56, no. 2, pp. 137–139, 1990.

[50] M. J. Aziz, P. C. Sabin, and G. Q. Lu, "The activation strain tensor: Nonhydrostatic stress effects on crystal-growth kinetics," *Phys. Rev. B*, vol. 44, no. 18, pp. 9812–9816, 1991.

[51] H. Brune, K. Bromann, H. Roder, K. Kern, J. Jacobsen, P. Stoltze, K. Jacobsen, and J. Norskov, "Effect of Strain on Surface-Diffusion and Nucleation," *Phys. Rev. B*, vol. 52, no. 20, pp. 14380–14383, 1995.

[52] M. Sorescu, L. Diamandescu, and A. Tomescu, "Mechanochemical Synthesis of Novel Sensor Materials," *MRS Proceedings*, vol. 1226. pp. 3–8, 2009.

[53] J. Ding, W. F. Miao, P. G. McCormick, and R. Street, "Mechanochemical synthesis of ultrafine Fe powder," *Appl. Phys. Lett.*, vol. 67, no. 1995, p. 3804, 1995.

[54] J. Xue, D. Wan, S. Lee, and J. Wang, "Mechanochemical Synthesis of Lead Zirconate Titanate from Mixed Oxides," *J. Am. Ceram. Soc.*, vol. 92, pp. 1687–1692, 1999.

[55] P. G. McCormick, T. Tsuzuki, J. S. Robinson, and J. Ding, "Nanopowders synthesized by mechanochemical processing," *Adv. Mater.*, vol. 13, no. 12–13, pp. 1008–1010, 2001.

[56] Y. Tang, Y. Zhang, J. Deng, J. Wei, H. Le Tam, B. K. Chandran, Z. Dong, Z. Chen, and X. Chen, "Mechanical force-driven growth of elongated bending TiO2 -based nanotubular materials for ultrafast rechargeable lithium ion batteries.," *Adv. Mater.*, vol. 26, no. 35, pp. 6111–8, Sep. 2014.

[57] A. J. Hart and A. H. Slocum, "Force output, control of film structure, and microscale shape transfer by carbon nanotube growth under mechanical pressure.," *Nano Lett.*, vol. 6, no. 6, pp. 1254–60, Jun. 2006.

[58] K. Hasegawa and S. Noda, "Diameter increase in millimeter-tall vertically aligned single-walled carbon nanotubes during growth," *Appl. Phys. Express*, vol. 3, no. 4, pp. 3–6, 2010.

[59] D. B. Geohegan, A. a. Puretzky, J. J. Jackson, C. M. Rouleau, G. Eres, and K. L. More, "Flux-dependent growth kinetics and diameter selectivity in single-wall carbon nanotube arrays," *ACS Nano*, vol. 5, no. 10, pp. 8311–8321, 2011.

[60] E. R. Meshot, L. Plata, S. Tawfick, Y. Zhang, E. a Verploegen, and a J. Hart, "Nanotube Growth by Decoupled Catalyst," vol. 3, no. 9, pp. 2477–2486, 2009.

[61] A. A. Puretzky, D. B. Geohegan, S. Jesse, I. N. Ivanov, and G. Eres, "In situ measurements and modeling of carbon nanotube array growth kinetics during chemical vapor deposition," *Appl. Phys. A*, vol. 81, no. 2, pp. 223–240, 2005.

[62] H. J. Qi, K. B. K. Teo, K. K. S. Lau, M. C. Boyce, W. I. Milne, J. Robertson, and K. K. Gleason, "Determination of mechanical properties of carbon nanotubes and vertically aligned carbon nanotube forests using nanoindentation," *J. Mech. Phys. Solids*, vol. 51, no. 11–12, pp. 2213–2237, 2003.

[63] S. D. Mesarovic, C. M. McCarter, D. F. Bahr, H. Radhakrishnan, R. F. Richards, C. D. Richards, D. McClain, and J. Jiao, "Mechanical behavior of a carbon nanotube turf," *Scr. Mater.*, vol. 56, no. 2, pp. 157–160, 2007.

[64] S. Pathak, Z. G. Cambaz, S. R. Kalidindi, J. G. Swadener, and Y. Gogotsi, "Viscoelasticity and high buckling stress of dense carbon nanotube brushes," *Carbon N. Y.*, vol. 47, no. 8, pp. 1969–1976, 2009.

[65] a. Qiu, D. F. Bahr, a. a. Zbib, a. Bellou, S. D. Mesarovic, D. McClain, W. Hudson, J. Jiao, D. Kiener, and M. J. Cordill, "Local and non-local behavior and coordinated buckling of CNT turfs," *Carbon N. Y.*, vol. 49, no. 4, pp. 1430–1438, 2011.

[66] S. Pathak, N. Mohan, P. P. S. S. Abadi, S. Graham, B. a. Cola, and J. R. Greer, "Compressive response of vertically aligned carbon nanotube films gleaned from in situ flat-punch indentations," *J. Mater. Res.*, vol. 28, no. 7, pp. 984–997, 2012.

[67] S. Korte, R. J. Stearn, J. M. Wheeler, and W. J. Clegg, "High temperature microcompression and nanoindentation in vacuum," *J. Mater. Res.*, vol. 27, no. 01, pp. 167–176, 2012.

[68] J. C. Trenkle, C. E. Packard, and C. a Schuh, "Hot nanoindentation in inert environments.," *Rev. Sci. Instrum.*, vol. 81, no. 7, p. 073901, Jul. 2010.

[69] P. M. Holland, B. E. Eaton, and H. J. M. Hanley, "A correlation of the viscosity and thermal conductivity data of gaseous and liquid ethylene," *J. Phys. Chem. Ref. Data*, vol. 12, no. 4, pp. 917–932, 1983.

[70] A. J. Hart, "Chemical, Mechanical, and Thermal Control of Substrate-Bound Carbon Nanotube Growth," *Carbon Nanotub.*, no. December, pp. 1–14, 2006.

[71] F. L. Deepak, A. Govindaraj, and C. N. R. Rao, "Improved synthesis of carbon nanotubes with junctions and of single-walled carbon nanotubes," *J. Chem. Sci.*, vol. 118, no. 1, pp. 9–14, 2006.

[72] C. R. Oliver, E. S. Polsen, E. R. Meshot, S. Tawfick, S. J. Park, M. Bedewy, and a. J. Hart, "Statistical analysis of variation in laboratory growth of carbon nanotube forests and recommendations for improved consistency," *ACS Nano*, vol. 7, no. 4, pp. 3565–3580, 2013.

[73] K. Hata, D. N. Futaba, K. Mizuno, T. Namai, M. Yumura, and S. Iijima, "Water-assisted highly efficient synthesis of impurity-free single-walled carbon nanotubes.," *Science*, vol. 306, no. 5700, pp. 1362–1364, 2004.

[74] E. R. Meshot and a. J. Hart, "Abrupt self-termination of vertically aligned carbon nanotube growth," *Appl. Phys. Lett.*, vol. 92, no. 11, pp. 90–93, 2008.

[75] a a Zbib, S. D. Mesarovic, E. T. Lilleodden, D. McClain, J. Jiao, and D. F. Bahr, "The coordinated buckling of carbon nanotube turfs under uniform compression.," *Nanotechnology*, vol. 19, no. 17, p. 175704, 2008.

[76] M. Bedewy, E. R. Meshot, H. Guo, E. a. Verploegen, W. Lu, and a. J. Hart, "Collective mechanism for the evolution and self-termination of vertically aligned carbon nanotube growth," *J. Phys. Chem. C*, vol. 113, no. 48, pp. 20576–20582, 2009.

[77] M. Bedewy, E. R. Meshot, M. J. Reinker, and a J. Hart, "Population growth dynamics of carbon nanotubes.," *ACS Nano*, vol. 5, no. 11, pp. 8974–89, Nov. 2011.

[78] T. Hertel, R. E. Walkup, and P. Avouris, "Deformation of carbon nanotubes by surface van der Waals forces," *Phys. Rev. B*, vol. 58, no. 20, pp. 13870–13873, 1998.

[79] R. S. R. Ruoff, J. Tersoff, D. C. Lorents, S. Subramoney, and B. Chan, "Radial deformation of carbon nanotubes by van der Waals forces," *Nature*, vol. 364, no. 6437, pp. 514–516, 1993.

[80] J. J. Vilatela, J. a. Elliott, and A. H. Windle, "A model for the strength of yarn-like carbon nanotube fibers," *ACS Nano*, vol. 5, no. 3, pp. 1921–1927, 2011.

[81] A. Rao, S. Tawfick, M. Bedewy, and A. J. Hart, "Morphology-driven mechanics and strength limits of carbon nanotube yarns."

[82] L. D. Landau and E. M. Lifshitz, *Theory of elasticity*, 3rd ed. Oxford, England: Pergamon Press, 1986.

[83] J. N. Israelachvili, *Chapter 13 - Van der Waals Forces between Particles and Surfaces*. 2011.

[84] Y. Mo, K. T. Turner, and I. Szlufarska, "Friction laws at the nanoscale.," *Nature*, vol. 457, no. 7233, pp. 1116–1119, 2009.

[85] H. C. Chiu, B. Ritz, S. Kim, E. Tosatti, C. Klinke, and E. Riedo, "Sliding on a nanotube: Interplay of friction, deformations and structure," *Adv. Mater.*, vol. 24, no. 21, pp. 2879–2884, 2012.

[86] D. Qian, G. J. Wagner, W. K. Liu, M.-F. Yu, and R. S. Ruoff, "Mechanics of carbon nanotubes," *Appl. Mech. Rev.*, vol. 55, no. 6, p. 495, 2002.

[87] M. Yu, "Strength and Breaking Mechanism of Multiwalled Carbon Nanotubes Under Tensile Load," *Science (80-.).*, vol. 287, no. 5453, pp. 637–640, 2000.

[88] M. F. Yu, T. Kowalewski, and R. S. Ruoff, "Investigation of the radial deformability of individual carbon nanotubes under controlled indentation force," *Phys. Rev. Lett.*, vol. 85, no. 7, pp. 1456–1459, 2000.

[89] a. Buldum and J. P. Lu, "Atomic Scale Sliding and Rolling of Carbon Nanotubes," p. 4, 1999.

[90] J. Lou, F. Ding, H. Lu, J. Goldman, Y. Sun, and B. I. Yakobson, "Mesoscale reverse stick-slip nanofriction behavior of vertically aligned multiwalled carbon nanotube superlattices," *Appl. Phys. Lett.*, vol. 92, no. 20, pp. 15–17, 2008.